Exploiting the Enhanced Permeability and Retention Effect for the Targeting of Tumors with ^{18}F-SiFA Polymer Nanoparticles

by

Sheldon Stephen Berke

A thesis submitted in partial fulfillment of the requirements for the degree of

Master of Science

in

Cancer Sciences

Department of Oncology
University of Alberta

Abstract

Over the last several decades great progress has been made in cancer diagnosis and detection. One foundation of this progress has been improved imaging technologies. Among the most promising imaging technologies for cancer detection is Positron Emission Tomography (PET). PET imaging allows for visualization of cancerous tissue through the utilization of positron emitting radioactive nuclides attached to biomolecules, which are designed to target the unique characteristics of cancerous cells. Current radiotracers, mostly small molecules, monoclonal antibodies, and peptides have shown varying degrees of clinical success. In most cases serious limitations exist which prevent their use in more than a fraction of cancers[1]. Recently, a unique cancer characteristic has shown vulnerability to targeting, a trait existing in almost all solid tumors. Solid tumors have a unique vascular architecture in comparison with normal tissue. Vascular defects and poor lymphatic drainage result in solid tumors possessing a unique physiological environment. These abnormal conditions facilitate the accumulation of nanometer-sized particles. Exploiting this phenomenon, known as the enhanced permeability and retention (EPR) effect, with functionalized nanoparticles may lead to new diagnostics and therapies of cancer. To further understand the EPR effect, a range of polymer nanoparticles (PNPs) of distinct sizes, from 10 nm to 130 nm , were synthesized and functionalized with the Silicon-Fluoride Acceptor (SiFA) isotopic exchange technology (PNP1-PNP3, PNP5-PNP14). This SiFA group allows for simple and rapid fluorine-18 labeling under mild conditions. PNPs were chosen due to their ease of functionalization, low inherent toxicity, and extensive tunability. Optimal radiolabeling methodologies were established, including green chemistry conditions, resulting in fluorine-18 incorporation from 59 - 79% and radiochemical yields ranging from 28 – 43%. Purification of PNPs was achieved through

size exclusion chromatography. Four ^{18}F-labeled PNPs (sizes: 20 nm, 33 nm, 45 nm, and 72 nm) were then chosen for injection into EMT-6 tumor bearing mice and their biodistribution was observed over a time course of 4-hours p.i. PET scan. Biodistribution studies determined that both organ and tumor uptake were dependent on PNP size. Furthermore, tumor accumulation for several ^{18}F-PNPs (33 nm, 45 nm, and 72 nm) increased from 1- to 4-hours p.i.. This work revealed that the 33 nm nanoparticle, ^{18}F-PNP5, was the most effective ^{18}F-PNP for tumor targeting, displaying a tumor SUV_{mean} of 0.97 and a tumor to muscle ratio of 4.22 at 4-hours p.i.. These results compare favorably with other classes of tumor targeting PET agents and reveal that SiFA-radiolabeled PNPs, specifically in the 30 nm range, should be further evaluated as tumor-targeting agents in this specific tumor model.

Acknowledgments

Many individuals and research groups were essential to the completion of the following thesis. Below is a short list of those who have made this possible:

To those mentioned above, and all the others who helped in my education and research, thank you.

Table of Contents

List of Tables

List of Figures

List of Abbreviations

NP	nanoparticle
CT	computed tomography
MRI	magnetic resonance imaging
SPECT	single photon emission tomography
PET	positron emission tomography
^{99m}Tc	technetium-99m
MDP	methylene diphosphonate
keV	kiloelectron volts
mm	millimeter
nm	nanometer
MeCN	acetonitrile
p	proton
n	neutron
α	alpha particle
FDG	fluorodeoxyglucose
ATP	adenosine triphosphate
met	methionine
FET	O-(2-fluoroethyl)-L-tyrosine
SUV_{mean}	mean standard uptake value
DNA	deoxyribonucleic acid
dUMP	deoxyuridine monophosphate
TMP	thymidine monophosphate
TDP	thymidine diphosphate
TTP	thymidine triphosphate
TK1	thymidine kinase 1
FLT	3'-Fluoro-3'-deoxythymidine
PC	phosphatidylcholine
CK	choline kinase
FMISO	Fluoromisonidazole
FAZA	1-(5-fluoro-5-deoxy-α-D-arabinofuranosyl)-2-nitroimidazole

EF5	2-(2-nitro-(1)H-imidazol-1-yl)-N-(2,2,3,3,3-pentafluoropropyl)-acetamide
ATSM	diacetyl-bis(N4-methylthiosemicarbazone)
PTK	protein tyrosine kinase
RTK	receptor tyrosine kinase
mAB	monoclonal antibodies
VEGF	vascular endothelial growth factor
VEGFR	vascular endothelial growth factor receptor
DLL4	delta like canonical notch ligand 4
FGF	fibroblast growth factor
PDGFB	platelet derived growth factor B
EGF	endothelial growth factor
LPA	Lysophosphatidic acid
EPR	enhanced permeability and retention
^{64}CuAuNPs	copper-64 labeled gold nanoparticles
SMANCS	styrene-maleic acid conjugated neocarzinostatin
kDA	kilodalton
PEG	polyethylene glycol
RES	reticuloendothelial system
cRGD	cyclic Arg-Gly-Asp
%ID/g	percent injected dose per gram
SCC	sickle cell carcinoma
AC	adenocarcinoma
STS	soft tissue carcinoma
LS	liposarcoma
TCC	transitional cell carcinoma
DOTA	1,4,7,10-tetraazacyclododecane-1,4,7,10-tetraacetic acid
TETA	Triethylenetetramine
PNP	polymer nanoparticle
NREP	nanoreporter
SOD	superoxide dismutase
C-dots	cornell dots

SFB   N-succinimidyl 4-[^{18}F]fluorobenzoate

FBBA   4-[^{18}F]fluorobenzy-2-bromoacetamide

NOTA   1,4,7-triazacyclononane-1,4,7-trisacetic acid

QMA   quaternary methylammonium

μmol   micromole

TLC   thin layer chromatography

Bq   becquerel

RCY   radio-chemical yield

MBq   mega becquerel

SiFA IE   silicon fluoride acceptor isotopic exchange

HPLC   high pressure liquid chromatography

AIBN   azo-bis-(isobutyronitrile)

HDDA   (1,6-hexandiol diacrylate)

Khz   kilohertz

SEC   size exclusion chromatography

PPM   parts per million

MeCN   acetonitrile

EtOH   ethanol

MeOH   methanol

TLC   thin layer chromatography

RF   retention factor

TEM   transmission electron microscopy

PBS   phosphate buffered saline

mL   milliliters

min   minute

T/M   tumor to muscle ratio

p.i.   p.i.

SUV   standardized uptake value

TAC   time activity curve

1. Introduction

Cancer diagnosis has reached a stage where earlier detection is necessary to help increase the survival rate of patients. Improvements in early detection have been garnered through extensive technological developments and expansive scientific research. Imaging technology has improved vastly over the past century and with it a better understanding of cancer. These improvements have allowed new cancer-targeting agents to be developed, which can differentiate healthy tissue from cancer. Countless tumor targeting agents have been designed with many showing varying degrees of clinical success. Still, serious limitations exist preventing their widespread use in cancer diagnosis. Over the last two decades, nanoparticles (NPs) have emerged as a viable tumor targeting option in both therapy and diagnosis. NPs display unique physical characteristics, which allow them to inherently exploit the characteristics of almost all solid tumors. Improved understanding of NPs and their interaction with tumors is essential to the progress of cancer detection.

1.1. Medical Imaging

Improvements in technology have led to advancements in the *in vivo* visualization of biological processes and physiological structures through medical imaging. This progress has ushered the development of diagnostics and therapies of cancer, and other diseases. Over the last century, medical imaging has emerged as a valuable tool while continuing to improve in effectiveness, efficiency, and utility.[2-6] The discovery of radiation at the end of the 19th century led to a cascade of technological evolutions and innovations. These developments have provided clinics with the capability to visualize physiological structures and functions in a non-invasive manner through medical imaging. X-ray imaging, or computed tomography (CT), magnetic resonance imaging (MRI), and ultrasound are the three most common medical imaging modalities and have proven to be successful in structural imaging.[4,7-9] Alternative imaging modalities involve injecting radioactive substances into the patient's body and tracking the radiation to determine the molecules biodistribution. Unstable nuclides that emit radiation provide a means of imaging biological functions through two main nuclear imaging techniques: positron

emission tomography (PET) and single photon emission computed tomography (SPECT).[6,10]

Medical imaging began to take form after Wilhelm Conrad Roentgens discovery of the X-ray in 1895.[11] This discovery eventually led to a Nobel Prize in 1901 and a torrent of inventions and innovations, providing clinics with an array of medical imaging techniques. Roentgen realized that X-rays (high-energy photons) would penetrate different mediums with different attenuation. This unique property allows for the imaging of tissues of contrasting densities. Bones are clearly visible in X-ray images due to their high density, which assists in the detection of fractures and malformations. Furthermore, X-ray technology is capable of detecting soft tissue tumors once sufficiently dense. This function allows X-ray imaging to be used for the diagnosis of several cancers, predominantly bone, lung, and breast.[4,12] As technology advanced, X-ray imaging would be used in conjunction with computational software to enhance its capabilities. X-ray technicians could then easily control X-ray energy, observe better contrast, incorporate complex algorithms to increase resolution, and introduce CT to visualize bones three-dimensionally.[8] X-ray and CT are excellent at imaging dense tissues such as bones and advanced solid tumors; unfortunately, this technique is not as capable in soft tissue imaging. Although, there are several other imaging techniques that are proficient in imaging the structural characteristics of soft tissue. Ultrasound and MRI have proven to be highly effective in this regard.

Ultrasound exploits the backscattering propensity of sound waves to map shallow depths of tissue. This process is possible due to the unique characteristics of the piezo crystal. This material has the ability to convert sonic pulses to an electrical signal and vice versa.[9] Ultrasound Imaging has many benefits including real-time imaging, high spatial and temporal resolution, and the use of safe, non-ionizing radiation. These features, combined with the mobile nature of ultrasound devices, provide a widely accessible and safe imaging technology. Unfortunately, there are several drawbacks to ultrasound technology such as its limited depth penetration, limited tissue imaging range, and operator dependency.[9,13] MRI is possible due to the spin possessed by certain nuclei.[14] Hydrogen-1 is the most abundant nucleus within the body that displays spin. Hydrogen is significant

due to its presence in water, a substantial component of soft tissue.[15,16] This imaging technique displays high resolution and soft-tissue contrast, unfortunately, the long imaging times and high cost create accessibility issues for many patients.

Anatomical imaging is useful for detecting physical ailments and primary tumors if the tumor has grown large enough to display physical abnormalities. Unfortunately, at this stage the disease has already progressed to a pernicious state.[12,17] In order to diagnose cancer, before significant progression of the disease, detection must be possible at a molecular level. Nuclear imaging has proven to be a potential solution in this requisite.[10,13,18] Nuclear imaging utilizes the ionizing radiation emitted from unstable isotopes as they decay to a more stable state. Compounds containing radioactive isotopes are injected into the patient and scintillator crystals are used to detect the ionizing radiation.[19,20] Functionalizing a cancer-targeting molecule with radioactive nuclides provides insight on the molecules' biodistribution. Tracking the biodistribution of these cancer-targeting molecules can be used to determine the location of cancerous cells in the body, elucidating not only primary tumors but also peripheral tumors that have not yet induced structural changes (Figure 1).

Figure 1: PET/CT scan of a 53-year-old female patient with triple negative breast cancer. [^{18}F]FDG used as imaging agent. Arrows point to tumors. Image taken from Imaging of triple-negative breast cancer.[21] Permission granted through Rightslink®

The ability to control and utilize the unique physical properties of radioactive isotopes has led to advances in disease diagnosis, a better understanding of cancer, and improved therapies.[6,19,22-26] SPECT imaging utilizes the gamma rays emitted from unstable nuclides (a single gamma ray for every nucleus) as they relax to a more stable state (via internal conversion).[27] These photons pass through lead collimators and excite crystal scintillators that then relay the signal, which is processed by complex computational

software. Functional imaging can be done at virtually unlimited depth penetration when visualizing biological processes. Unfortunately, SPECT has limited spatial resolution and low sensitivity due to the necessity of lead collimators, which filter out the majority of gamma photons.[27,28]

PET, the alternative nuclear imaging technology, has established itself as a more sophisticated imaging technique over SPECT, as PET generally has much better spatial resolution (~2 mm) and substantially superior sensitivity (~10^{-12}Mol•L^{-1}).[29] Furthermore, carbon-11, a common PET radionuclide, is an isotope of an element naturally found in most bioactive molecules.[13,18,12] The incorporation of a radioactive nuclide without changing the chemical structure of the native biological molecule allows for a true assessment of the molecule at microdose *in vivo* (as opposed to radioactive analogues). PET tracers can be utilized as a tool in initial cancer diagnosis, detecting peripheral tumors, or assessing the effectiveness of cancer therapies.[6,12,13,22,24-26] PET utilizes radioactive nuclides with a proton rich nucleus. Radioactive isotopes that have an abundance of protons, such as fluorine-18, carbon-11, or copper-64, emit a single positron during the decay to a more stable state. The positron travels a short distance (2-10 mm) until it loses sufficient kinetic energy and encounters its antiparticle, an electron, where both are immediately annihilated. This annihilation event creates two gamma photons with 511 keV of energy. The photons then travel opposite direction from one another and scintillator crystals are used to detect the photons in coincidence. The scintillator crystal is coupled to photomultipliers that transmit the signal to a computer. This relay system enables the construction of a line of response, which provides valuable information about the location of the radioactive nuclides in 3D space (Figure 2).[20]
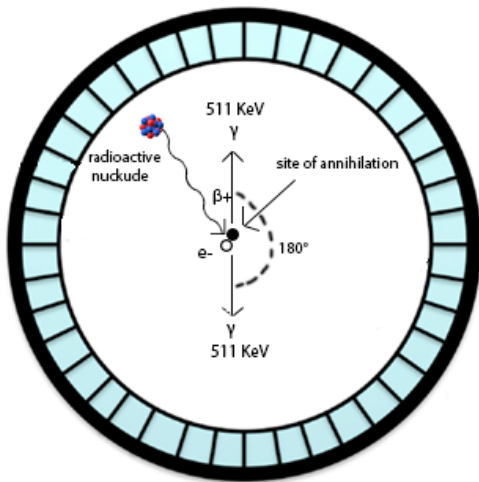
Figure 2: Positron Emission Tomography diagram. As the radioactive nuclide decays, a proton is converted to a neutron, complimented by the emission of a positron. The positron travels a short distance, determined by its kinetic energy. As the positron travels, it undergoes collisions with electrons and loses kinetic energy. After sufficient kinetic energy is lost, the positron collides with an electron and both particles are instantaneously annihilated. The annihilation results in the production of two gamma photos of 511 keV, which travel in opposite directions. Information for image taken from The Handbook of Radiopharmaceuticals.[20]

There are four coincidence events that occur in PET (Figure 3):[30] True coincidences, where the line of response that is established is a true indicator of where the annihilation event occurred; Scatter coincidences, where one of the pair of gamma rays undergoes Compton scattering (scattering of the photon caused by charged particles); Random coincidences, where detection occurs from gamma photons produced by two distinct nuclei; and Gamma coincidence occurring when a 511 keV photon and a gamma photon from another nuclear event are detected simultaneously. The three latter events are not a true indication of the annihilation event location and can introduce error into the PET results. These coincidence errors, along with deficiencies in the signal detection and relay technology, can reduce the quality of PET images. Fortunately, there are several methods to improve PET scan quality: improved scintillator crystals, superior photon transduction, and computational improvements can all enhance PET image quality.
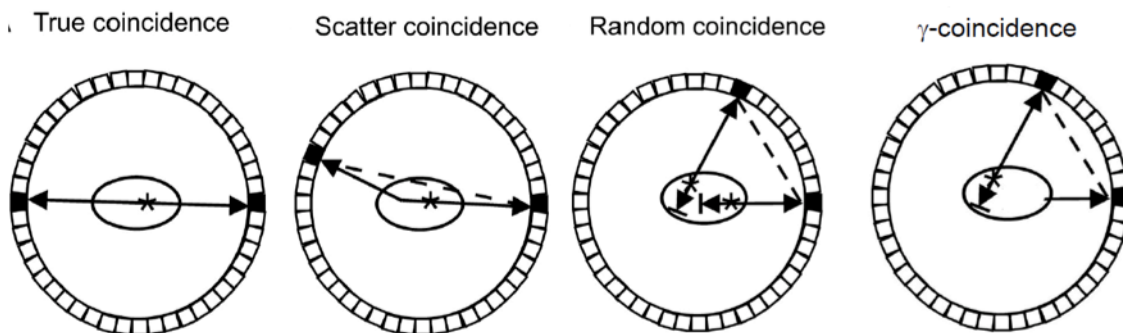
Figure 3: Coincidence events in PET imaging. True coincidence: the line of response (line drawn between two coincidence events) that is established is a true indicator of where the annihilation event occurred. Scatter Coincidence: one of the pair of 511 keV gamma rays undergoes Compton scattering. Random coincidence: detection occurs as a result of gamma photons from two distinct nuclei. Gamma coincidence: occurs when a 511 keV photon and a gamma photon from another nuclear event are detected simultaneously.

Two primary materials encompass the gamma photon detection system in PET: Scintillator crystals and photomultipliers.[20] Scintillator crystals are excited by a gamma photon and subsequently relax, emitting light that is detected by photomultiplier tubes. The efficiency of this system is dependent on crystal density, crystal excitation range, crystal relaxation time, and the relay capabilities of photomultiplier tubes. Initially, PET scintillator crystals were constructed out of bismuth germinate and although these rudimentary crystals had a high density they also had low light production and long decay time.[20] New scintillator crystals (Lutetium oxyorthosilicate or lutetium–yttrium oxyorthosilicate for example) exhibit a shorter relaxation time, narrower excitation ranges, and output more intense light pulses.[31] Additionally, advancements in manufacturing technology have allowed for smaller crystals to be produced that create better spatial resolution.[32] New photomultipliers have improved image quality by increasing efficiency of the signal transduction pathway. Lastly, analysis software has been designed to reduce background noise. Advanced algorithms have been developed to neglect the majority of coincidence events that do not represent true coincidence events.[33-35]

Positron emitting nuclides can be prepared in cyclotrons under well established and reliable conditions.[19] Moreover, these PET compatible radionuclides have a plethora of simple and effective radiolabeling methodologies.[19,36-41] The high clinical translation of PET allows for streamlined development of radiotracers along with the pharmacokinetic assessment of new drug candidates during the early stages of clinical development. A wide range of successful cancer tracers has already been developed with many more surely to come.

1.2. Radionuclides

Radioactive nuclides used in PET have an unstable nucleus with a proton to neutron ratio that is too high and therefore lies above the line of beta stability (Figure 4).[42] For the nuclide to reach a stable state it must reduce the number of protons. Positron emission involves the conversion of a proton to a neutron, supplemented by the emission of a positron and an electron neutrino. The positron then travels with a defined maximum

energy (positron emission energy).[27] Each radionuclide has its own unique nuclear properties (Table 1), which must be taken into consideration when designing a radioactive tracer. Additionally, both radionuclide production method and availability of the parent isotope of the radioactive nuclide must be accounted for.
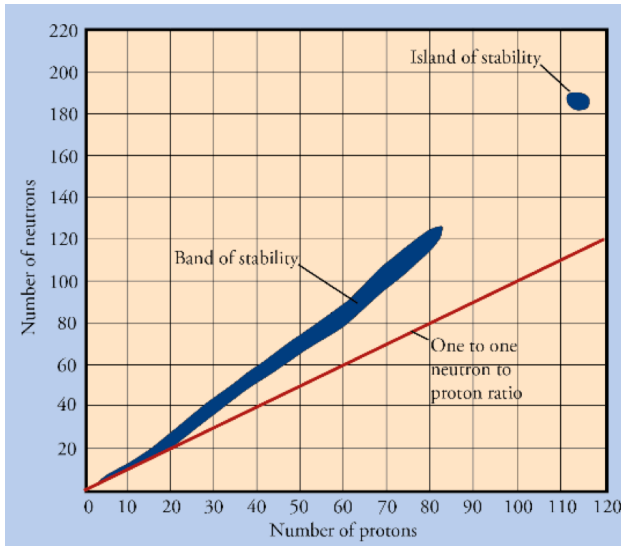
Figure 4: Line of stability for nuclides. The blue line represents nuclides that are stable. The red line represents a one to one neutron to proton ratio. As the number of protons increases more neutrons are needed at a higher ratio to stabilize the nucleus.

Decay composition, half-life, and positron emission energy are all nuclear properties that vary between radionuclides. A favorable radioactive PET nuclide decays primarily through positron emission. Neutron deficient nuclides can decay through positron emission, electron capture, or both.[42] Electron capture involves the conversion of a proton to a neutron, initiated when a proton captures an electron from the electron shell (predominantly the K and L shell). This process results in the emission of a gamma photon directly from the nucleus and can also lead to internal conversion (the ejection of a high energy electrons and subsequent X-rays). These gamma rays will interfere with the PET detectors and increase the background noise in a PET scan. Additionally, a radionuclide that does not decay solely through positron emission will require a higher concentration of activity to account for the reduction in positron emission.[20] Further disparaging, non-positron emissions subject patients to unnecessary radiation exposure. For these reasons, nuclides, which decay entirely (or near entirely) through positron emission, such as carbon-11 or fluorine-18, are preferable in PET imaging (Table 1). A second radioactive property to consider is that different radioactive nuclides can have a direct effect on the resolution of a PET scan. The positron emitted by a radioactive nuclide travels a short distance before colliding with an electron to undergo an annihilation event. The distance traveled by the positron is determined by its positron energy, a constant for each specific radioactive nuclide (Table 1). An ideal PET nuclide

7

will emit a positron with a low energy value in order to limit the distance traveled. The shorter the path length, the more accurate the cameras can associate the annihilation event with the origin of the positron (~1 mm).[27] Therefore, a low positron emission energy value ultimately leads to an image with better resolution.

Table 1: Decay properties of common radionuclides

Radionuclide	Decay composition	β+ energy (keV)	Half-life
Carbon-11	β+: 100%	960	10.4 minutes
Oxygen-15	β+: 100%	1700	2.03 minutes
Fluorine-18	β+: 97%, EC 3%	690	1.83 hours
Copper-64	EC: 45%, B-:37%, B+:18%	653	12.7 hours
Zirconium-89	β+:23%, EC:77%	900	3.3 days

β+: positron, EC: electron capture. Data taken from Handbook of Radiopharmaceuticals: Radiochemistry and Applications.[27]

Lastly in terms of nuclear characteristics, a radiochemist must consider the radioactive decay half-life for the radionuclide of choice. The time frame for radioactive nuclides can range from less than a millisecond to thousands of years. Half-lives of common PET nuclides typically range from minutes to days. The half-life of the radionuclide of interest should be appropriate for the radiosynthesis time as well as the nature of the study. Oxygen-15, with a half-life of 122 seconds, is used in blood flow imaging where a short half-life is beneficial. In contrast, zirconium-89, has a half-life of 3.3 days, making it more practical for antibody studies where a long half-life is necessary due to the slow physiological kinetics.[27,43,44]

The principal method for producing positron emitting nuclides is through charged particle accelerators. Typically these machines accelerate particles in an outward spiral motion. These cyclic particle accelerators are aptly named cyclotrons (Figure 5). Modern cyclotrons function by accelerating negatively charged particles (hydrogen-, or deuterons-) in a circular path with an oscillating electromagnetic field. Charged particles are accelerated until they have sufficient energy to penetrate the repulsive electromagnetic forces surrounding the target nucleus: the coulomb barrier. Once the particles are accelerated to this energy, the charged particles pass through a stripper foil to remove any electrons and are directed toward the target. The resulting radionuclide product depends on the accelerated particle, the energy of the particle, and the target (parent nuclide).[42] A

radiochemist must know both the columbic barrier to produce the desired radionuclide, and the availability of the target to determine whether or not production is feasible. Table 2 lists a summary of the production requirements for fluorine-18 and carbon-11.
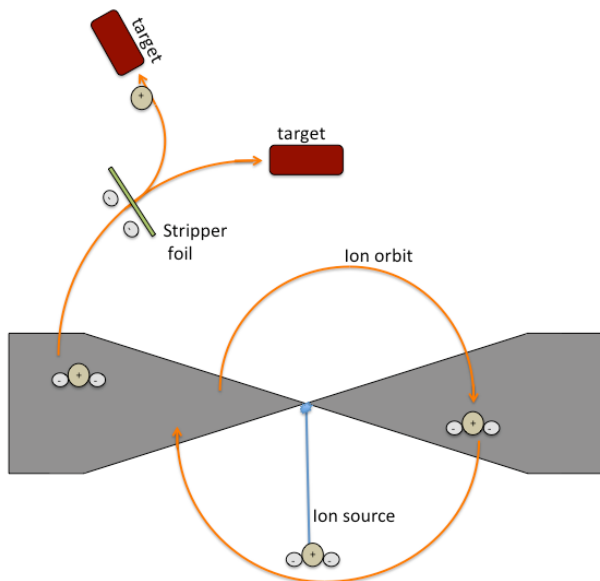
Figure 5: Diagram of a negative ion cyclotron. Negatively charged particles are introduced at the center of the cyclotron. These negative particles are accelerated outward due to an oscillating electromagnetic field produced by large magnets called Dees. At a calculated energy (columbic barrier for target) the negatively charged particle passes through a stripper foil, which removes electrons and directs the accelerated particle to the target. Data for image taken from Physical Characteristics and Production Methods. [42]

Table 2: Cyclotron production information for fluorine-18, and carbon-11

Product	Parent	Reaction	Parent nuclide natural abundance	Energy (MeV)
^{18}F	^{18}O	$^{18}O(p,n)^{18}F$	0.2%	4-14
^{11}C	^{14}N	$^{14}N(p,\alpha)^{11}C$	99.6%	7-15

Data taken from Handbook of Radiopharmaceuticals: Radiochemistry and Applications. [27]

1.3. Cancer Imaging Agents

Radioactive biochemical compounds aimed to interact specifically with certain biological functions enables *in vivo* visualization through PET imaging. In this way, it is possible to track abnormal or overactive biological functions and identify their location. Visualization of biological changes before the expression of physical symptoms provides clinicians with an advantage in treating diseases such as cancer. This distinct temporal advantage is not available through current standard cancer imaging techniques such as MRI, or X-ray. PET, however, has the potential to visualize tumors at an early stage due to its ability to target the unique features of cancer cells with radiotracers.

There are several characteristics of a radiotracer that contribute to its clinical success. Radiotracers must have high target specificity in order to show clear contrast between cancer tissue and healthy tissue.[45] Additionally, radiotracers must have good *in vivo* stability as many promising drug candidates fail due to high levels of metabolism once injected into the body. Radiotracers must also be designed to avoid excessive metabolism. Although drug metabolism is near impossible to predict, several reviews have been published on common targets for enzymes and drug metabolism.[46-48] The metabolism of radiotracers can introduce a variety of issues. Metabolized tracers are no longer intact, affecting their affinity, specificity, and effectiveness. Further complicating PET scan results, cleavage of radioactive nuclides from tracers can cause high background noise. For example, defluorination leads to high fluorine-18 bone uptake and thus high activity in bone structures (Figure 6). The lipophilicity of a radiotracer is an important quality that influences *in vivo* success as it affects blood solubility, membrane permeability, and muscle and fat uptake. Together these factors must be assessed during the design of any radiotracer.
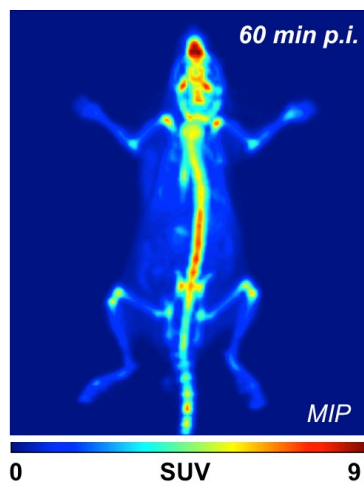
Figure 6: PET image of fluorine-18 in an EMT-6 tumor bearing mouse. Data collected over 60 minutes p.i.. High fluorine-18 uptake by bones reveals the skeletal construction of the mouse.

Cancer hallmarks (unique features indicative of cancerous cells) help oncologists characterize the diverse and extensively complex nature of tumors. In 2000 *Hanahan, et al*. described the six hallmarks as terminologies that help organize the remarkable diversity of a neoplastic disease.[49] Just over a decade later this list was expanded to 11.[50] Likely, as the biology of cancer is further explored and understood, future hallmarks will contribute to the characterization of tumors. Hanahan's 2011 paper describes the following cancer hallmarks: Evading growth suppressors, avoiding immune suppression, enabling replicative immortality, tumor promoting inflammation, activating invasion and metastasis, genome instability and mutation, resisting cell death, deregulating cellular energetics, sustaining proliferative signaling, and inducing angiogenesis. It is important to note that not all tumors express every cancer hallmark, however, these

10

hallmarks are indicative of a cell undergoing the transition to a potentially cancerous cell. The extensively diverse nature of cancer results in different patients displaying widely different tumor characteristics. Furthermore, the heterotypic nature of tumors results in a variety of neoplastic cells exhibiting characteristics diverse from one another within the same individual.[51-53] The unique features of cancer cells (such as the cancer hallmarks) distinguishing them from healthy cells serve as potential targets for both therapy and diagnosis.

Most individuals with malignant cancer cells remain undiagnosed until the tumor has grown large enough to display physiological disturbances. Unfortunately, for many patients at this stage the cancer has already metastasized, resulting in a poor prognosis.[54] Radiotracers that specifically target cancerous cells allow cancer to be detected at an early stage, once the mutations have occurred at the cellular level and before any structural changes occur. In both bowel and breast cancer more than 90% of patients diagnosed at an early stage will survive the disease for at least five years.[55] Furthermore, cancer targeting tracers can provide details on tumor size, tumor staging, tumor growth over time, number of tumors, therapy progression, and other useful information.[12] The hallmarks of cancer can serve as potential targets for radiotracers. Advanced metabolism, angiogenesis, uncontrolled proliferation, hypoxia and unique microenvironments are features of cancer that have been targeted by radiotracers with varying degrees of success.[18,50] The most important cancer imaging agent for PET today is 2-[^{18}F]Fluorodeoxyglucose ([^{18}F]FDG).

1.3.1. 2-[^{18}F]Fluorodeoxyglucose ([^{18}F]FDG)
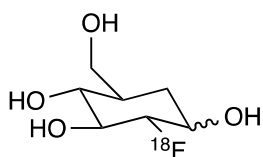
Figure 7: [^{18}F]FDG chemical structure.

Healthy cells are able to convert glucose into cellular energy, adenosine triphosphate (ATP), through two glucose catabolic pathways. The metabolic mechanism is determined by the presence or absence of oxygen in the cell, that is, whether the cell is under aerobic or anaerobic (hypoxic) conditions. Under aerobic conditions glucose is

11

initially phosphorylated and metabolized in the mitochondrial tricarboxylic acid cycle to produce carbon dioxide, water, and ATP. In contrast, under anaerobic conditions, phosphorylated glucose is metabolized to lactate for the generation of ATP. This process (glycolysis) is much less efficient than the aerobic pathway, producing only 2 mol of ATP for every mol of glucose. In comparison, the aerobic pathway produces 36 mol of ATP.[56] Cancerous cells function predominantly through glycolysis, regardless of the presence of oxygen, although many tumors do exhibit hypoxic conditions. This characteristic, known as the Warburg effect, in combination with the excessive proliferation of cancerous cells, results in the voracious consumption of glucose in relation to that of healthy tissue. [57] The high glucose uptake is often sustained through overexpression of the primary glucose transporter, GLUT1.[58-60]

After the discovery of the Warburg effect by Otto Warburg in 1924, it was surmised that the high uptake of glucose by cancer cells could be exploited to target cancer.[61] In 1968 Pacek, Tocik, and Cerny described the first synthesis of the glucose analogue, fluorodeoxyglucose (FDG).[62] FDG was designed to be taken up by the GLUT1 transporter and subsequently phosphorylated by 6-hexokinase. Once phosphorylated, however, the FDG would cease its progress in the metabolic cycle and become trapped within the cell (Figure 8). In this way, cells with overexpressed GLUT transporters would harbor an excess amount of trapped FDG. By labeling FDG with a positron emitting radionuclide, such as fluorine-18, PET scans could reveal cells with abundant [18F]FDG. The initial synthesis of fluorine-18 labeled FDG was in 1970 by Ido and Wolf.[63] In 1976 [18F]FDG was first administered into human volunteers for a PET scan of the brain by Dr. Abass Alavi and Dr. Martin Reivich.[64] [18F]FDG was ultimately approved by the FDA as a cancer imaging agent in 2000. Since its approval, [18F]FDG has become the most heavily used PET isotope for cancer imaging and encouraged the development of more cancer targeting PET radiopharmaceuticals.

Unfortunately, [18F]FDG has several limitations and therefore is not a universal diagnostic tool for cancer. Not all cancers show increased glucose uptake, causing [18F]FDG to present false negatives in slow growing tumors, such as prostate cancer or

neuroendocrine tumors. Additionally, [^{18}F]FDG does not distinguish between cancerous tissues and inflamed or infected tissue, giving rise to false positives.[65] Lastly, [^{18}F]FDG is not available for intracranial tumor detection due to the high baseline uptake of glucose by brain tissue. Fortunately, other radiotracers have been developed that are also capable of imaging cancer.[60]
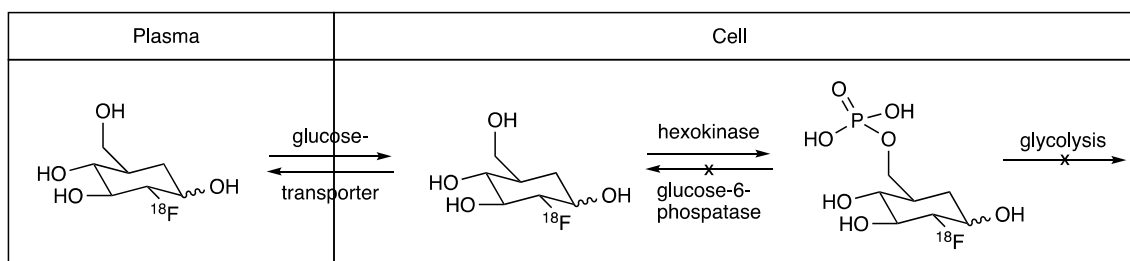
Figure 8: *In vivo* trapping mechanism for [^{18}F]FDG. [^{18}F]FDG enters the cell through the glucose transporter, is irreversibly phosphorylated by hexokinase and is then trapped within the cell due to fluorine substitution.

The success of [^{18}F]FDG has prompted the development of numerous other small molecule cancer radiotracers, with several showing clinical success. Many of these tracers, similar to FDG, are designed to exploit the rapid proliferation of cancer. Uncontrolled proliferation can results in excessive nucleoside uptake,[66] increased amino acid transport,[67 68 69 70] and sustained membrane growth.[71-73] These characteristics have been targeted through the development of [^{18}F]3'-deoxy-3'-fluorothymidine ([^{18}F]FLT), [Methyl-^{11}C] methionine ([^{11}C]met), and [^{11}C]choline, respectively. Unlike [^{18}F]FDG, [^{18}F]FLT is not subject to accumulation in inflammatory tissues,[74] however, it is characterized by relatively high uptake in the liver and bone marrow. [^{11}C]met and [^{11}C]choline have several deficiencies, namely the short half life of carbon-11, which results in the requirement of technologically advanced clinics containing both a cyclotron and PET machinery.[75] In addition to the aforementioned cancer characteristics, the rapid proliferation of cancer cells often results in oxygen demand exceeding oxygen supply, a condition further exaggerated by the lack of arterial blood sources in the center of many tumors.[76] Ultimately, these conditions lead to 50-60% of locally advanced solid tumors exhibiting hypoxic conditions.[77] The most investigated hypoxia imaging agent is Fluoromisonidazole ([^{18}F]FMISO).[78] This radiotracer acts as an oxygen mimetic, a

compound that becomes trapped within hypoxic cells. Unfortunately, due to the high lipophilicity of this compound, high muscle accumulation occurs.[79]

1.4. Nanoparticles for Cancer Detection and Therapy

1.4.1. Heterotypic Nature of Tumors

Tumor targeting agents are designed to expose the unnatural characteristics expressed by cancer cells. Recently, both cancer therapeutic and diagnostic agents have been developed to target specific cancer genes expressed within that patient's particular cancer.[80] Small molecule kinase inhibitors are an example of this 'personalized therapy.'[81] However, this personalized approach has shown serious limitations in the clinical setting. Highly specific cancer targeting is impractical for initial cancer diagnosis due to the high variation of gene expression among cancers.[51,52] Furthermore, tumors in patients are often heterotypic and the agent cannot detect all cancer cells, leaving certain metastatic sites undiagnosed. Therapeutic agents designed in this personalized therapy approach are extremely limited due to the heterotypic nature of tumors. Many treatments exhibiting success are only temporary, as the cancer acquires a resistance to the specialized therapy in most cases. One of the most successful personalized anti-cancer drugs, Herceptin, is used to treat patients with HER-2 positive breast cancer. This drug is severely limited in that only 20-30% of breast cancer patients are HER-2 positive and the drug is only effective in 20-30% of these patients. Overall the chance of success for Herceptin is low and any improvements observed are often temporary, lasting only a couple of months before the cancer becomes drug resistant.[1,82] To improve cancer therapeutics and diagnostics, better targets must be established. For an effective tumor targeting approach, especially for tumor detection and diagnosis, it is necessary to exploit a feature of cancer present in most, if not all tumors.

1.4.2. Angiogenesis

Rapidly proliferating cells require plentiful oxygen and nutrients. Eventually, as more cells are produced, new blood vessels must be recruited. Solid tumors undergoing

uncontrolled proliferation are capable of growing up to 1-2 mm before new blood vessels are required.[83] At 1-2 mm, the cells in the center of the tumor are within the diffusion range of oxygen and therefore can procure the necessary nutrients to proliferate. Small tumors of this nature are relatively common and present in many unaware individuals. Most tumors grow to this size, and then cease growth due to limited blood supply. The malnourished tumors then enter a dormant stage for long periods of time and many never resume growth.[83-85] The discovery of numerous dormant tumors during autopsies of patients further supports the notion that most tumors do not progress past dormancy.[86] For a tumor to develop beyond the blood diffusion threshold and evade dormancy, additional blood vessels must be recruited.[87]

The production of new blood vessels is a natural and necessary physiological process that can be accomplished through two means: vasculogenesis, the production of new blood vessels from angioblasts (endothelial cell precursors) and angiogenesis, the branching of new blood vessels from existing ones. Vasculogenesis is a process that occurs during embryonic development whereas angiogenesis occurs regularly throughout the lifecycle of an individual.[88] Angiogenesis is necessary for wound healing, female reproductive cycles, and physiological growth.[89] During angiogenesis, established capillaries sprout new endothelial cells to expand the vasculature network. Capillaries, which supply blood to cells, consist of three components: an interior endothelial cell layer, a basement membrane coating the endothelial cell layer, and pericytes that support the basement membrane, among other duties.[90] The angiogenic process is initiated by a cell deficient in blood supply. The malnourished cell secretes pro-angiogenic factors, predominantly VEGF-A (Table 3), which eventually diffuse through interstitial space until existing vasculature is reached. Vasculature, in opposite directions from the angiogenic center, will be signaled to grow towards one another (Figure 9). Endothelial cells within the vasculature express vascular endothelial growth factor receptor (VEGFR), capable of recognizing VEGF. Once an endothelial cell recognizes enough VEGF to surpass a threshold it becomes a tip-cell. The tip-cell expresses the receptor DLL4 (delta like canonical Notch ligand 4). The DLL4 receptor communicates with neighboring endothelial cells to ensure only a single tip cell is formed in the capillary. The tip cell forms filopodia

covered in VEGFR and encourages neighboring endothelial cells to proliferate and form a stalk. The stalk grows toward the site of VEGF secretion, guided by the VEGFR expressed on the tip cell. As the two stalks on either side of the angiogenic center grow, they eventually fuse and form a continuous capillary capable of supplying the angiogenic center with blood, resulting in the discontinuation of VEGF production. At this point the vessel is formed, the lumen opens, and the basement membrane structure is established along with pericyte localization.[91] The entire process is a temporary procedure and is carefully regulated through the balance of pro-angiogenic factors and anti-angiogenic factors (Table 3). It is important for the new capillary to fully develop, and receive support from an established basement membrane, in addition to pericyte cells. The new capillary acts as a semi-selective barrier, protecting extravascular space from unwanted particles and supplying cells with the necessary nutrients. Disturbing the angiogenic mechanism results in a multitude of vasculature complications.[92]
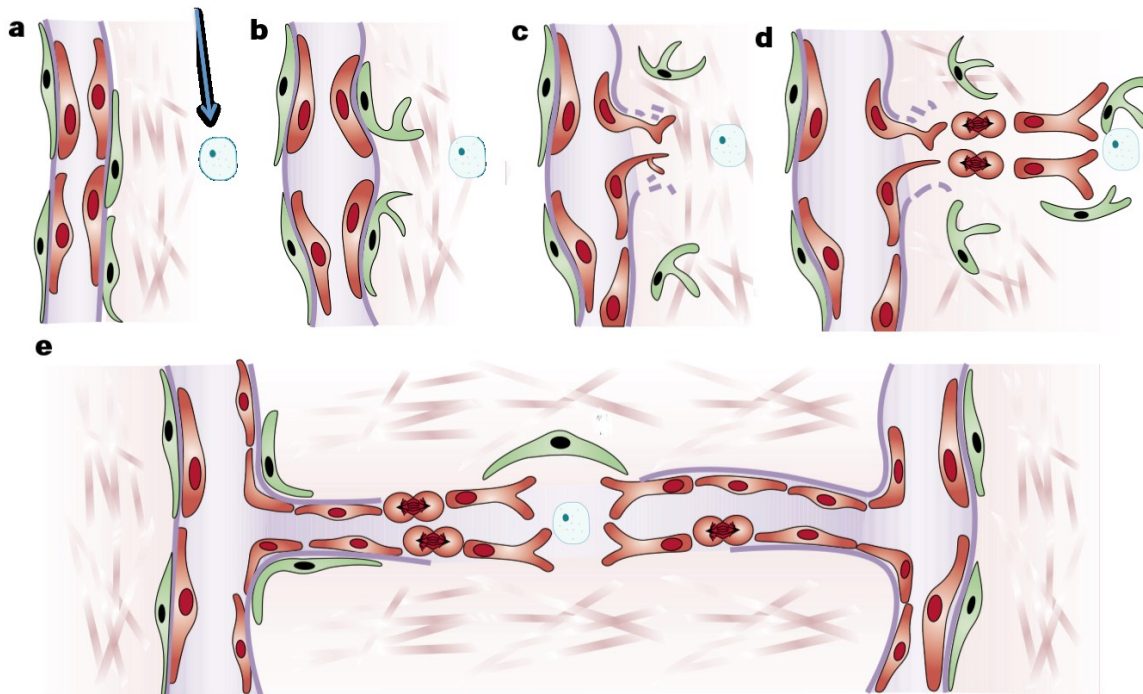
Figure 9: Angiogenic process for healthy tissue. Arrow points to angiogenic center. New capillaries are formed as a result of sprouting from pre-existing blood vessels. (a) Angiogenic center secretes pro-angiogenic factors, which diffuse through extracellular matrix until existing blood vessels are reached. (b) Pericytes (green) detach from blood vessel, followed be degradation of basement membrane and extracellular matrix. (c)endothelial cells (red) migrate towards angiogenic center. (d) Stalk forms as a result of proliferating endothelial cells. (e) Stalks from opposing sides of angiogenic center meet and form a new capillary. Figure adapted from Tumorigenesis and the angiogenic switch. [87] Permission granted through Rightslink®.

Table 3: Table of pro-angiogenic factors and anti-angiogenic factors

Pro-angiogenic	Anti-angiogenic
VEGFs, FGFs, PDGFB, EGF, LPA	thrombospondin-1, the statins, angiostatin, endostatin, canstatin, tumstatin

Data taken from Tumorigenisis and The Angiogenic Switch.[87]

      Tumors can acquire mutations that perpetually stimulate angiogenesis, thus sustaining growth beyond 2 mm.[93] Unlike the tightly regulated and organized nature of angiogenesis in healthy tissue, tumor angiogenesis is often indefinite due to the persistent presence of pro-angiogenic factors.[94] Tumors are often referred to as wounds that never heal.[95] These conditions result in excessive vasculature riddled with defects. Tumors display hypervasculature, lack of smooth muscle layer or pericytes, erratic blood flow, increased permeability, irregular endothelial cell shape, incomplete and leaky capillaries, and discontinuous or absent basement membrane.[87,96,97] O'brien*, et al*. designed an experiment to visualize the differences between tumor and healthy tissue vasculature in order to fully appreciate it's chaotic features.[98] Water-soluble acrylic resin was injected into the vasculature of both healthy and tumor bearing mice. The resulting cast was then imaged with scanning electron microscopy (SEM), as seen in Figure 10. These images depict the stark contrast between healthy and tumor vasculature. The excessive and defective vasculature is clearly visible.
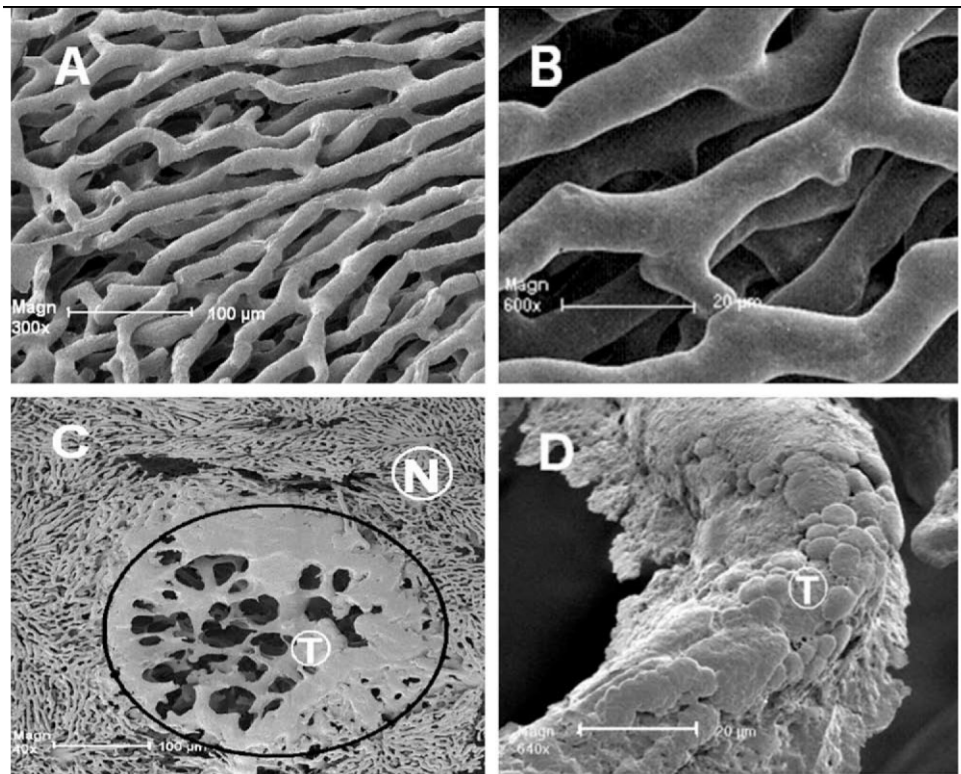
Figure 10: SEM images of healthy vasculature and tumor vasculature. A and B (top left and right) depict healthy vasculature in mice. C and D (bottom left and right) reveal the excessive and deformed nature of tumor vasculature. Image taken from Polymeric drugs for efficient tumor-targeted drug delivery based on EPR-effect. [82] Permission granted through Rightslink®.

1.4.3. The Enhanced Permeability and Retention (EPR) Effect

The unique condition of the tumor vasculature results in the deposition of various circulating particles into the tumor environment. The enhanced permeability of tumor vasculature, in conjunction with excessive vascularization and chaotic blood flow, allows large macromolecules, which would normally be unable to penetrate capillary walls, to extravasate and accumulate in solid tumor tissue. Typically, endothelial gaps in capillaries are no larger than 5 nm in diameter, whereas tumor vasculature gaps have been found to be as wide as 400 nm and larger.[99,100] Interestingly, the vasculature is not the only aberrant transportation vessel within the tumor milieu. Lymphatic drainage within the hyper-pressurized tumor is often severely impaired. As a result of this condition, tumors are unable to remove foreign particles from their environment as effectively as normal tissue. Consequently, foreign particles are retained for long periods (up to weeks at a time).[101]

These two unique features are prominent in a majority of malignant solid tumors and starkly contrast the state of healthy tissue. The outcome of these two conditions is termed the enhanced permeability and retention (EPR) effect. This phenomenon results in nanometer sized particles permeating the tumor vasculature and persisting for long periods of time. These 'nanoparticles', which utilize the EPR effect, can be applied to target most solid tumors for both diagnosis and therapeutic endeavors.[102] The EPR effect is a phenomenon present in almost all human cancers, excluding hypovascular tumors such as prostate or pancreatic cancer.[82] The EPR effect provides a promising target for cancer research and presents improvements over several established tumor targeting methods. Inflamed or infected non-cancerous tissue often presents similar characteristics to cancer and can complicate the results for tumor targeting tracers such as [^{18}F]FDG.[65] However, NPs designed to exploit the EPR allow differentiation of tumors from inflamed tissue due to the intact lymphatic drainage present in non-cancerous tissue.[102] Tissues inflamed or infected will accumulate large particles, but should still be able to clear unwanted particles: a capability that tumor tissue often lacks.[102] NPs have incredible promise as a cancer-imaging agent. The inherent ability of NPs to exploit the EPR effect have shown improvements in tumor targeting over [^{18}F]FDG. *Zhao, et al.* demonstrated that their gold NPs and [^{18}F]FDG exhibited identical tumor to muscle uptake after one hour in mice. However, after one hour, NP uptake continued to increase resulting in triple the uptake of [^{18}F]FDG at 24-hours p.i. (Figure 11).[103]
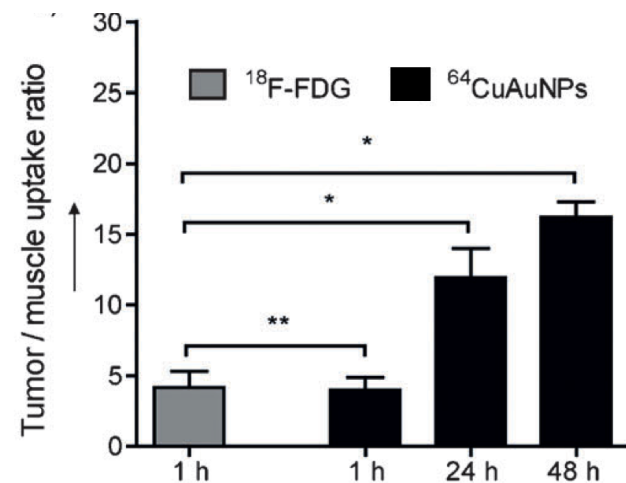
Figure 11: T/M comparison of [^{18}F]FDG and ^{64}AuNPs. At 1-hour both [^{18}F]FDG and ^{64}AuNPs display similar T/M values. However, at 24-hours p.i. and 48-hours p.i. ^{64}AuNPs expresses a much higher T/M value. Image taken from Copper-64-alloyed gold NPs for cancer imaging: improved radiolabel stability and diagnostic accuracy.[103] Permission granted through Rightslink®

19

1.4.4. Nanoparticles Utilized as Tumor Targeting Agents

Maeda, et al. were the first to describe the EPR effect and the inherent nature of NP accumulation in the tumor environment.[104] Their findings determined that large particles, such as SMANCS (styrene-maleic acid conjugated neocarzinostatin NPs), would accumulate in tumors much more effectively than their low molecular weight counterparts. Through a series of experiments, they realized that all macromolecular drugs over 40 kDa had significantly higher tumor accumulation. NPs (particles ranging from 10 nm to 100 nm in diameter in at least two dimensions) are too large to penetrate the endothelial gaps in healthy tissue (< 5 nm), but are small enough to penetrate the large gaps commonly found within the tumor vasculature (~200 nm) (Figure 12). Indeed, NPs present the inherent ability to exploit the EPR effect, but there are a multitude of factors that influence tumor accumulation.[105,106] Foremost, NPs must exhibit long blood circulation time to fully exploit the EPR effect and maximize tumor accumulation.[107 108,109] Blood circulation half-life for NPs is influenced by the propensity to avoid the blood clearance systems. Both the renal system, and the reticuloendothelial system (RES) are the primary mechanisms through which foreign particles are removed from the blood.
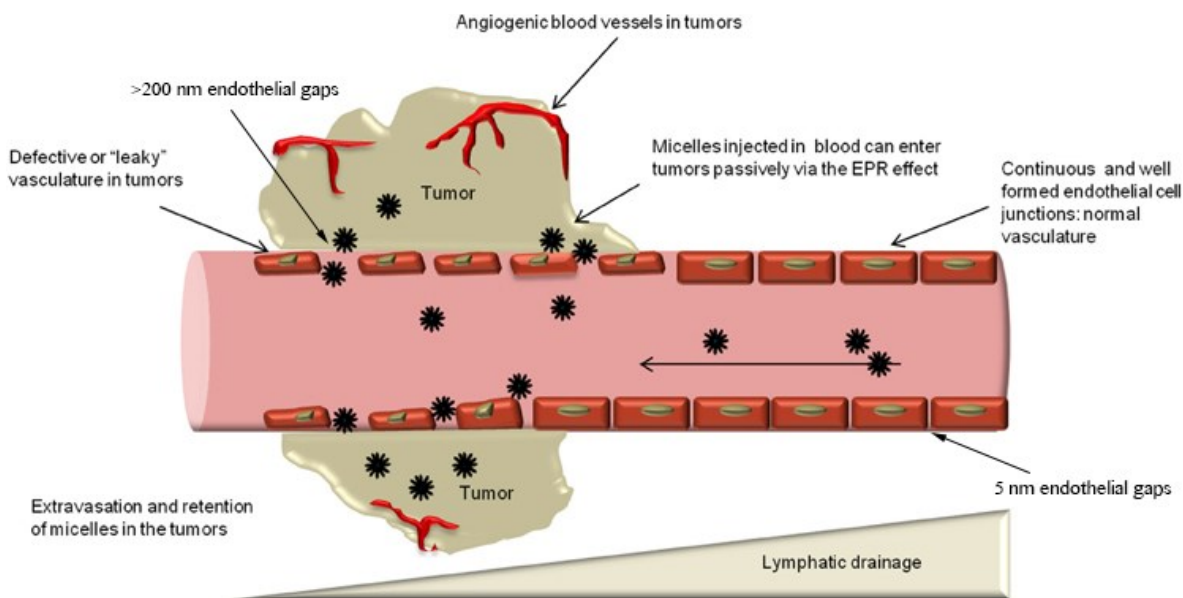
Figure 12: Diagram of healthy vasculature versus tumor vasculature. Tumor tissue has defective vasculature with large endothelial gaps and poor lymphatic drainage among. Figure adapted from Multifunctional polymeric micelles for delivery of drugs and siRNA.[110] Permission granted under Creative Commons Attribution license.

The renal filtration system is capable of removing most small, hydrophilic particles from the cardiovascular system. The kidneys are able to filter certain foreign particles efficiently due to minimal cell internalization, and a timely transfer of particles to the bladder where they are excreted as urine.[107,109] As blood enters the kidneys, it travels through the afferent arteriole to the glomerulus where the principal renal filtration occurs. Inside the glomerulus are the glomerular filtration channels, which can remove particles below a certain size threshold. The channels are capable of removing a majority of circulating particles lighter than ~40 kDa.[111] *In vivo* NP studies by *Choi, et al.* elucidated how the size threshold affects NPs with a defined diameter. It was determined that quantum dots with a hydrodynamic diameter smaller than 5.5 nm and were vulnerable to the glomerular filtration channels and thus removed from circulation.[109] Therefore, for minimal renal clearance and prolonged circulation, NPs must be above the 5.5 nm threshold to successfully exploit the EPR effect.

NPs larger than 5.5 nm are capable of evading the renal clearance system. However, many of these larger NPs are susceptible to blood clearance by the RES. Circulating NPs are subject to adsorbance by opsonins such as immunoglobins, complement proteins, albumin, apolipoprotien and fibrinogen.[112] Opsonization marks foreign particles for internalization by the mononuclear phagocytic system and subsequent elimination from the blood supply by the liver. Numerous studies have been conducted to determine the NP properties that influence hepatic clearance.[105,107,108,113] The primary influence on NP circulation and susceptibility to RES clearance mechanisms are NP size and surface charge. *Choi, et al.* established that as NPs increase in size, they are more likely to be targeted for opsonization.[109] Furthermore, several studies have shown that high surface charge, particularly highly positive surface charges, have a high non-specific internalization rate by phagocytes, thus reducing blood circulation time.[114-116] Many researchers have used polyethylene glycol (PEG) ligands to reduce opsonization. This method showed success in RES evasion initially, but several studies found that PEG induces immune response, and thus rapid blood clearance, after consecutive injections.[117-119] Designing NPs under 100 nm but larger than 5.5 nm with low surface charge is optimal for maximum NP blood

circulation time. NPs with these specifications should be able to exploit the EPR effect most effectively and display high tumor accumulation.

1.4.5. Nanoparticles as Radiotracers

The extensive tunability of NPs has contributed to their appeal as diagnostic imaging agents. The ability to customize their composition, size, shape, and surface chemistry defines a highly versatile molecular tracer. Moreover, the ability to functionalize NPs with ligands provides the option to compliment the NP's inherent abilities. NPs can be functionalized with active targeting ligands, drugs, or radioactive nuclides. Functionalizing NPs with positron emitting nuclides provides a reliable manner for *in vivo* assessment. Through PET imaging it is possible to visualize NP organ distribution, blood circulation half-life, and tumor accumulation. This information is invaluable in assessing NP viability as a cancer targeting agent.

PET imaging of radiolabeled NPs provides quantifiable data on blood clearance, organ distribution, brain uptake, and tumor uptake. Numerous NP radiolabeling methodologies have been established. Many of these NPs have been injected into animal models to study their *in vivo* behavior as well as tumor targeting ability. Several types of NPs have been radiolabeled in attempt to further understand the *in vivo* behavior including gold NPs, metal oxide NPs, silica NPs, and polymer NPs.

Gold NPs have received significant attention in nanomedicine due to their long established synthetic procedures and ease of size and shape customization. Furthermore, the ability to synthesize monodisperse NPs allows for more accurate *in vivo* studies.[120] The inherent affinity of gold for thiol groups enables easily functionalized gold NPs. *Schirrmacher, et al*. exploited the gold-thiol chemistry by functionalizing gold NPs (3.2 nm ± 0.5 nm) with PEG modalities capped with the radiolabeling technology, Silicon-fluoride acceptor (SiFA). The SiFA enabled simple and rapid isotopic exchange of fluorine-19 on the SiFA unit with fluorine-18. The radiolabeled gold NPs were then injected into healthy rats and analyzed with PET over 2-hours. The gold NPs were able to

cross the blood brain barrier and accumulate in the brain, a feat few NPs have been able to accomplish.[121] Several gold NPs have been labeled with longer-lived radioisotopes to determine a long-term biodistribution profile. 7.7 ± 0.2 nm gold NPs were labeled with indium-111 and injected into U87 glioblastoma tumor bearing mice. At 4-hours p.i. tumors displayed an accumulation value of 0.37 ± 0.14 %ID/g. To determine if active targeting could enhance the EPR effect, NPs were labeled with the $\alpha_3\beta_v$ integrin targeting cRGD ligand. Results revealed a substantial increase in tumor accumulation: up to 0.83 ± 0.14 %ID/g. In regard to blood clearance mechanisms, these NPs showed high liver accumulation and low kidney accumulation.[122] A separate study involving hollow gold nanospheres injected copper-64 labeled versions into tumor bearing rabbits. 4-hours after intra-arterial injection, tumor accumulation reached 0.33 %ID/g.[123] Finally, to assess the relative value of NPs as a tumor imaging agent, *Zhao, et al*. compared tumor uptake in EMT-6 tumor bearing mice with the gold standard of tumor PET imaging, [^{18}F]FDG. Copper-64 radiolabeled gold NPs of 27 nm were injected and results were assessed at multiple time points. At 1-hour p.i., both [^{18}F]FDG and the NP showed near identical tumor accumulation (4.59 ± 0.43 %ID/g and 4.90 ± 0.32 %ID/g respectively); however, after 48-hours the NP displayed substantially better numbers, 16.8 ± 0.98 %ID/g (Figure 19).[103] These results show the incredible promise of NPs as tumor-imaging agents.

Metal oxide NPs present diverse application in the diagnostic field due to the inherent magnetic properties. The magnetic properties allow utilization as a contrast agent in MRI. Radiolabeled metal oxides enable a dual modality approach to study NP biodistribution. Combining MRI and PET allows the strengths of both technologies to be utilized while compensating for the shortcomings of each. Many metal oxide NPs are relatively large (>50 nm) and insoluble.[124] Therefore, metal oxide NPs must be modified with hydrophilic moieties such as PEG, or cysteine. Interestingly, in a study conducted by *Sharma, et al*. 16 nm iron oxide NPs were labeled with carbon-11. Typically NPs are radiolabeled with longer lived nuclides, due to the slow kinetics of the EPR effect. Unfortunately, in this experiment the carbon-11 NP radiosynthesis had poor radiochemical yield (0.3 %) and very high liver uptake was observed when injected into healthy mice.[125] Two separate studies involved radiolabeling iron oxide NPs with copper-64. The first

study, by *Xu, et al*. radiolabeled a 71.6 nm ± 3.8 nm NOTA-RGO-IONP-PEG-PEG and observed tumor uptake over 48-hours. 4T1 murine breast cancer models were studied in these mice. PET scans were performed at 0.5-, 3-, 6-, 24- and 48-hours with tumor accumulation steadily increasing at each time point (2.8 ± 0.5, 4.3 ± 0.8, 5.3 ± 1.2, 12.0 ± 2.0, and 15.5 ± 12 %ID/g respectively). Due to the large size of these NPs, high liver uptake was observed which remained relatively constant through the time points (Figure 13).[124] A second PET study involved copper-64 radiolabeled iron oxide NPs and used U87MG glioma tumor model mice. Iron oxide NPs were coated with dopamine and human serum albumin to increase solubility. The final hydrodynamic diameter was 29.4 ± 1.2 nm. Scans were performed at 1-, 4- and 18-hours p.i.. with tumor uptake of 5.46 ± 0.64, 6.11 ± 0.7 and 8.45 ± 0.86 %ID/g respectively. Liver uptake was high with a liver/muscle ratio of 28.3 ± 2.9.[126] A HT-29 xenografted mouse study involved gallium-68 radiolabeled 66 nm iron oxide NPs. PET scans displayed high liver uptake with moderate tumor accumulation (3.07 ± 0.76 %ID/g at 1-hour p.i.).[127]
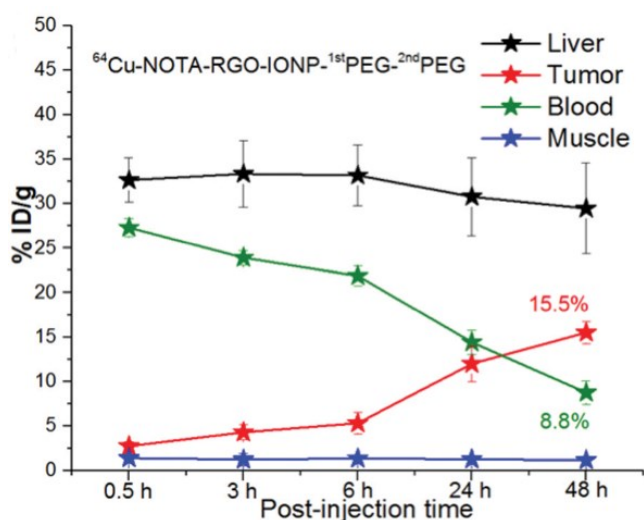
Figure 13: Graph of %ID/g for iron oxide NP accumulation in various tissues and organs as a function of time from 0- to 48-hours p.i.. Liver (black), tumor (red), blood (green) and muscle (blue). Figure taken from Long Circulating Reduced Graphene Oxide-Iron Oxide NPs for Efficient Tumor Targeting and Multimodality Imaging. [124] Figure reproduced from Ref. 162 with permission from The Royal Society of Chemistry.

Silica NPs hold high value in nanomedicine due to a variety of favorable synthetic and biocompatible factors.[128] Silica NPs have several simple and established syntheses which can yield monodisperse NPs, are easily modified with functional ligands, and have favorable biocompatibility.[129,130] Ultrasmall (<10 nm) silica NPs designed by *Benezra, et al*. offer insight into the value of NPs cleared by renal filtration. For an imaging agent to be approved by the FDA it must be cleared from the body within a reasonable time frame.

7 nm Cysteine dye encapsulating core-shell silica NPs coated with PEG were radiolabeled with iodine-124 to determine the long term biodistribution of NPs in M21 xenografted tumor mice. Both active and passive tumor targeting were assessed for this silica nanoparticle. Functionalizing NPs with cRGDY allowed active targeting of $\alpha_v\beta_3$ integrins overexpressed in these tumor models. As expected, both ultrasmall NPs showed high renal clearance. Urine studies revealed that half of the injected NP dose was excreted within the first 24 hours, and 72% by the 96th hour. Tumor examination revealed highest accumulation for the active targeting nanoparticle, RGDY-PEG-dot, at 4-hours (2.0 %ID/g) which slowly decreased to 0.5 %ID/g over the next 92-hours. The non-targeted variation showed highest tumor accumulation at 1-hour p.i. (1.0 %ID/g) and steadily decreased to negligible amounts at 96-hours p.i..[128] The decrease in tumor accumulation over time is contrasting with most current NP studies, but can be attributed to the high renal clearance rate of these particular NPs. Efficient renal clearance results in a shorter blood pool half-life and therefore limits contact with tumor vasculature.

Larger (175 nm) mesopourus silica NPs were prepared by *Chen, et al.* and radiolabeled with copper-64. Both passive and active tumor targeting were examined in this experiment. The active targeting silica NP was functionalized with TRC105, which targets CD105, a vascular specific marker for tumorgenesis. Both NPs were injected into 4T1 murine breast cancer mice and *in vivo* PET imaging was performed. High liver uptake was observed in both instances. The passive targeting NP displayed moderate uptake at 4-hours p.i. (2.0 %ID/g), whereas there was a marked increase in tumor uptake for the active targeting TRC105 nanoparticle, displaying 5.4 ± 0.2 %ID/g at 4-hours with a muscle to tumor ratio of 7.3 ± 1.1.[131] This study clearly reveals the potential of NPs in tumor imaging and highlights the increased tumor accumulation possible via active targeting.

Polymeric nanoparticles (PNPs) have emerged as a dominant division of nanomedicine and have shown incredible promise. PNPs can be easily synthesized with almost unlimited polymer groups to fine tune size, surface charge, or functionality. PNPs can be synthesized inherently soluble, removing the necessity for PEG groups. Furthermore, many PNPs are designed as drug carriers, encapsulating chemotherapy drugs.

PNPs are perhaps the most diverse array of NPs, encompassing lipid nanoparticle, liposomes, micelle NPs, and amphiphilic block copolymer NPs.

Many NPs are being developed utilizing self-assembling block copolymers. *Starmans, et al.* synthesized micelles assembled via polymers and acrylic acid residues, functionalized with [89]Zr-deferoxamine (25 nm). The PNPs were injected into LS174T (human colon carcinoma) tumor mice. Biodistribution showed very high liver and spleen uptake with tumor accumulation of 6.1 ±1.5 %ID/g at 48-hours p.i. (Figure 14).[132] *Jensen, et al.* designed triblock polymeric micelles and radiolabeled them with copper-64. Copper-64 was chelated to NPs through two agents to compare *in vivo* stability and tumor uptake. Chelating agents, DOTA and TETA were attached to NPs with a final diameter of 33 nm and 36 nm, respectively. The surface charge of each NP was then measured with an effective nuclear charge of -2.3 mV for the DOTA chelated nanoparticle, and -3.5 mV for the TETA chelated nanoparticle.[133] Both radiolabeled NPs showed moderate liver uptake with slightly less kidney uptake. Furthermore, both tracers showed identical tumor uptake at 1-hour, 1.9 ± 0.10 %ID/g and slowly increased to 4.9 ± 0.4 for TETA and 3.6 ± 0.11 for DOTA at 46-hours p.i..
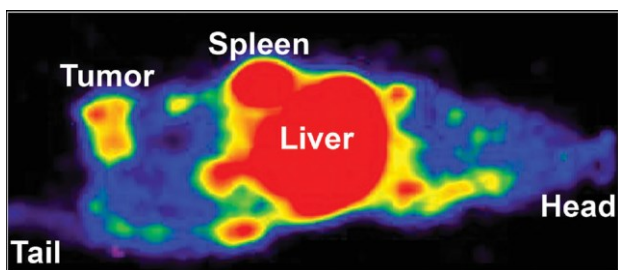
Figure 14: PET image of tumor bearing mice with zirconium-89 labeled polymeric micelle at 48-hours p.i.. Red depicts higher radioactivity. Spleen, liver and tumor all revealed high PET signal. Image from 89 Zr- and Fe-Labeled Polymeric Micelles for Dual Modality PET and T1 -Weighted MR Imaging.[132] Permission granted through Rightslink®.

Medina, et al. demonstrated the value of radiolabeled NPs by predicting the efficacy of established cancer drugs. Their nanoparticle, termed the Nanoreporter (NREP), was able to predict the efficacy of doxil, an FDA approved anti-cancer nanotherapy. The study revealed a strong correlation (r=0.96, P<0.0001) between the %ID/g of both agents in breast cancer mice models. The strong correlation can be attributed to the similar size and zeta potential between the two NPs, resulting in similar EPR effects.[134] *Hansen, et al.*

conducted a unique study using 11 family owned dogs with spontaneously formed tumors. Liposomes radiolabeled with copper-64 were used to study the various tumors. Radiochemical yield for NP labeling was high at 98%. The NPs final hydrodynamic diameter was 110 ± 5 nm with a surface charge of -7 ± 3mV. Results from the study were quite diverse (Table 4), outlining the unpredictable nature of the EPR effect. Interestingly, dog 1 and dog 10, both with intranasal squamous cell carcinoma, showed highest NP uptake.[135] These findings are supported by a SPECT study by *Harrington, et al*. where 111-indium labeled liposomes were injected into 17 patients with locally advanced cancers. The study found tumor uptake decreased with tumor size and highest accumulation was found in squamous cell carcinoma. Moderate uptake occurred in lung cancer tumors, and the lowest NP uptake was seen in breast cancer tumors.[136]

Table 4: NP accumulation in tumor bearing dogs

Dog	BW(kg)	Tumor Type	Tumor Volume (cm³)	Tumor Location	SUVmean (1-hour p.i.)	SUVmean (24-hours p.i.)
1	39	SCC	4.0	Intranasal	2.1	6.1
2	28	AC	274.5	Mammary glands	0.7	1.3
3	25	AC	19.4	Submandibular	1.3	1.6
4	12	STS	32.6	Masticatory muscle	0.5	0.4
5	25	STS	10.5	Neck muscle	0.6	0.4
6	32	LS	4.8	Ante-brachium	0.8	0.6
7	33	TCC	22.0	Intranasal	1.4	2.6
8	27	STS	10.1	Front paw	0.6	0.3
9	10	AC	7.1	Mammary glands	0.7	0.7
10	13	SCC	8.0	Intranasal	1.3	2.9

p.i. = p.i.. BW = body weight. Data taken from Positron Emission Tomography Based Elucidation of the Enhanced Permeability and Retention Effect in Dogs with Cancer Using Copper-64 liposomes. [135]

Radiolabeling previously established NPs can help elucidate further pharmacokinetic information which can be used to prove efficacy and safety through biodistribution studies. IT-101, a cyclodextrin polymer-based nanoparticle, loaded with camptothecin is currently under clinical development. *Schluep, et al*. radiolabeled IT-101 with copper-64 through the DOTA chelating ligand. The final size of the radioisotope was determined to be 30-40 nm in diameter. PET studies revealed that tumor accumulation increased from 4.6 %ID/h at 1-hour to 11.0 %ID/g at 24-hours p.i.. It was found that at 24-hours, the NP concentration in the tumor surpassed the NP concentration in the blood.

Organ uptake displayed liver accumulation was relatively low and did not increase over time.[137]

Radiolabeled NPs have proven to be successful in preclinical studies and in 2014 the first clinical study of a radiolabeled NPs was. Cornell dots (C-dots) functionalized with PEG, cRGDY and iodine-124, synthesized by *Phillips, et* al. were approved by the FDA for an investigational new drug approval as a drug for targeted molecular imaging of integrin-expressing cancer. The clinical study was conducted in five patients exhibiting metastatic melanoma. These NPs were 6-7 nm in hydrodynamic diameter. Results were favorable with efficient urinary clearance, and good *in vivo* stability. Furthermore, although it was not the focus of the study, several patients exhibited lesion uptake. Tumor data from patient #2 is expressed in Figure 15. This study has incredible significance, as it paves the way for more radiolabeled NPs to undergo investigation in clinical trials.[138]
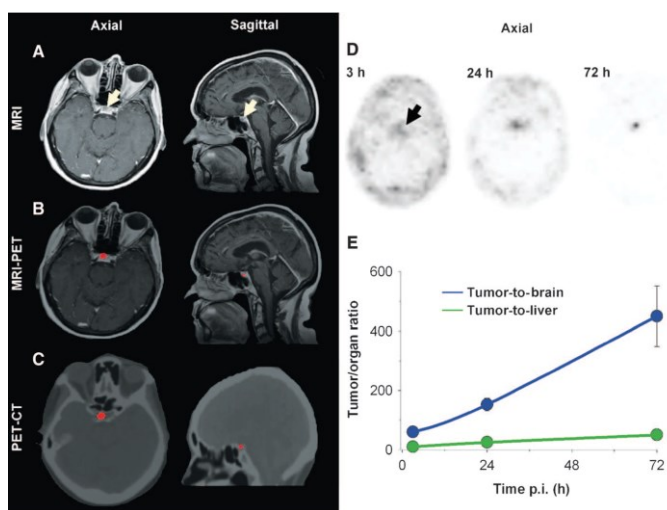
Figure 15: Clinical brain PET scan for ultrasmall inorganic NPs. PET brain scan results from clinical translation of an ultrasmall inorganic optical-PET imaging NP probe. Arrows point to subcentimeter cystic focus (A) imaging 72-hours after NP injection. (B) MRI-PET (C) PET-CT (D) axila PET images of ^{124}I-cRGDY-PEG-C dots in the brain 3-, 24- and 72-hours p.i.. Study found higher tumor-to-brain activity observed as time went on. (E) time (hours) vs tumor/ organ ratio for ^{124}I-cRGDY-PEG-C dots. Image taken from Clinical translation of an ultrasmall inorganic optical-PET imaging NP probe. [138] Permission granted through Rightslink®.

1.5. Labeling Nanoparticles with Fluorine-18

Fluroine-18 has become the most heavily studied radionuclide in PET imaging. Over the past decade several protocols have been utilized for fluorine-18 labeling of NPs.[139-147] Two paradigms are available for NP labeling: indirect radiolabeling and direct radiolabeling. Indirect fluorine-18 labeling of NPs requires a multistep process, often

requiring the use of HPLC. This can result in a long synthesis time and therefore substantial fluorine-18 decay. These methods often involve the use of a prosthetic group being labeled before incorporation into the nanoparticle. *Borros, et al.* radiolabeled polyester-based NPs in this way: first synthesizing the labeling agent 4-[^{18}F]fluorobenzy-2-bromoacetamide ([^{18}F]FBBA), which was then used to label block copolymers, and then finally used to synthesize the polymer NPs (Figure 16).[139] This entire process required 120-230 minutes (fluorine-18 half life:109 min), resulting in low radiochemical yields (RCY). Several other NPs have been radiolabeled through indirect labeling and many involve the exploitation of N-succinimidyl 4-[^{18}F]fluorobenzoate (SFB), an NHS-ester (Figure 17).[141,143,148] Alternatively, NPs can be labeled with fluorine-18 directly in a 1-step method. Most of these methods require harsh reaction conditions such as high reaction temperature, and low pH.[147] Robust iron oxide NPs were designed to withstand these conditions and labeled with fluorine-18 through a procedure based on the formation of a complex between aluminum fluoride ([^{18}F]AlF) ions and 1,4,7-triazacylononane (NOTA) chelators.[146] Unfortunately, this method is severely limited in that many particles would be compromised under these conditions. Direct radiolabeling of NPs can be accomplished under mild conditions through the silicon-fluoride acceptor (SiFA) isotopic exchange functional group.
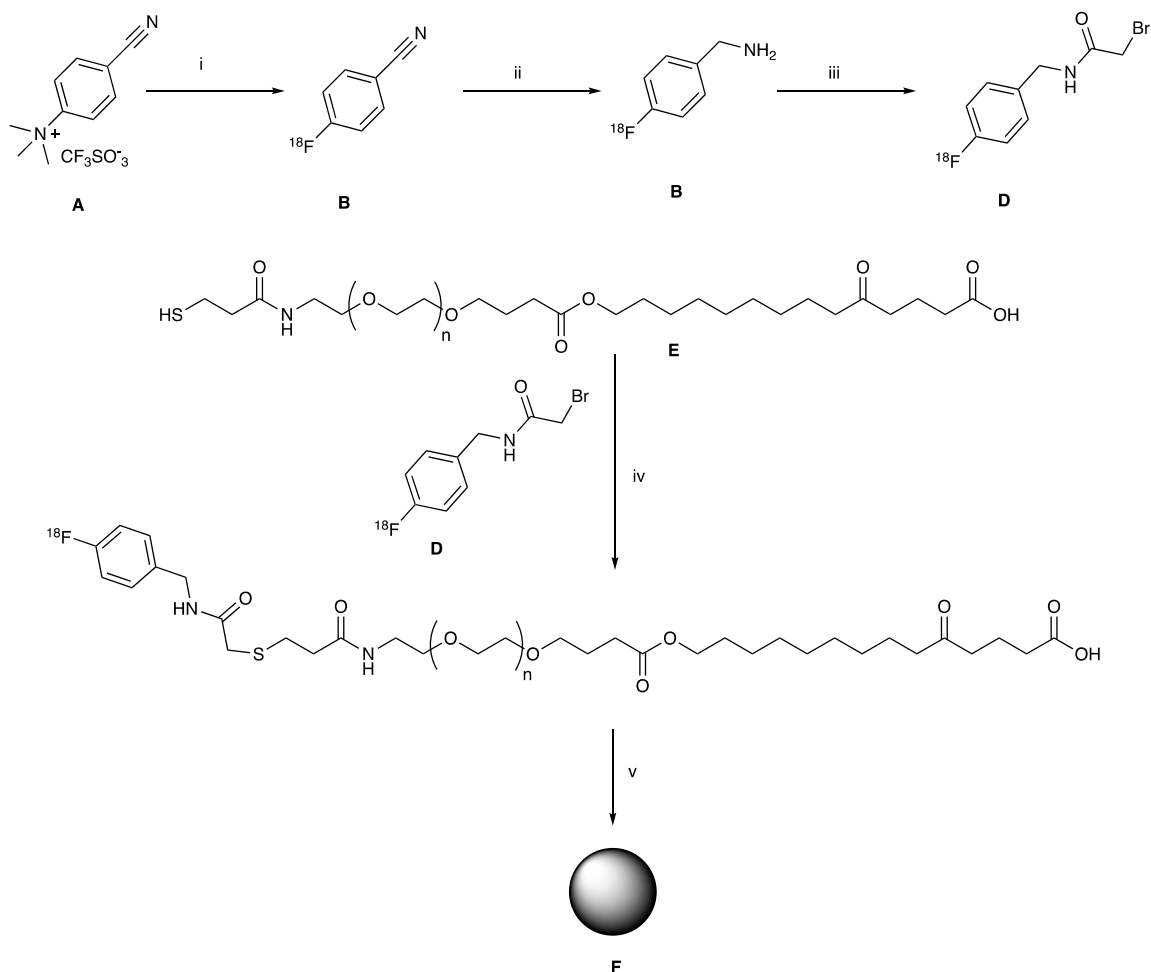
Figure 16: Indirect fluorine-18 labeling method for polyester-based NPs. i) azeotropically dried [^{18}F]F$^-$, K_2CO_3, $K_{2.2.2.}$,MeCN, 130°C, 10 min, ii) 0.1 M $LiAlH_4$, 2 min, 120 C (iii) bromoacetyl bromide in CH_2Cl_2, 2 min, RT, followed by HPLC iv) PBS / MeCN, 90°C 30 min, followed by HPLC. v) Polymerization to form NPs.[139]
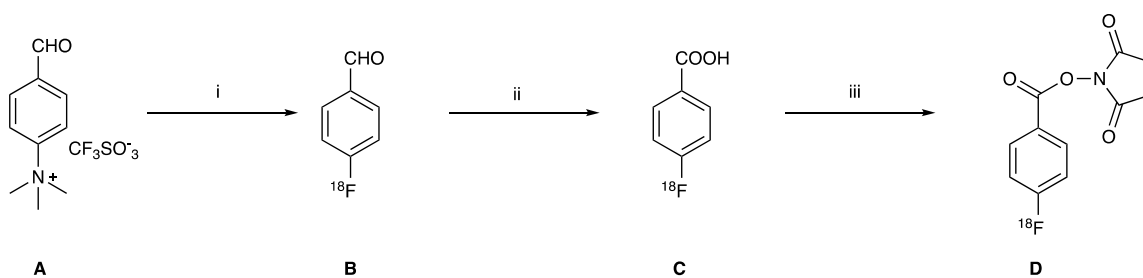
Figure 17: Synthesis of N-succinimidyl 4-[18F]fluorobenzoate. i) Kryptofix 222, fluorine-18 , DMSO, 120–140°C; ii) $KMnO_4$, NaOH, 120°C; iii) DSC, pyridine, CH_3CN, 150°C. **D,** [^{18}F]SFB is then used to conjugate to particle of interest.[148]

The SiFA functional group was developed by the Schirrmacher and Jurkschat Research Groups in 2006 and allows for direct labeling with fluorine-18 through simple isotopic exchange.[149] The isotopic exchange is facilitated by the unique chemical bond

between fluorine and silicon. Silicon and fluorine have a high affinity for one another, which leads to a strong bond (565 Kj•mol^{-1}). However, this bond is highly polarized and therefore kinetically labile. Typically silicon-fluorine bonds are subject to hydrolysis *in vivo,* especially under basic conditions. The SiFA functional group makes use of two silicon bonded *tert*-butyl groups to decrease the Lewis acidity of silicon and increase the steric hindrance, resulting in a kinetically stable silicon-fluoride bond.[36] SiFA can be attached to the NP of interest via bioconjugation, resulting in a particle ready for radiolabeling through isotopic exchange when required. Radiolabeling is performed in a rapid 1-step process under mild conditions (Figure 18). Furthermore, this process does not result in the formation of side products, obviating the requirement for HPLC purification.
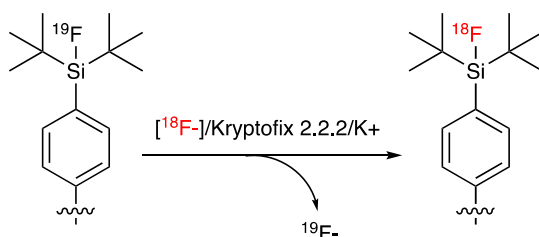
Figure 18: Silicon-Fluoride Acceptor isotopic exchange (SiFA-IE) technology. Through this modality, radiolabeling can be completed through the simple isotopic exchange of fluorine-19 with fluorine-18 ions.

1.6. Concluding Remarks, Hypothesis and Objectives

Exploiting the EPR effect offers a unique opportunity to target the inherent nature of solid tumors. NPs, due to their unique size relative to most biological molecules, provide an ideal candidate to expose this mechanism. Radiolabeling NPs enables high resolution tracking of *in vivo* biodistribution. PET imaging of radiolabeled NPs can provide information on blood pool half-life, blood clearance mechanisms, and organ uptake. Furthermore, injection of radiolabeled NPs into tumor bearing live subjects allows further understanding of tumor uptake and retention. Currently, considerable research has gone into NPs and the EPR effect. It is apparent that the degree of tumor accumulation observed is dependent on a multitude of factors, including NP size, tumor size, NP surface charge, and tumor type. However, there is still much uncertainty on how the size of NPs influences tumor uptake. Several studies have been published with varying results further enhancing

the ambiguity of this phenomenon. Polymer NPs, synthesized from subunits functionalized with radiolabeling modalities, would provide easily radiolabeled NPs for *in vivo* studies. Furthermore, due to the tunable nature of polymer NPs, a range of polymer NPs of distinct sizes could be used to further understand the relationship between the EPR effect and NP size.

We hypothesize that NP uptake by tumors should be influenced by NP size. Moreover, there should be a NP size or size range, which is best able to take advantage of the EPR effect in a specific biological system or tumor model. It is possible this size could be correlated to the average fenestration size of tumor vasculature. In addition, provided the NPs are above the renal filtration threshold, tumor accumulation of NPs should increase over time. Thirteen PNPs conjugated with SiFA building blocks were prepared to allow for simple and rapid fluorine-18 labeling. Optimal radiolabeling and purification techniques were obtained for all NPs. Optimal PNP candidates were then chosen for up scaling radiolabeling and injection into EMT-6 tumor bearing female BALB/c mice. PET scans were then performed to assess the ^{18}F-PNPs biodistribution.

2. Results and Discussion

2.1. Choice of Polymer Nanoparticles as Object of Study

For our experimental objectives it was necessary for the NPs to be soluble in a variety of solvents suitable for radiolabeling, have specific size tunability, and be easily functionalized. PNPs were chosen to explore the EPR effect. PNPs are composed of individual polymer subunits, which are cross-linked to form stable NPs. The chemical makeup of the subunits predominantly determines the PNPs physical properties, which allows fine-tuning of the PNPs.[150] In this way PNPs can be synthesized at desirable sizes and easily functionalized with specific modalities. Furthermore, most PNPs display low inherent toxicity and have already shown success in the relatively new field of nanomedicine.[132-136] The Weberskirch group and the Jurkschat Group, who both reside at the Technical University of Dortmund, Germany, synthesized the PNPs for this study.

PNPs were synthesized using self-assembling amphiphilic block copolymers through a microemulsion technique.[150]

2.2. Choice of Polymer Nanoparticle Size

To maximize PNP exposure with the tumor vasculature long blood circulation and tumor retention is required.[107-109] Successful NPs must avoid both renal and hepatic clearance. Renal clearance studies involving quantum dots revealed that NPs below 5.5 nm are filtered from the blood by glomerular filtration channels.[109] Furthermore, it has been shown that there is a positive correlation between NP size and targeting by opsonization proteins. NPs subject to opsonization will be cleared from the blood pool through hepatic clearance.[109] Therefore, a range of PNPs of distinct sizes from 10 to 130 nm were synthesized. This array of PNPs will be able to avoid clearance by the glomerular filtration channels and provide information on the optimal size for hepatic evasion. Furthermore, this size range should be proficient at penetrating the large fenestrations within the tumor vasculature while avoiding the less than 5 nm endothelial gaps present in healthy tissue [99,100]

2.3. Choice of Radiolabeling Methodology

Fluorine-18 decays almost entirely by positron emission (97%) and has a half-life (109 minutes) capable of imaging the EPR effect over several hours. Positrons emitted by fluorine-18 have relatively low energy resulting in a shorter travel distance in tissue and thus provide better PET resolution than nuclides that emit positrons of higher energy. Furthermore, fluorine-18 is readily available through most medical cyclotrons and has established radiolabeling protocols.[27] Radiolabeling PNPs with fluorine-18 through a rapid 1-step procedure is important to developing a potential clinical tumor-targeting/ imaging agent. There are numerous fluorine-18 methodologies that have proven to be effective for ^{18}F-labeling of PET radiotracers. However, many methods require several steps or harsh labeling conditions.[39] The Silicon Fluoride Acceptor isotopic exchange (SiFA IE) methodology developed by Schirrmacher and Jurkschat in 2006 is highly appealing for labeling our PNPs. The SiFA technology utilizes the isotopic exchange approach as opposed to a leaving group-radiolabeling method and therefore high-performance liquid

chromatography (HPLC) is not necessary, allowing for a simple purification.[149] Functionalizing polymer subunits with the SiFA technology resulted in PNPs coated with a multitude of ^{18}F-labeling sites.[149]

2.4. Solubility of PNPs

The successful radiolabeling of the PNPs is contingent on their solubility in suitable solvents capable of facilitating the isotopic exchange reaction such as acetonitrile. Furthermore, PET imaging requires that the PNPs be soluble in an injectable solution, such as saline or buffer. Therefore, it was necessary to characterize the solubility of each PNP in a variety of solvents. NPs have different solubility characteristics than small molecules. Interparticle interactions are not additive and the molar volumes of NPs are orders of magnitudes larger than that of small molecules. NPs dissolved in a solvent form a colloidal suspension with two physical phases in equilibrium. The two phases consist of a supernatant with single NPs dispersed in the solvent and a solid phase of aggregated NPs.[151] The solubility of the PNPs in ethanol, water, and acetonitrile are displayed in Table 5. Most PNPs were soluble in ethanol and water. For PNP1, PNP5-PNP14 highest solubility was observed in ethanol. PNP2 showed good solubility in all solvents and PNP3 was only soluble in water, preventing a successful isotopic exchange reaction in ethanol or acetonitrile.

Table 5: Table of PNP solubility

PNP	Size in water (nm)	MeCN	EtOH	Water
PNP1	33.65	Not soluble	Soluble	Poorly soluble
PNP2	19.61	Soluble	Soluble	Soluble
PNP3	4.89	Not soluble	Not soluble	Soluble
PNP5	32.81	Poorly soluble	Soluble	Soluble
PNP6	45.12	Poorly soluble	Soluble	Soluble
PNP7	71.9	Poorly soluble	Soluble	Soluble
PNP8	40.12	Poorly soluble	Soluble	Soluble
PNP9	91.54	Poorly soluble	Soluble	Soluble
PNP10	93.56	Poorly soluble	Soluble	Soluble
PNP11	105.5	Poorly soluble	Soluble	Soluble
PNP12	48.44	Poorly soluble	Soluble	Soluble
PNP13	62.92	Poorly soluble	Soluble	Soluble
PNP14	131.6	Poorly soluble	Soluble	Soluble

2.5. Radiolabeling Conditions

The radiolabeling of PNPs with fluorine-18 was enabled by the SiFA technologoy present on individual PNP subunits. Therefore, each PNP has a multitude of potential labeling sites. The SiFA technology enables simple, and rapid fluorine-18 labeling under mild conditions. There was no need for additional reactants due to this process being driven by simple isotopic exchange. Azeotropically dried fluoride-18 was added to the PNP solution to initiate the radiolabeling process. Initially acetonitrile was used as the reaction solvent due to SiFA labeling protocols already established for peptides and proteins.[38] Protic solvents should be unable to facilitate the isotopic exchange reaction due to the solvation of fluorine-18.[38] However, publications by *Scott, et al*. where fluorine labeling was done in ethanol and *Glaser, et al*., where the SiFA isotopic exchange reaction was performed in water, inspired us to attempt the reaction in ethanol. [152,153] Radiolabeling of PNPs in ethanol would establish green reaction conditions without the need to separate the final product from an environmentally harmful solvent such as acetonitrile. Experiments revealed that isotopic exchange was successful in ethanol with an increase in radiochemical yield (RCY) compared to acetonitrile. In one experiment the increase in fluorine-18 incorporation for PNP1 was from ~40% to ~69%. The increase in RCY was likely due to the increased solubility of PNPs in ethanol versus acetonitrile. However, to facilitate isotopic exchange it was necessary to increase the reaction temperature to 65 °C and reaction time to 30 minutes (as opposed to 25 °C and 20 minutes for the acetonitrile reaction). The ethanolic isotopic exchange reaction was applied to PNP1, and PNP5-PNP14. PNP2 showed poor solubility in ethanol and therefore the reaction was conducted in acetonitrile. PNP3 was insoluble in all solvents excluding water, preventing successful isotopic exchange. Results from radiolabeling experiments are listed in Table 6.

Table 6: Fluorine-18 incorporation based on NAP™-10 elution profiles and RCYs of labeled ^{18}F-PNPs after size-exclusion chromatography

PNP	Size in water (nm)	Size in MeOH (nm)	Fluorine-18 Incorporation (%)	Radiochemical yield (%)
PNP1	33.65	414.2	65 ± 22	28 ± 10
PNP2*	19.61	30.02	54 ± 17	20 ± 5
PNP3	4.89	6.99	0	0
PNP5	32.81	59.39	68 ± 14	26 ± 7
PNP6	45.12	843	53 ± 11	19 ± 2
PNP7	71.9	1512	72 ± 11	25 ± 8
PNP8	40.12	38.11	64 ± 12	23 ± 5
PNP9	91.54	1216	59 ± 10	20 ± 7
PNP10	93.56	965.5	68 ± 10	19 ± 10
PNP11	105.5	967.3	59 ± 20	25 ± 12
PNP12	48.44	26.43	63 ± 8	32 ± 3
PNP13	62.92	27.97	66 ± 17	34 ± 12
PNP14	131.6	32.11	77 ± 20	47 ± 9

Sample size for all experiments is n = 3, except for PNP2 where sample size is n=2. Fluorine-18 incorporation and Radiochemical yields were determined using activity measurements from NAP™-10 size exclusion elution fractions.

Monitoring reaction progress and confirming the successful labeling of PNPs required a simple and reliable reaction monitoring technique. Typically silica thin layer chromatography (TLC) plates are used to give adequate and quantitative information about RCYs. Unfortunately, silica TLC was not suitable due to both PNPs and fluorine-18 remaining on the baseline regardless of the eluent used. Therefore, paper TLC strips with a water eluent were used, which allowed successful separation of the PNP retention factor (R_f=0) from the fluorine-18 RF (R_f=1) (Figure 19). Spotting the radiolabeled PNP fluorine-18 labeling reaction solution onto paper chromatography strips resulted in the radiolabeled PNPs remaining on the baseline whereas fluorine-18 would follow the solvent front.
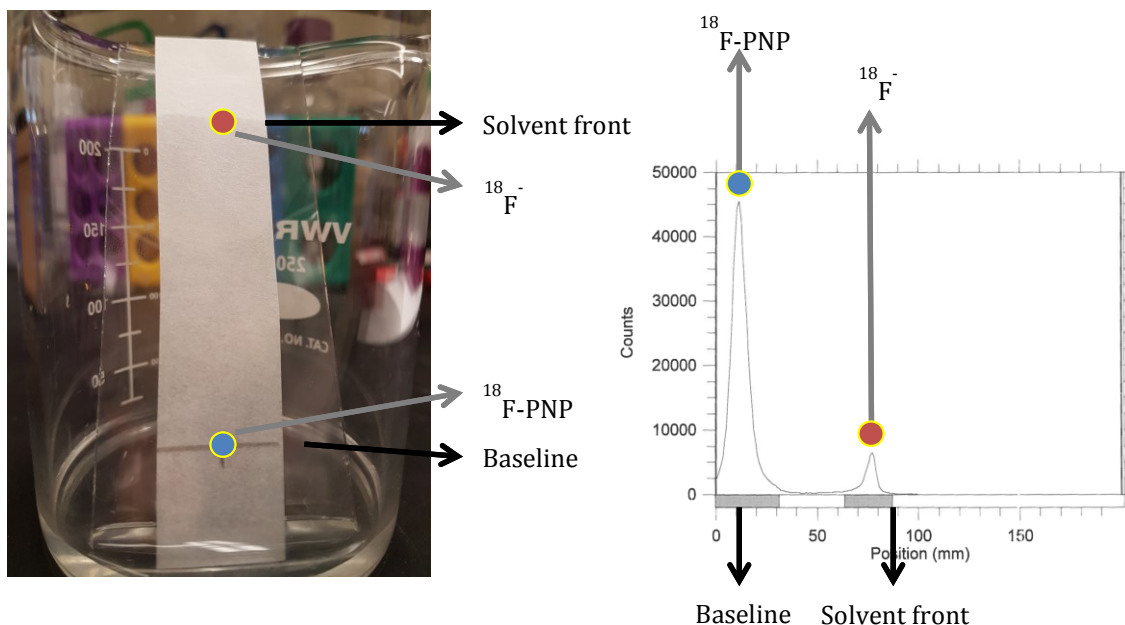
Figure 19: Paper chromatography results for the PNP radiolabeling reaction. For all PNP fluorine-18 labeling reactions TLC strips were spotted with 2 μL of reaction solution and eluted in water containing development chamber. Upon completion, strips were dried completely and analyzed with a radio-TLC scanner (Eckert & Ziegler Bioscan). Baseline (blue dot) contains radiolabeled PNP whereas solvent front (red dot) contains fluorine-18 .

2.6. Fluorine-18 labeled-PNP Purification

Removal of several constituents from the PNP reaction solution was required before *in vivo* studies could be performed. During the fluorine-18 drying process Kryptofix 2.2.2® was added, increasing the nucleophilicity of fluorine-18. Unfortunately, Kryptofix 2.2.2® is toxic and lethal to mice in quantities as low as 1 mg (for a 25 g mouse). [154] Additionally, free fluoride-18 ions injected into mice are absorbed by bones and therefore increase background noise in the PET image. Before radiolabeled PNPs could be injected, it was necessary to develop a reliable purification method to remove both Kryptofix 2.2.2® and fluorine-18 ions. Size exclusion chromatography was deemed the most sensible option due to the significant size difference between PNPs and both Kryptofix 2.2.2®, and fluorine-18. Two size exclusion materials were highly appealing to us: Zeba™ spin columns and NAP™-10 size exclusion columns.

2.6.1. Fluorine-18 Purification Using Zeba™ Spin Desalting Columns

Zeba™ spin desalting columns offer a rapid and effective method of retaining small molecules (<1000 Da) and eluting large macromolecules (>7000Da). This method was appealing due to minimal purification time, resulting in less product decay and less radiation exposure. Furthermore, the product was eluted in a volume suitable for mouse injection (~130 µL). Unfortunately, this method proved to be inconsistent as fluorine-18 often contaminated the final product.

2.6.2. Fluorine-18 Purification Using NAP™-10 Size Exclusion Columns

NAP™-10 size exclusion columns offer a similar property to the ZEBA™ spin columns, as both utilize size exclusion gels for separation. The longer elution pathway present in the NAP™-10 columns led to a more controlled separation. Consistent purification results made it the preferred route for PNP purification. NAP™-10 columns were initially used to determine elution profiles of fluorine-18 and Kryptofix 2.2.2® then compared to the elution profiles of each radiolabeled PNP. Table 8 describes the elution profile of Kryptofix 2.2.2®. Table 9 outlines the elution details of PNP1, PNP2, PNP5-PNP14 and the fluorine-18 elution profile is outlined in table 10. Kryptofix 2.2.2® was determined to elute after 1.5 mL. However Kryptofix 2.2.2® was eluted in quantities below the lethal dosage for mice until the 2.0 mL mark.

Fluorine-18 was found to elute after 2.1 mL (Figure 20). Fluroine-18 labeled PNP elution profiles were very similar for all PNPs. All PNPs eluted from the NAP™-10 column between 1.1 ± 0.1 mL and 1.9 ± 0.2 mL with peak activity concentration at 1.4 ± 0.1 mL. These results indicate that pure radiolabeled PNPs could be obtained by collecting fractions from 1.0 to 2.0 mL. However, due to the bulk of radiolabeled PNP eluting between 1.3 mL and 1.6 mL it was determined that this would be the preferred fraction collection range. While a minimal amount of Kryptofix 2.2.2® is col-eluted within this range, it was determined that concentrations are below toxic quantities until after 2.0 mL (Figure 21) and therefore the fractions containing the highest amount of PNP radioactivity was proven safe for mouse injection. During the purification process it became apparent that $41\% \pm 16\%$ (average of all PNP purification experiments, n=35) of radiolabeled PNPs became

trapped on the NAP™-10 column via an unknown mechanism. This number was determined by measuring the activity remaining on the NAP™-10 columns and comparing it with the activity of pure ^{18}F-PNP fractions. All activity remaining within the NAP™-10 column can be attributed to radiolabeled PNPs. This was confirmed through fluorine-18 elution experiments where no activity remained on the column after elution. It is possible that certain PNPs are trapped within the column due to the formation of aggregates; however, this issue was not investigated further. In addition to its purification uses, NAP™-10 columns provided a quantitative method of monitoring the efficiency of the PNP labeling reaction and the RCY. Examining the elution profile of ^{18}F-PNPs and measuring radioactivity in all fractions as well as the column itself allowed for a full quantification of the radiolabeling reaction.
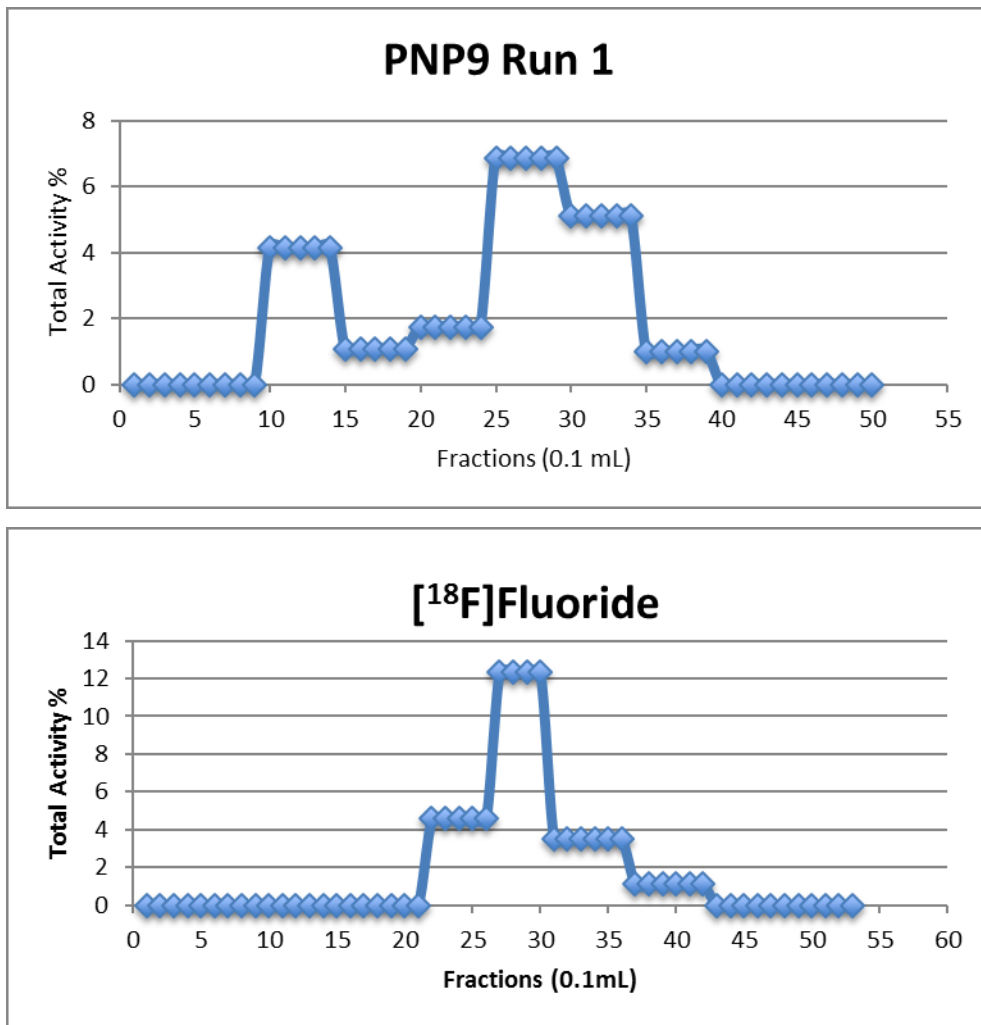
Figure 20: NAP™-10 elution profiles of PNP9 (top) and fluorine-18 solution (bottom) . Y-axis depicts total radioactivity of 0.1 mL elution fractions expressed as a percentage of total radioactivity eluted. X-axis contains fractions collected from column expressed as 0.1 mL volumes. Top graph reveals activity elutes at ~1mL-1.5 mL and 2.5 mL – 3.5 mL. Due to the nature of size exclusion chromatography we should expect PNP to elute before fluorine-18. Bottom graph confirms this as it depicts activity eluting in a single range from 2.2 mL-3.5 mL.
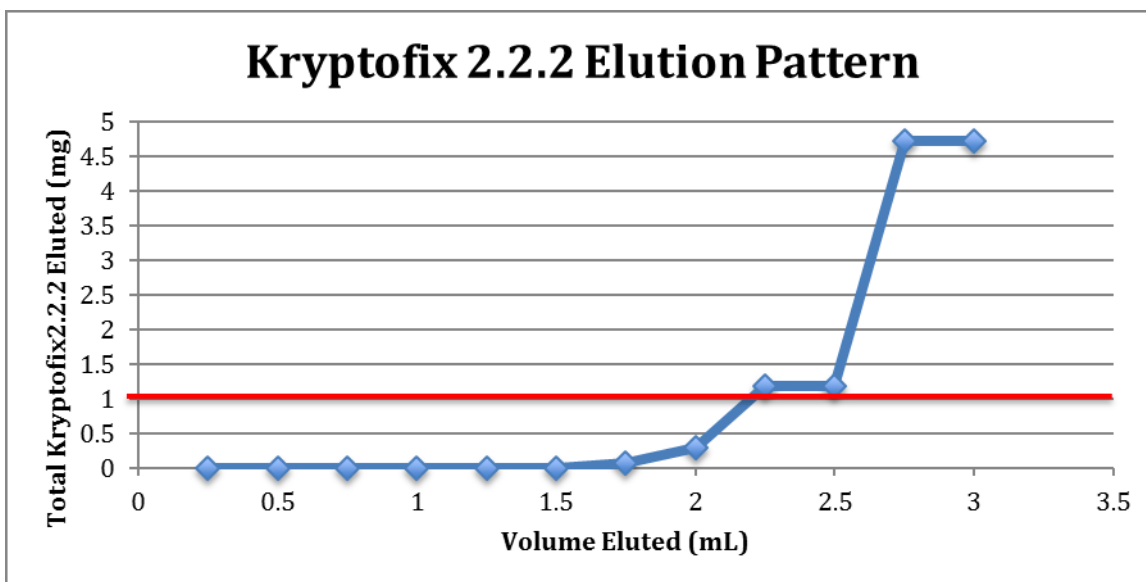
Figure 21: Kryptofix2.2.2 elution pattern from NAP™-10 size exclusion columns. Red line denotes toxic limit of Kryptofix 2.2.2 (1 mg) for a 25 g mouse.

Table 7: NAP™-10 elution profiles for PNPs

Sample	Average Elution Start (mL)	Average Elution Finish (mL)	Volume of Highest Activity Concentration (mL)	Sample Size
PNP1	1.0	1.9	1.5	5
PNP2	1.2	2.2	1.5	2
PNP5	1.1	2.0	1.6	4
PNP6	1.0	2.1	1.5	4
PNP7	1.1	2.3	1.6	4
PNP8	0.9	1.8	1.4	3
PNP9	1.0	1.7	1.3	3
PNP10	1.1	1.7	1.4	4
PNP11	1.1	1.9	1.5	3
PNP12	0.8	1.8	1.3	3
PNP13	1.1	1.9	1.3	3
PNP14	0.9	1.8	1.4	3

2.7. Transmission Electron Microscopy (TEM)

With successful radiolabeling and purification protocols established an experiment was designed to confirm that the fractions collected from the NAP™-10 columns contained radiolabeled PNPs. Transmission Electron Microscopy (TEM) was utilized to visualize the presence of PNPs in fractions collected from NAP™-10 size exclusion chromatography.

TEM images were obtained of pure SiFA tagged PNP1 before radiolabeling (Figure 22, left). PNP1 was then radiolabeled and eluted through the column. NAP™-10 fractions containing volumes from 1 to 2 mL were then analyzed with TEM (Figure 22, right). Images revealed that PNP1 is clearly visible in the fractions collected from the NAP™-10 size exclusion columns. This experiment confirmed that the radioactive product collected over the 1-2 mL range from the NAP™-10 columns contain the PNPs.
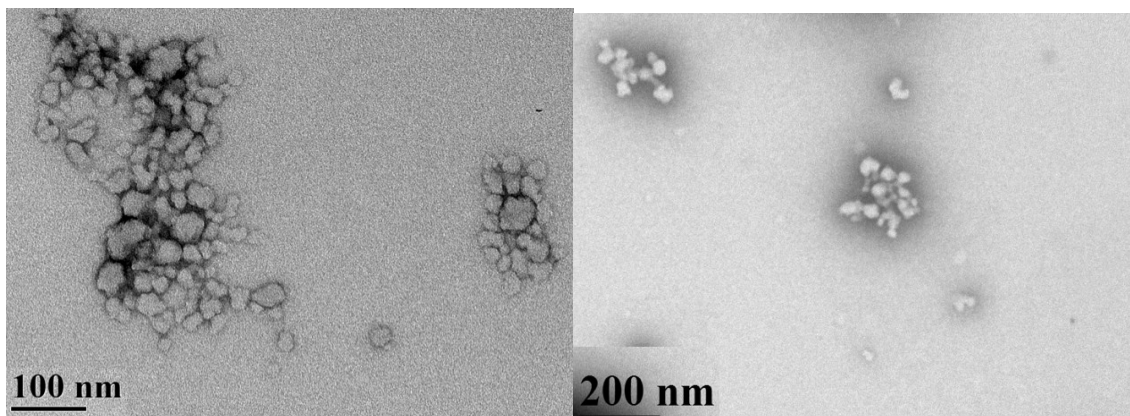
Figure 22: TEM images of PNP1 before and after purification by NAP™-10 size excision chromatography. Left: TEM image of pure PNP1 at 110K X magnification. Right: TEM image of fractions eluted at 1-2 mL from NAP™-10 size exclusion chromatography at 110K X magnification.

2.8. Confirming Covalent Binding of Fluorine-18 to the SiFA Building Block of the PNPs

We wanted to confirm that fluorine-18 was covalently bonded to the SiFA group present on the PNPs. There was a possibility that the fluorine-18 was simply adsorbed on the surface of the PNPs or encapsulated within, simulating covalent fluorine-18 radiolabeling. If this were true the *in vivo* stability of the radiolabeled PNPs would be compromised, as well as the whole labeling concept. Fluorine-18 non-covalently bonded to the PNP would most probably be unstable under physiological conditions and compromise the integrity of the PET study by continuously leaking fluorine-18. A PNP without the SiFA functional group was synthesized to prove this hypothesis. This PNP, PNP20, was produced via thermal micromolusion and expressed a final hydrodynamic diameter of 43 ± 5 nm. Labeling conditions identical to PNP5-PNP14, agitated at 65°C for 30 minutes in ethanol solvent, were performed and the reaction was monitored via radioactive paper TLC and NAP™-10 filtration. Paper TLC revealed 100% of radioactivity

residing at the solvent front, indicating the absence of radiolabeled PNPs. Additionally, the NAP™-10 elution profile of the reaction solution resembled that of the fluorine-18 elution profile (Table 10). Taken together these results reassured us that the fluorine-18 had been covalently bound to the PNP through isotopic exchange with the SiFA technology.

Table 8: NAP™-10 elution profile for PNP20 and fluorine-18

Sample	Activity Elution Start (mL)	Activity Elution end (mL)	Sample size
PNP20	2.6	4.9	3
fluorine-18	2.2	4.2	1

2.9. *In Vivo* Studies

Successful radiolabeling of PNP1, PNP2, PNP5-PNP14 established a reliable labeling protocol and allowed for their *in vivo* analysis using a murine EMT-6 breast cancer tumor model. PNP2, PNP5, PNP6, and PNP7 (20, 33, 45, and 72 nm respectively) were selected as suitable nanoparticles due to their size ranging from 20 nm to 72 nm and RCYs sufficient for *in vivo* studies. This selection exhibited a size range large enough to avoid kidney filtration and should be able to avoid significant opsonization, hypothetically leading to longer blood circulation half-life and therefore better tumor accumulation.[109] Furthermore, PNP2, PNP5, PNP6, and PNP7 were labeled in good radiochemical yields between 28% and 41% (Table 6) suitable for pre-clinical animal studies. A Syngenic EMT-6 breast cancer mammary carcinoma model was chosen for this study due to its established reliability as a tumor model. EMT-6 cells (1 x 10^6 cells in 100 μL PBS) were injected into female BALB/c mice (Charles-River, Saint-Constant, QC, Canada) and allowed to grow to a size of ~300-500 mm^3. Several NPs have already been analyzed in the EMT-6 tumor model with results showing NP accumulation at tumor sites, making this model useful for comparison as well.[103] PNP2, PNP5, PNP6, and PNP7 were then radiolabeled with fluorine-18 using the [^{18}F]SiFA approach as described before, purified and injected into the EMT-6 tumor-bearing mice for PET imaging. A dynamic PET scan was performed over 1-hour p.i. for each PNP. Static PET scans were then conducted for each PNP at 1- and 4-hours p.i.. Examining the clearance profiles, specifically through the liver and kidney provided valuable data on the PNPs accumulation and clearance properties (Figure 23).

The data obtained from these studies provided insight on the PNPs ability to exploit their passive tumor uptake via the EPR effect. Calculating semi-quantitative tumor uptake values and comparing these numbers to non-targeting muscle tissue provides a measure of suitable tumor-specific uptake for the ^{18}F-PNPs as tumor targeting radiotracers.
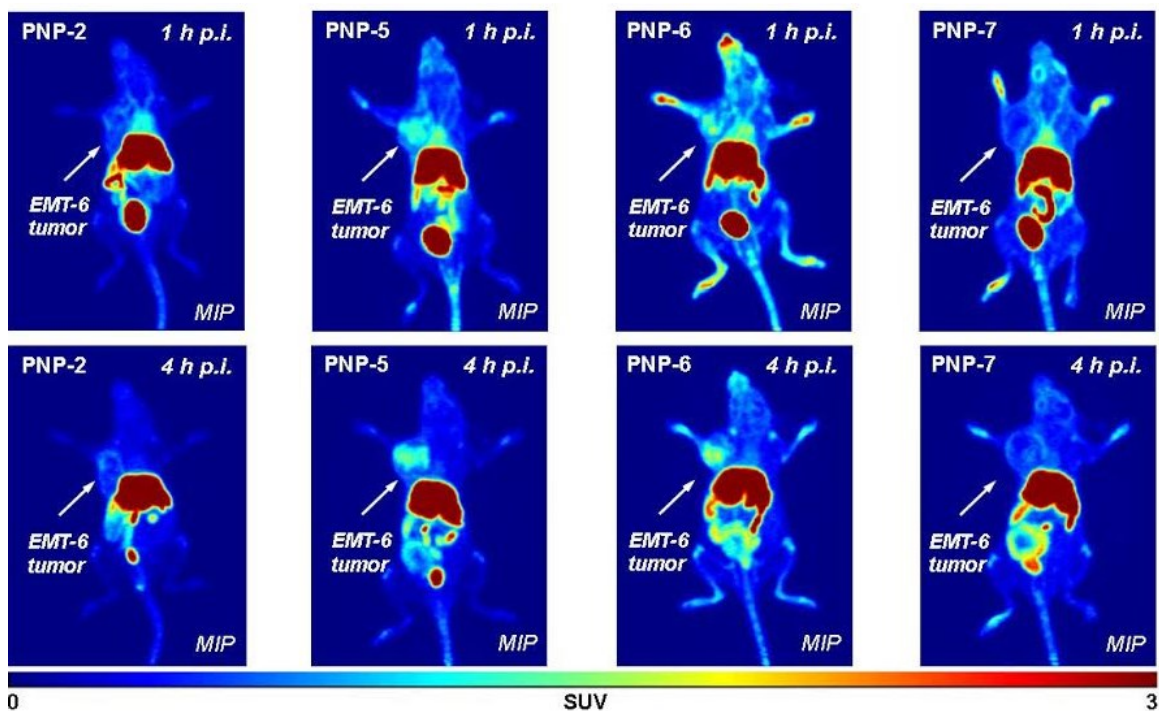
Figure 23: Representative PET images (MIP, maximum intensity projection) of fluorine-18 labeled PNP2, PNP5, PNP6, and PNP7 in EMT-6 tumor bearing mice at 1(top)- and 4(bottom)- hours p.i.. Location of EMT-6 tumors are marked with an arrow.

Dynamic PET imaging over 1-hour p.i. revealed high and rapid liver uptake for all four ^{18}F-PNPs despite their hydrophilic nature (Figure 24). Mean Standardized Uptake Values (SUV_{mean}) in the liver remained fairly constant over the 1 hour time course. Static PET images at 1-hour p.i. showed all ^{18}F-PNPs displayed high tumor radioactivity levels with SUV_{mean} ranging from 3.8 to 4.9 SUV_{mean}. Static 4-hour p.i. scans revealed that liver uptake remained relatively unchanged for all ^{18}F-PNP (an SUV_{mean} of 3.9 - 5.2) confirming that no clearance from the liver was observed during the 4 hour time frame. Interestingly, at 4-hours p.i. PNP7, the largest PNP, showed the highest liver accumulation (SUV_{mean} of 5.20 ± 0.20), whereas PNP2, the smallest PNP, showed the lowest liver accumulation

(SUV$_{mean}$ of 3.86 ± 0.15). This result is in line with other studies that suggest larger Nps are more vulnerable to opsonization.[109]

Figure 24: Top: Semi-quantitative SUV$_{mean}$ values for liver radioactivity levels of all four analyzed 18F-PNPs after 1-hour p.i (left) and 4-hours p.i, (right) Data are shown as mean ± SEM from n-experiments. Bottom: Time-activity curves (TACs) from dynamic scans for the liver radioactivity levels over the course of 1-gour p.i. Data are shown as SUV from n=1 or n=2 experiment.

In contrast clearance through the kidneys was observed at much lower levels and relatively fast. After 5 min a continuous decrease in radioactivity was observed (Figure 25, bottom left). This was the case for all ^{18}F-PNPs. At 1-hour p.i. static scans revealed SUV$_{mean}$ for all four ^{18}F-PNPs to be between 1.3 and 1.9, with ^{18}F-PNP6 showing the highest kidney activity levels (SUV$_{mean}$ = 1.9 ± 0.11). Static scans after 4-hours p.i. revealed all ^{18}F-PNP SUV$_{mean}$ dropped to 0.6 to 0.85. This kidney clearance pattern could be attributed to a fast final renal clearance into the bladder, which showed very high levels for all ^{18}F-PNP at 1-hour p.i. (SUV$_{mean}$ = 30 – 40 for PNP bladder at 1-hour p.i.).

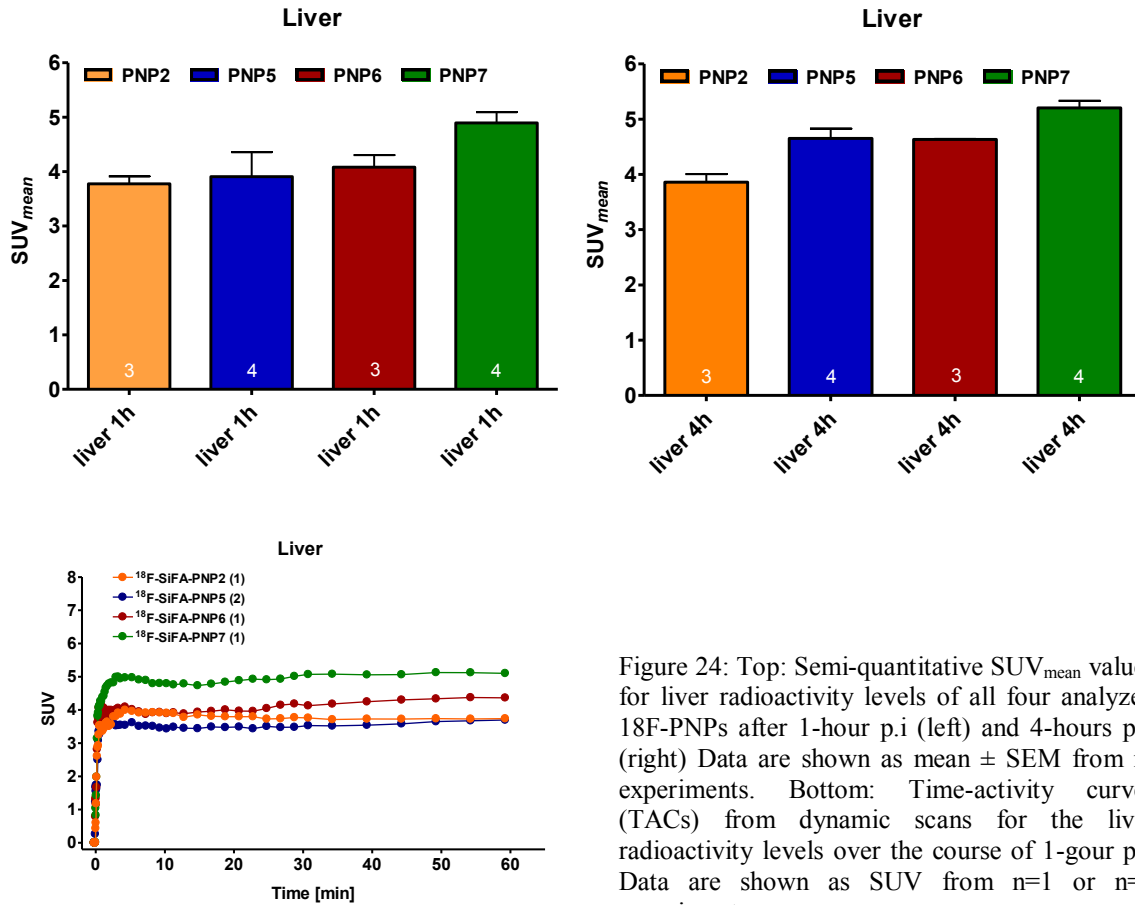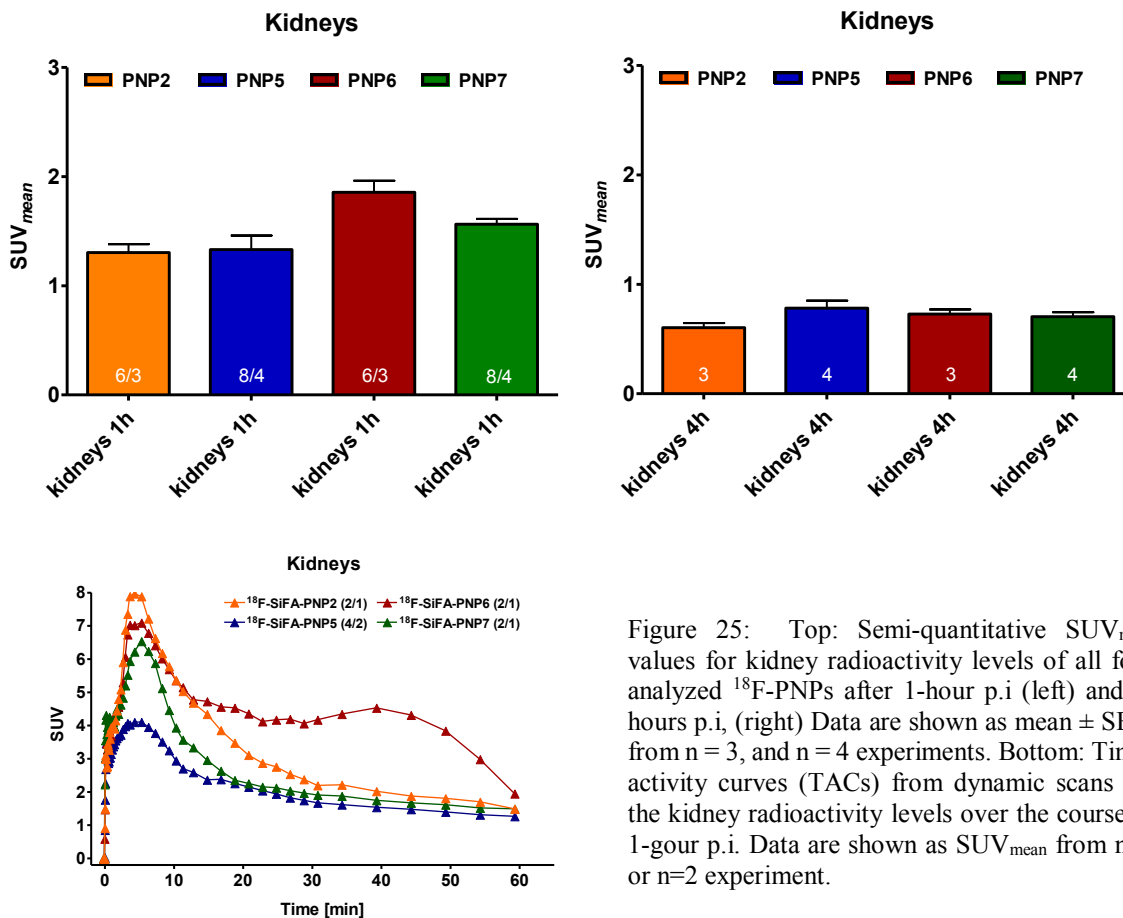Figure 25: Top: Semi-quantitative SUV_{mean} values for kidney radioactivity levels of all four analyzed ^{18}F-PNPs after 1-hour p.i (left) and 4-hours p.i, (right) Data are shown as mean ± SEM from n = 3, and n = 4 experiments. Bottom: Time-activity curves (TACs) from dynamic scans for the kidney radioactivity levels over the course of 1-gour p.i. Data are shown as SUV_{mean} from n=1 or n=2 experiment.

Comparable clearance profiles have been observed in other NP studies of similar sizes. *Hirn, et al*. examined monodisperse, negatively charged gold NPs of 1.4, 5, 18, 80, and 200 nm in rats at 24-hours p.i.. They noted through fluorescent imaging that as the size of the NPs increased, liver concentration (hepatobilary clearance) also increased. Furthermore, the liver exhibited highest concentration of all organs for all NP sizes.[115] A second size related study examined fluorescently tagged 30, 50, 69 and 110 nm polymeric micelles in tumor bearing mice. The 110 nm NPs had slightly higher liver accumulation than its smaller NP counterparts.[155] Further agreeing with our results, a paper published by *Fang, et al*. observed small (<100 nm), medium (100-200 nm) and large (200 nm) NPs incubated in protein serum. After 2-hours there was a clear relationship between size and opsonization, indicating that larger NPs are more prone to opsonization and thus subsequent hepatic clearance from the bloodstream.[107,156] As a general rule, first pass renal

clearance occurs for particles with a size of < 5 nm. While all particles with sizes above are characterized by increased hepatobilary clearance and decreased renal clearance pattern.[106]

All four fluorine-18 labeled PNPs demonstrated EMT-6 tumor accumulation at 1- and 4-hours p.i. (Figure 26). Highest uptake levels were detected using ^{18}F-PNP5, the 32.8 nm NP, resulting in an SUV_{mean} at 1-hour p.i. of 0.77 ± 0.11 and SUV_{mean} at 4-hours p.i. of 0.97 ± 0.11 (n=4, p<0.05). ^{18}F-PNP2, the smallest NP in this study (19.6 nm), displayed the lowest tumor uptake value of $SUV_{mean} = 0.47 \pm 0.02$ (n=3) at 1-hour p.i. which did not increase further. Conversely, as the size of the PNPs increased over 30 nm, EMT-6 tumor uptake decreased again: $SUV_{mean,60min}$ 0.72 ± 0.21 (n=3) for ^{18}F-PNP6 and 0.60 ± 0.02 (n=4) for ^{18}F-PNP7. These latter two did also not increase further in their tumor uptake levels over the 4-hour time course. In conclusion, tumor uptake levels only increased for ^{18}F-PNP5 significantly over the 4-hours p.i.. All three other investigated ^{18}F-PNPs did not show any significant change in their tumor uptake levels over time. The SUV_{mean} of 0.97 ± 0.11 for EMT-6 tumor uptake level with ^{18}F-PNP5 at 4-hours p.i. corresponds to 4.42 ± 0.59 %ID/g. This value is in a similar order of magnitude as two other studies using radiolabeled NP with sizes of ~25-30 nm which detected 3-5 %ID/g of tumor uptake at 4-hours p.i. in two different tumor models.[157,158,106]
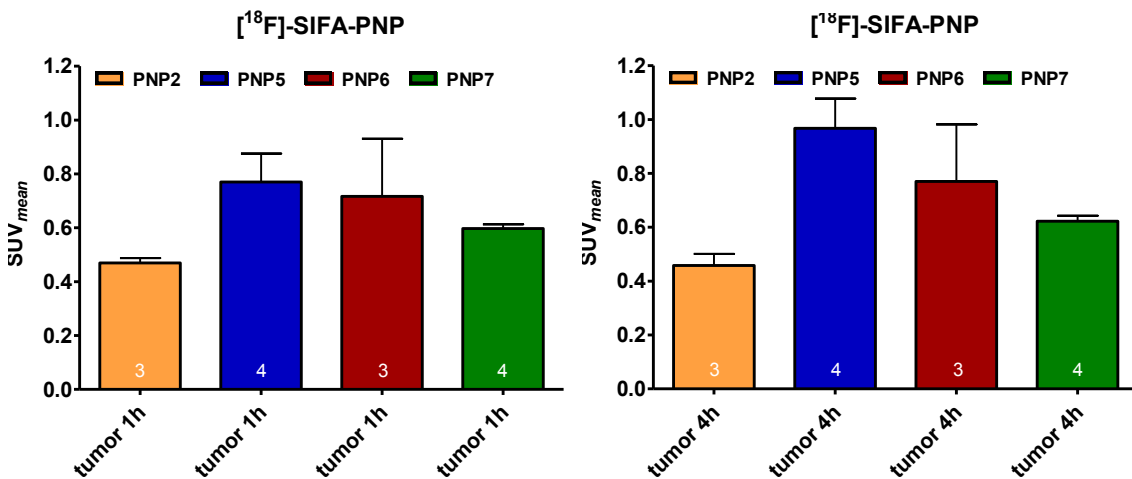

Figure 26: Semi-quantitative SUV_{mean} values for EMT-6 tumor accumulation for all four investigated ^{18}F-PNPs after 1-hour p.i. (left) and 4-hours p.i. (right). Data shown as mean ± SEM from n experiments.

Tumor-to-muscle ratios (T/M) can provide information about the PNPs as diagnostic tumor imaging agents. T/M is a factor that defines the quality of the resulting PET image based on the tumor radioactivity uptake versus background radioactivity levels such as unspecific muscle uptake. ^{18}F-PNP2 displayed the lowest muscle tissue uptake with $SUV_{mean, 4h}$ of 0.11 ± 0.01(n=3), followed by ^{18}F-PNP5 of 0.23 ± 0.03 (n=4) at 4-hours p.i.. ^{18}F-PNP6 and ^{18}F-PNP7 both showed the highest muscle uptake at 4 hours p.i. with SUV_{mean} of 0.34 ± 0.02 (n=3) and 0.25 ± 0.03 (n=4), respectively. Muscle tissue SUV_{mean} dropped between 1- and 4-hours p.i. for all four analyzed ^{18}F-PNPs. Comparing the T/M of each ^{18}F-PNP at 1-hour p.i. clearly reveals that the ^{18}F-PNP5 and ^{18}F-PNP2 are the most proficient with values of 3.2 and 3.0 respectively (Table 11). These numbers increased further to 4.2 and 4.4 after 4-hours p.i. which is indicative of an increase in image contrast over time. ^{18}F-PNP5 presented an optimal T/M at 4-hours p.i. due to the high tumor uptake with an SUV_{mean} of 0.97 in combination with a low muscle retention with an SUV_{mean} of 0.23. These values indicate that in this tumor model, EMT-6, the 30 nm (^{18}F-PNP5) NP had the most effective size for selectively accumulating in the tumor tissue via EPR targeting which, as stated already above, confirms the general relationship between particle size and passive tumor uptake as analyzed and proposed by *Wittrup et al.*[106]

Table 9: SUV_{mean} values and tumor-to-muscle (T/M) ratios derived from PET imaging experiments for all four investigated ^{18}F-PNPs.

^{18}F-PNP	Size (nm)	Tumor SUVmean (1-hours p.i.)	T/M (1-hours p.i.)	Tumor SUVmean (4-hours p.i.)	T/M (4-hours p.i.)	Sample size
PNP2	19.61 ± 5.91	0.47 ± 0.02	2.99 ± 0.12	0.46 ± 0.04	4.43 ± 0.81	3
PNP5	32.81 ± 3.49	0.77 ± 0.11	3.22 ± 0.47	0.97 ± 0.11	4.21 ± 0.20	4
PNP6	45.12 ± 5.80	0.72 ± 0.21	1.69 ± 0.51	0.77 ± 0.21	2.31 ± 0.71	3
PNP7	71.90 ± 9.28	0.60 ± 0.02	2.14 ± 0.17	0.62 ± 0.02	2.60 ± 0.24	4

Data are given as mean ± standard error from the mean from n experiments

For completeness, results from dynamic scans over 1-hour p.i. for both the tumor and muscle uptake are presented as time-activity curves (TACs) in Figure 27. Tumor TACs

show a similar profile of initial uptake and then steady state radioactivity accumulation in tumor tissue over time for all four 18F-PNPs. Muscle TACs show a continuous washout over time for all four ^{18}F-PNPs. These differences in accumulation and clearance profiles between the tumor and muscle tissue can easily be explained by the EPR effect. The tumors are subject to higher initial levels of PNP penetration due to the enhanced permeability of tumor vasculature, resulting in the accumulation of more PNPs within the tumor over time. Throughout the 1-hour p.i. scan tumor radioactivity slowly increased while muscle radioactivity slowly decreased. The higher tumor radioactivity uptake can be explained by the compromised lymphatic drainage system, typical of most tumors whereas; muscle tissue harbors an intact lymphatic drainage system capable of removing any foreign particles such as the PNPs resulting in washout over time. Analyzing T/M ratios over 1-hour p.i. revealed the trends associated with the EPR effect. T/M increased gradually over one hour for all ^{18}F-PNPs. ^{18}F-PNP5 and ^{18}F-PNP2 both reached a maximum T/M ratio of ~3 after 1-hour p.i. confirming their more optimal particle size for increasing tumor uptake over time versus the larger NPs studied. Graphing T/M values over time clearly demonstrate the presence of the EPR effect and depict how this phenomenon can be used to successfully target tumors but only with a specific particle size. A relationship *Wittrup et al.*[106] has suggested and other studies using radiolabeled nanoparticles have also confirmed.[159]

Muscle uptake

EMT-6 tumor uptake

Tumor-Muscle-Ratios
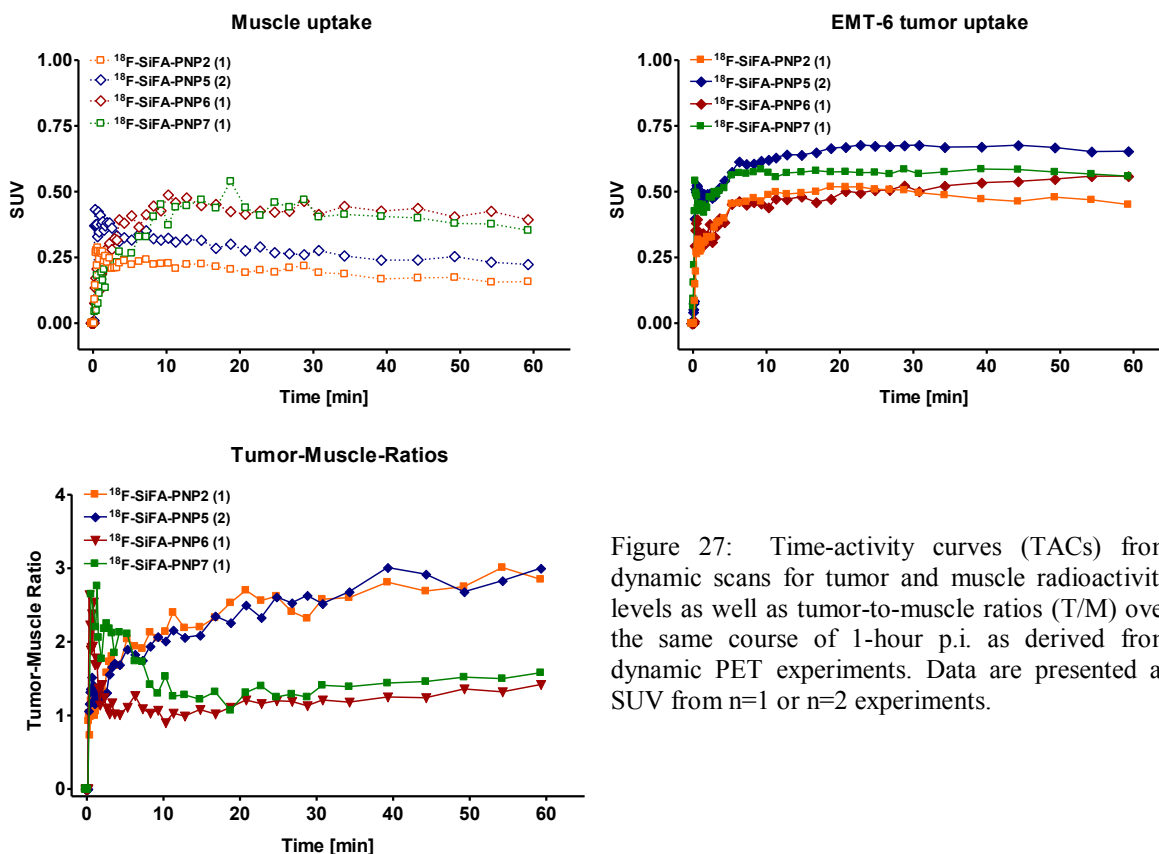
Figure 27: Time-activity curves (TACs) from dynamic scans for tumor and muscle radioactivity levels as well as tumor-to-muscle ratios (T/M) over the same course of 1-hour p.i. as derived from dynamic PET experiments. Data are presented as SUV from n=1 or n=2 experiments.

Conducting *in vivo* experiments using functional PET imaging with ^{18}F-PNPs of various sizes helped elucidate valuable information on how NP size contributes to tumor uptake and therefore detection. Examining radioactivity levels of radiolabeled nanoparticles within the tumor on both an absolute basis and relative to muscle tissue allowed the determination of which particle size was the most proficient for passive tumor targeting which can be used for diagnostic purposes using non-invasive imaging technology. Our results determined that PNP5, the 33 nm nanoparticle, was the most effective at tumor targeting (highest SUV_{mean} and high T/M at both 1- and 4- hour p.i.), the only ^{18}F-PNP which showed an increasing tumor accumulation over time. The further the PNP diameter deviated from this size the less tumor accumulation was observed. This was particularly true for the smallest NP, PNP2 (20 nm), which displayed the lowest tumor SUV_{mean} of all four PNPs at both 1- and 4-hours p.i.(static scans). When further comparing to the literature correlation between nanoparticle size and tumor uptake was also found to be consistent with several other studies of a similar nature using fluorescence to track NP

biodistribution. *Cabral, et al.* showed that, out of polymeric micelle NPs sizes 30, 54, 69 and 110 nm injected into tumor bearing mice, the 30 nm NPs was the most proficient when targeting pancreatic adenocarcinoma BxPC3 tumor mice, followed by the 54 nm nanoparticle.[155] *Sykes, et al.* injected Gold NPs of 46, 64, 104 and 166 nm diameters into MDA-MB-435 breast tumor-bearing mice and observed that there was a negative correlation between gold NP size and tumor uptake at 4-hours p.i. with 46nm being the most effective tumor targeting agent.[105] Another study using 20, 50 and 200nm copper-64 labeled silica NPs were analyzed in MCF-7 human breast cancer mice via PET and it was determined that at 5- and 20-hours p.i. the 50nm NP was the most concentrated in the tumor, followed by the 20nm nanoparticle.[160] These publications also revealed that as nanoparticle size deviates away from the 30 nm size, tumor concentration decreases.

Several other experiments have been done with NPs of similar sizes to the PNPs examined in this thesis. *Andresen, et al.* observed that polymeric NPs of 31-36 nm had a T/M ratio of 2 to 3 at 1-hour and 5-6 at 22-hours p.i..[133] A 29.4 ± 1.2 nm NP radiolabeled with copper-64 resulted in a T/M of 2.0 at 1-hour p.i., 2.5 at 4-hours p.i. and 3.1 at 18-hours p.i..[126] A 25 nm polymeric micelle NP presented a T/M of 11 at 6-hours with very high spleen and liver activity and low kidney activity indicative of low renal and preferred hepatobilary clearance. This study was observed over 120-hours p.i. and found peak tumor activity at 48-hours p.i. (T/M of 15). These three studies clearly indicate that the EPR effect is a prolonged phenomenon. [132] A large iron oxide NP (71.6 ± 3.8 nm) of similar size to PNP7 showed high liver accumulation from 0.5- to 48-hours p.i..[124] Highest tumor uptake occurred at 48-hours p.i..[124] A second study, also involving a large NP, examined 80 nm silica nanoparticles. This NP exhibited very high liver uptake relative to that of the other organs as well. However, this NP displayed a high T/M, which peaked at 4-hours p.i. at 7 over a 48-hour scan. This experiment, by *Chen, et al.*, displayed peak tumor accumulation much earlier than most other NP experiments.[131] A study involving a NP of similar size to PNP5 by *Zhao, et al.* examined gold NPs of 27 ± 3.2 nm. This NP showed an excellent T/M and compared the values to [^{18}F]FDG uptake, the "gold standard" radiotracer for diagnostic PET imaging. [^{18}F]FDG displayed a tumor to muscle ratio of ~4 when injected into tumor bearing mice. The NP showed a value of 4 at 1-hour and 12 at 24-hours p.i.

demonstrating that after 1-hour p.i. NPs have the potential to display superior contrast in tumors.[103] Lastly, a copper-64 labeled polymer based NP of 30-40 nm revealed high radioactivity levels detected in the urinary bladder, similar to ^{18}F-PNP5, with static scans observing a drop in kidney levels from 1- to 4- to 24-hours p.i. indicative of a fast renal clearance, while T/M rose from 1- to 4- after 24-hours p.i..[137] The comparison of the present *in vivo* results from this thesis with the literature leads to the conclusion that the four analyzed fluorine-18 labeled PNPs were successful in passive tumor targeting via the EPR effect. Specifically, ^{18}F-PNP5 displayed a suitable $SUV_{mean, 4h}$ value of 0.97 corresponding to ~4.4 % ID/g, which correlates well with literature reports using similar sized nanoparticles.[159] The T/M ratio of ~4 at 4h p.i. also correlates well with T/M ratios reported form other studies using similar sized NPs (see Table 12). The present results are encouraging and suggest PNP5 should be further evaluated as a passive tumor-targeting agent.

Table 10: Comparison of T/M ratios from different studies analyzing radiolabeled NPs

Nanoparticle	Size (nm)	T/M (1 hr p.i.)	T/M (at x hrs p.i.)	Tumor Model	Reference
Polymeric Micelles	31-36	2-3	5-6 at 22 hours	EMT-6 breast cancer	133
Iron Oxide	29.4 +/- 1.2	2.0	2.5 at 4 hours	U87MG glioma	126
Mesoporous Silica Nanoparticle	80	2.6*	3.1 at 4 hours	4T1 Murine Breast cancer	131
Gold Nanoparticle	27 +/-3.2	4	12 at 24 hours	EMT-6 breast cancer model	103
^{18}F-PNP5	32 nm	3.21	4.22 at 4 hrs p..i.	EMT-6 breast cancer	Present thesis

* at 0.5 hours p.i.

2.10. Conclusion

Twelve distinct PNPs conjugated with SiFA (PNP1, PNP2, PNP5-PNP14) were ^{18}F-radiolabeled through a rapid 1-step efficient process with fluorine-18. For PNP1, PNP5-PNP14 radiolabeling isotopic exchange was performed in ethanol, an environmentally safe solvent with low toxicity. These reactions were monitored via paper radio-TLC and the ^{18}F-PNPs were purified through size exclusion chromatography. To establish good sample sizes all PNPs were radiolabeled and purified in triplicates. PNP2, PNP4, PNP6, and PNP7 (20, 33, 45, 72 nm respectively) were radiolabeled with higher levels of radioactivity (~1 GBq), purified and injected into EMT-6 breast tumor bearing

mice to determine tumor uptake and organ biodistribution PET imaging was conducted over a 4 hour time period. Scans revealed that all ^{18}F-PNPs showed low kidney uptake (< 1 SUV$_{mean}$ at 4 hours p.i.), and high liver uptake (4-5 SUV$_{mean}$ at 4 hours p.i.). All four ^{18}F-PNPs demonstrated tumor accumulation, PNP5, PNP6, and PNP7 showed an increase in tumor accumulation after 1- to 4- hours p.i. where PNP2 tumor accumulation remained constant. The 32 nm PNP (PNP5) showed highest tumor uptake after both 1- and 4-hour post injection. Comparing tumor SUV to muscle SUV revealed that both the PNP2 (20 nm) and PNP5 (32 nm) displayed highest T/M values after 4-hours p.i., increasing over time to 4.43 and 4.22 respectively. These results are encouraging and revealed that ^{18}F-PNPs, specifically in the 30 nm PNP (PNP5), should be further evaluated as a tumor-targeting agent in a variety of different tumor models. Our aspirations for future PNP experiments will furthermore involve incorporating active targeting modalities to the PNPs. Taken together, we have demonstrated the power of pre-clinical PET imaging for the determination of the most efficient PNP size for tumor accumulation in the EMT-6 tumor model. In order to plan for a future therapeutic approach by using PNPs loaded with therapeutic radionuclides, our investigation demonstrated that ^{18}F-PET imaging can help deciding which PNP size will be the most suitable for endo-radiotherapy or any other kind of PNP-based delivery approach of anti-cancer drugs.

3. Methods

3.1. Reserach Contributions: Schirrmacher Research Group (Department of Oncology, University of Alberta); Weberskirch- and Jurkschat Research Groups (University of Dortmund, Department of Chemistry, Germany) and Wuest Research Group (Department of Oncology, University of Alberta).

All PNPs were designed, synthesized, and characterized by the Jurkschat and Weberskirch group from the University of Dortmund (Germany). PET scans, data conversion to images, and PET data analysis were performed by Dr. Melinda Wuest. The author of this thesis, Sheldon Berke, performed all radiolabeling experiments, optimizations, purifications, reaction monitoring experiments, TEM imaging, and helped with PET data analysis.

3.2. PNP Syntheses

PNPs were synthesized via a microemulsion process in which amphiphilic blockcopolymers were used as surfactants that self assemble into micelles (Figure 28). [150] Initially, two phases existed: an organic phase containing (1,6-hexandiol diacrylate) (HDDA) and hepadecane, as well as an aqueous phase containing the polymer subunits and azo-bis-(isobutyronitrtile) (AIBN). The mixture was sonicated for 1 minute at 45 Khz to obtain a homogenous solution where the polymer surfactants formed micelles encapsulating the HDDA. Afterwards, the reaction was heated to 65°C to initiate polymerization. Cross-linking of polymers was initiated via one of two methods, either AIBN (a thermal approach), or 2-propanethiol (a photochemical approach). Six unique polymer subunits were used to synthesize the various NPs in the microemulsion process: P0, P1, P2, P3, P3B, P5 (Figure 29). P0, P1, P2, P3B and P5 are functionalized with the SiFA technology to allow for rapid fluorine-18 labeling. PNP size was further controlled by incorporating varying percentages by weight of HDDA as a crosslinking agent. Through these various synthetic conditions 13 PNPs were produced, each with a distinct hydrodynamic diameter determined by dynamic light scattering (Table 12).

3.2.1. Materials and General Methods

All chemicals were purchased from Sigma–Aldrich (Steinheim, Germany), Acros (Nidderau, Germany) or ABCR (Karlsruhe, Germany), and were used as received unless otherwise stated. (4-(Bromomethyl)phenyl)di-tert-butylfluorosilane (SiFA-Br, synthesized according to *Jurkschat et al.*[161]), 2-methyl-2-oxazoline (MeOx), 2-heptyl-2-oxazoline (HepOx, synthesized according to *Seeliger et al.*[162]), 2-(5-pentyl-[(1,2,3-triazol)-4-yl-methacrylat)]-2-oxazoline (PenOx, synthesized according to ten *Brummelhuis et al.*[163]) and acetonitrile (ACN) for polymer preparation were dried by refluxing over CaH_2 under a dry argon atmosphere and subsequent distillation prior to use. Dry solvents were purified using a purification system from M Braun Glovebox Technology PLC 800. The dialysis membranes were composed of regenerated cellulose from ZelluTrans/Roth V-Series with a MWCO = 1000.

3.2.2. NMR Experiments

The NMR spectra were recorded on a Bruker Avance-300 DP X (300.1 MHz) and 400 DR X (400.1 MHz) at 292 K or the spectra were measured on 500 MHz spectrometer AVANCE-III HDX-500 with 5mm nitrogen cooled Prodigy H(C,N) probe from Bruker BioSpin GmbH or on a 400 MHz NMR spectrometer Nanobay AVANCE-III HD-400 with 5mm BBFOsmart probe from Bruker BioSpin GmbH. The spectra were calibrated using the solvent signals ($CDCl_3$ 7.26 ppm).

3.2.3. Size Exclusion Chromatography

The Size exclusion chromatography (SEC) was performed on a Viscotec GPCmax equipped with an refractive index (RI) detector (tempered to 55 °C) using a Tosoh TSKgel GMHHR-M (1x precolumn + 2x 5.0 μm pores) column set. *N,N*-dimethylformamide was used as eluent (DMF + LiBr, 20 mmol) at a flow rate of 0.7 mL min^{-1} at 60 °C. GPC columns were calibrated with poly(styrene) standards (from Viscotec). Prior to each

measurement, the samples were filtered through a 0.2 μm Teflon filter (VWR) to remove particles.

3.2.4. Dynamic Light Scattering

Dynamic light scattering experiments were performed using a Malvern Zetasizer Nano S (ZEN 1600). A 4 mW He-Ne laser (633 nm wavelength) with a fixed detector angle of 173° was used for these measurements. About 1 mL of dust-free sample was transferred to special light scattering cell. The experiments were carried out in water and methanol at 25 °C and were repeated five times for sufficient sample size.

3.2.5. Polymer Synthesis

Polymer Synthesis. Poly-[SiFA-(2-methyl-2-oxazoline)$_{22}$-OH] **(P0)**: The polymerization and workup procedures were carried out following a general procedure. In a Schlenk tube, 500 μL 2-methyl-2-oxazoline (MOx, 20 eq.), 97.4 mg SiFA-Br (1 eq.) and 5 mL dry acetonitrile were mixed under inert conditions (argon). The reaction mixture was stirred at 110 °C for 4 h. At room temperature, 1 mL of a methanolic sodiumhydroxide (pH 8) solution as a terminating agent was added and the reaction mixture was stirred for 30 minutes at room temperature.[20] The solid residue was filtered off and the solvent was removed at reduced pressure. Then water was added and the crude product was dialyzed for 24 h (MWCO = 1000) and afterwards lyophilized. Further the polymer was purified by reprecipitation in cold diethylether. The precipitated polymer was removed by centrifugation and dried under high pressure. **^{1}H-NMR** (300.13 MHz, CDCl$_3$): δ (ppm) = 1.04 (s, 20H, C(C*H$_3$*)$_{,SiFA}$), 2.06−2.13 (m, 64H, C*H$_{3,MOx}$*), 3.44 (m, 102H, C*H$_2$*-C*H$_{2,backbone}$*), 4.52 (brs, 2H, C*H$_{2,SiFA}$*), 7.19/7.61 (brs, 2H/2H, Phenylring$_{,SiFA}$). **^{29}Si-NMR** (59.63 MHz, CDCl$_3$): δ (ppm) = 11.55, 16.55 (^{2}J(^{29}Si-^{19}F)=298.15 Hz). **^{19}F-NMR** (282.4 MHz, CDCl$_3$): δ (ppm) = -188.12.

Poly[SiFA-(2-methyl-2-oxazoline)$_{24}$-*block*-(2-heptyl-2-oxazoline)$_7$-OH] **(P1)**: In a Schlenk tube, 500 μL 2-methyl-2-oxazoline (MOx, 22 eq.), 88.5 mg SiFA-Br (1 eq.) and 5 mL dry acetonitrile were mixed under inert conditions (argon). The reaction mixture was

stirred at 110 °C for 2 h. Then 361 µL 2-heptyl-2-oxazoline (8 eq.) was added and heated at 120 °C for 4 h. At room temperature, 1 mL of a methanolic sodiumhydroxide (pH 8) solution as a terminating agent was added and the reaction mixture was stirred for 30 minutes at room temperature.[20] The solid residue was filtered off and the solvent was removed at reduced pressure. Then water was added and the crude product was dialyzed (MWCO = 1000) for 24 h and afterwards lyophilized. Further the polymer was purified by reprecipitation in cold diethylether. The precipitated polymer was removed by centrifugation and dried under high pressure. ^{1}**H-NMR** (300.13 MHz, CDCl$_3$): δ (ppm) = 0.81 (s, 21H, CH_3,HOx), 0.99 (s, 18H, C(CH_3),SiFA), 1.22 (s, 54H, 4 × CH_2,HOx), 1.53 (brs, 14H, CH_2,HOx), 2.06−2.13 (m, 81H, CH_3,MOx), 2.30 (m, 10H), 3.40 (m, 124H, CH_2-CH_2,backbone), 4.48 (brs, 2H, CH_2,SiFA), 7.14/7.57 (brs, 2H/2H, Phenylring,SiFA). ^{29}**Si-NMR** (59.63 MHz, CDCl$_3$): δ (ppm) = 11.61, 16.60 (^{2}J(^{29}Si-^{19}F)=298.74 Hz). ^{19}**F-NMR** (282.4 MHz, CDCl$_3$): δ (ppm) = -188.13. SEC: PDI = 1.14, M$_n$ = 4463 g/mol.

Poly[SiFA-(2-methyl-2-oxazoline)$_{31}$-*block*-{(2-heptyl-2-oxazoline)$_4$-*co*-(2-pentynyl-2-oxazoline)$_5$}-OH] **(P2)**: In a Schlenk tube, 1000 µL 2-methyl-2-oxazoline (MOx, 30 eq.), 129.8 mg SiFA-Br (1 eq.) and 5 mL dry acetonitrile were mixed under inert conditions (argon). The reaction mixture was stirred at 110 °C for 2.5 h. Then 265 µL 2-heptyl-2-oxazoline (4 eq.) and 215 µL 2-pentynyl-2-oxazoline (4 eq.) was added simultaneously and heated at 120 °C for 6 h. At room temperature, 1 mL of a methanolic sodiumhydroxide (pH 8) solution as a terminating agent was added and the reaction mixture was stirred for 30 minutes at room temperature.[20] The solid residue was filtered off and the solvent was removed at reduced pressure. Then water was added and the crude product was dialyzed (MWCO = 1000) for 24 h and afterwards lyophilized. Further the polymer was purified by reprecipitation in cold diethylether. The precipitated polymer was removed by centrifugation and dried under high pressure. ^{1}**H-NMR** (500.13 MHz, CDCl$_3$): δ (ppm) = 0.87 (s, 11H, CH_3,HOx), 1.04 (s, 18H, C(CH_3),SiFA), 1.29 (s, 30H, 4 × CH_2,HOx), 1.59 (brs, 8H, CH_2,HOx), 1.83 (brs, 10H, CH_2,AOx),2.06−2.13 (m, 102H, CH_3,MOx, CH_2,AOx), 2.25-2.60 (m, 25H), 3.40 (m, 160H, CH_2-CH_2,backbone), 4.53 (brs, 2H, CH_2,SiFA), 7.17/7.62 (brs, 2H/2H, Phenylring,SiFA). ^{29}**Si-NMR** (59.63 MHz, CDCl$_3$): δ (ppm) = 11.61, 16.60 (^{2}J(^{29}Si-^{19}F)=298.74 Hz). ^{19}**F-NMR** (282.4 MHz, CDCl$_3$): δ (ppm) = -188.13. SEC: PDI = 1.08, M$_n$ = 5503 g/mol.

Poly{(2-methyl-2-oxazoline)$_{31}$-*block*-{(2-heptyl-2-oxazoline)$_4$-*co*-(2-pentynyl-2-oxazoline)$_5$-OH] **(P3)**: In a Schlenk tube, 1000 µL 2-methyl-2-oxazoline (MOx, 30 eq.), 44 µL methyltrilate (1 eq.) and 5 mL dry acetonitrile were mixed under inert conditions (argon). The reaction mixture was stirred at 110 °C for 2 h. Then 265 µL 2-heptyl-2-oxazoline (4 eq.) and 214 µL 2-pentynyl-2-oxazoline (4 eq.) was added simultaneously and heated at 120 °C for 6 h. At room temperature, 1 mL of a methanolic sodiumhydroxide (pH 8) solution as a terminating agent was added and the reaction mixture was stirred for 30 minutes at room temperature.[20] The solid residue was filtered off and the solvent was removed at reduced pressure. Then water was added and the crude product was dialyzed (MWCO = 1000) for 24 h and afterwards lyophilized. Further the polymer was purified by reprecipitation in cold diethylether. The precipitated polymer was removed by centrifugation and dried under high pressure. **^{1}H-NMR** (500.13 MHz, CDCl$_3$): δ (ppm) = 0.86 (s, 15H, C$H_{3,HOx}$), 1.27 (s, 42H, 4 × C$H_{2,HOx}$), 1.58 (brs, 10H, C$H_{2,HOx}$), 1.82 (brs, 12H, C$H_{2,AOx}$), 2.13 (m, 144H, C$H_{3,MOx}$, C$H_{2,AOx}$), 2.26-2.46 (m, 42H), 3.44 (m, 222H, CH_2-C$H_{2,backbone}$). SEC: PDI = 1.09, M_n = 5127 g/mol.

3.2.6. Microemulsion-Polymerization of PNP2, PNP5-PNP7

60 mg of P2 were dissolved in 5 mL millipure water, then 30 µL (50 wt%), 60 µL (100 wt%), 90 µL (150 wt%) or 120 µL (200 wt%) HDDMA, 5 µL AIBN solution (50 mg/mL in 1,4-dioxane) and 5 µL heptadecane were added. After 30 minutes degassing with argon, the mixture was sonicated for 5 minutes. The temperature was then increased to 65 °C overnight. When the reaction was cooled down, the whitish solution was centrifuged for 30 minutes followed by separation of the aqueous layer from the white precipitate (polymerized HDDMA) (two times) at 4400 rpm. The aqueous layer was taken and lyophilized. The received white solid were solved in chloroform and precipitated in cold diethylether. After centrifugation the white solid were dried under high pressure.
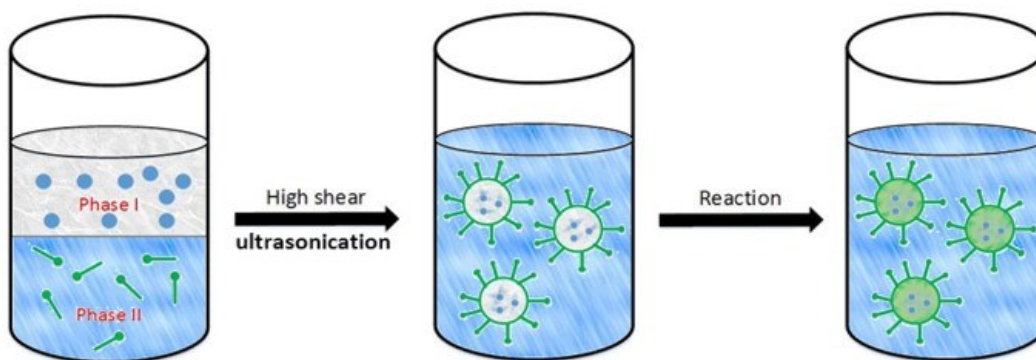
Figure 28: Microemulsion synthesis of PNPs. Amphipilic block copolymers are used as surfactants. Initially two phases exist: organic phase I containing 1,6-hexanediol diacrylate and the hydrophobe hepadecane and an aqueous phase II containing polymer subunits and AIBN. Mixture is then sonicated for one minute at 45 kHz, followed by core-cross linking via radical conditions. Image provided by Weberskirch group.

Figure 29: Polymer subunits used in PNP synthesis. Six distinct subunits were used in the microemulsion process: P0, P1, P2, P3, P3B, and P5.

Table 11: PNP properties

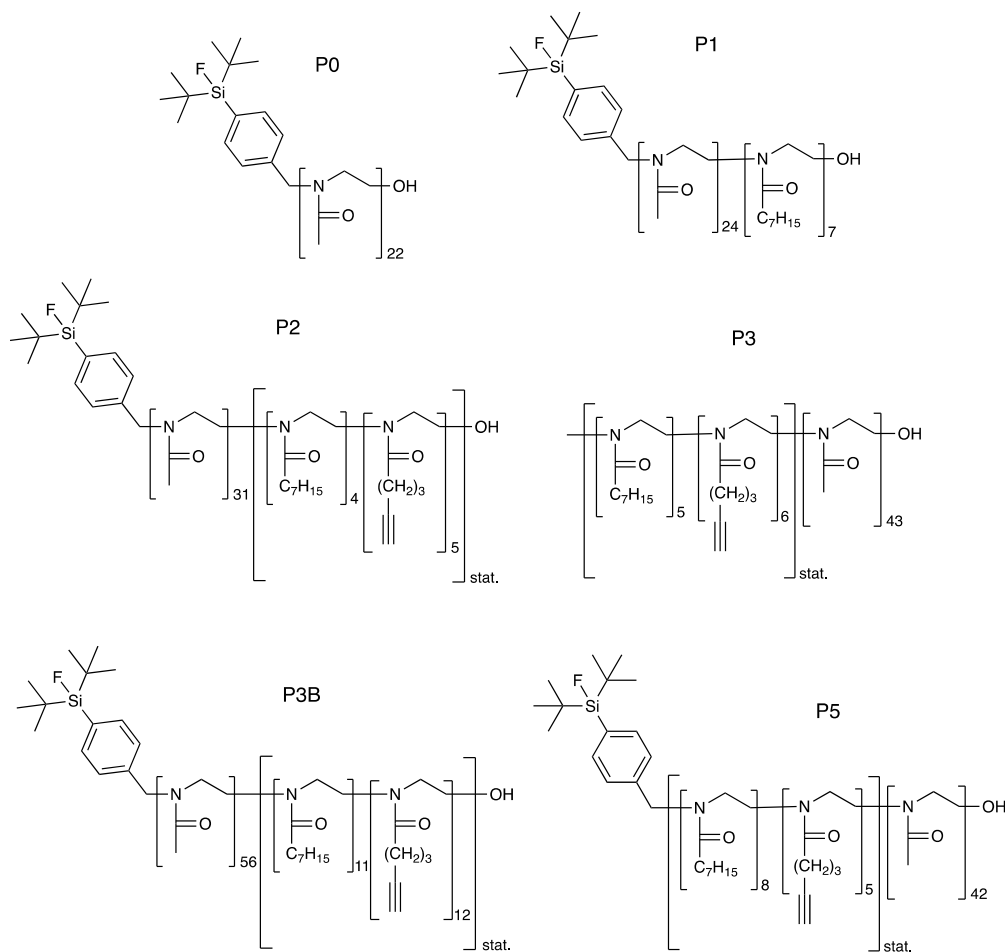| PNP	Subunit	HDDA%	Hydrodynamic diameter (nm)	Type	Initiator
1	P1	50	33.65±2,89	Radical	AIBN
2	P2	50	19.61±5.91	Radical	AIBN
3	P2:P3 (1:4)	50	4.89±0.79	photochemical	2-propanethiol
5	P2	100	32.81±3.49	Radical	AIBN
6	P2	150	45.12±5.80	Radical	AIBN
7	P2	200	71.90±9.28	Radical	AIBN
8	P3B	50	40.12±5.83	Radical	AIBN
9	P3B	100	91.54±29.27	Radical	AIBN
10	P3B	150	93.56±11.33	Radical	AIBN
11	P3B	200	105.5±12.56	Radical	AIBN
12	P5	50	48.44±1.52	Radical	AIBN
13	P5	100	62.92±10.25	Radical	AIBN
14	P5	200	131.6±20.46	radical	AIBN

AIBN: azo-bis-(isobutyronitrtile)

3.3. Solubility Test

Individual PNPs were assessed for solubility by adding 1 mg of PNP to 1 mL of solvent, mixing for 1 minute, allowing solution to stand undisturbed for 1 hour, and then visually assessing precipitate. Solubility was examined in water, acetonitrile, and ethanol. The results of these tests are arranged in Table 5.

3.4. Fluorine-18 Preparation

Fluorine-18 was produced using an ACSI TR19/9 cyclotron through the $^{18}O(p,n)^{18}F$ nuclear reaction with oxygen-18 enriched water (98%). Fluorine-18 activated water [ca. 1 Gbq in 1.5 mL ^{18}O-water] was then passed through a Sep-Pak Light carbonate QMA cartridge (Waters) preconditioned with 15 mL of water. The cartridge was dried by airflow and a Kryptofix 2.2.2® (12 mg, 0.032 mmol)/K_2CO_3 (1.66 mg 0.012 μmol) solution in acetonitrile/water (96 μL/4 μL)) was passed through QMA cartridge to elute trapped fluoride-18 into a 5.0 mL conical glass vial. The solvent was removed at 90°C under reduced pressure, and a stream of nitrogen gas. The residue was azeotropically dried with

1.0 mL of anhydrous acetonitrile twice at 90°C under a stream of nitrogen gas. Final residue was then dissolved in 300 µL of ethanol for PNP4-15 and 300 µL of acetonitrile for PNP2 fluorine-18 labeling reaction.

3.5. PNP Radiolabeling

3.5.1. PNP1, and PNP5-14 Radiolabeling Procedure

PNP1, and PNP5-14 (0.7 mg) were weighed and added to a 5.0 mL dry conical glass vial containing a stir bar. 6 µmol of Oxalic acid (0.1M in anhydrous ethanol) was then added to the fluorine-18 /ethanol solution (300 µL) and entire solution was transferred to the conical vial. The fluorine-18 /PNP solution was heated to 65°C and agitated for 30 minutes. The solution was then cooled to room temperature. Reaction progress was assessed via paper radio-TLC. Reaction solution was spotted on paper chromatography strips in 2.0 µL aliquots and developed in a water elution chamber. Solvent was allowed to travel 8 cm across TLC strip and then removed and dried. Once completely dry, TLC strips were assessed via gamma radioactivity single trace TLC scanner. (fluoride-18 RF: 1.0, ^{18}F-PNP: 0.0). All PNPs were radiolabeled in triplicates. Fluorine-18 incorporation for PNP1, and PNP5-PNP14 ranged from 53 to 77 % (Table 6).

3.5.2. PNP2 Radiolabeling Procedure

PNP2 (0.7 mg) was weighed and added to a dry conical glass vial. 9.6 µmol of Oxalic acid (0.1M in anhydrous acetonitrile) was then added to the fluorine-18 / acetonitrile solution (300 µL) and entire solution was which was mixed and then added to the vial containing PNP2. The solution was agitated for 20 minutes at room temperature. Reaction progress was assessed via paper radio-TLC. Reaction solution was spotted on paper TLC strips in 2.0 µL aliquots and developed in a water elution chamber. Solvent was allowed to travel 8 cm across TLC strip and then removed and dried. Once completely dry, TLC strips were assessed via gamma radioactivity single trace TLC scanner. (fluorine-18 RF: 1.0, ^{18}F-PNP: 0.0). PNP2 was radiolabeled in duplicates. Fluorine-18 incorporation for PNP2 was 54% ± 17% (Table 6).

3.6. Purification of Radiolabeled Polymer Nanoparticles

3.6.1. Zeba™ Spin Desalting Columns

Zeba™ spin columns were preconditioned by loading 130 μL of saline solution (0.9%) onto the column and subjecting the column to centrifugation at 1500 x g for 1 minutes 3 times. 30 – 130 μL of the PNP radiolabeling reaction solution was then loaded onto the column followed by centrifugation at 1500 x g for 2 minutes. Radioactivity of both the supernatant and Zeba™ column were then measured. Paper radio-TLC was utilized to determine purity of supernatant.

3.6.2. NAP™-10 Size Exclusion Columns

NAP™-10 size exclusion chromatography columns were obtained from General Electric Healthcare Life Sciences.

3.6.2.1. ^{18}F-PNP NAP™-10 Elution

NAP™-10 columns were preconditioned with 20 mL of saline solution (0.9%). Entire ^{18}F-PNP reaction solution for all PNP labeling reactions was loaded onto the column and eluted with saline solution. Fractions containing 0.3 mL of eluent were then collected and assessed for radioactivity via a dose calibrator and 2 μL of each fraction was then spotted on paper TLC for purity assessment.

3.6.2.2. Fluroine-18 NAP™-10 Elution

NAP™-10 columns were preconditioned with 20 mL of saline solution (0.9%). Fluorine-18 solution was eluted through NAP™-10 size exclusion columns with saline solution. Fractions of ~0.3 mL were collected and measured for radioactivity.

3.6.2.3. Kryptofix 2.2.2® NAP™-10 Elution

Eight samples of Kryptofix 2.2.2® in PBS buffer were prepared of various concentrations, 0.1M, 0.05M, 0.025M, 0.0125M, 0.0063M, 0.0031M, 0.0016M, and

0.0008M. Each sample was then spotted (2 µL) on a silica TLC plate in and incubated in an iodine chamber for 10 minutes. TLC spots were then used as standards for comparison (Table X). A solution of 10 mg of Kryptofix 2.2.2® in 300 µL of PBS buffer was then eluted through NAP™-10 size exclusion chromatography columns and seven sequential fractions of 0.5, 0.5, 0.5, 0.25, 0.25, 0.5, and 0.5 mL were collected. 2 µL of each fraction was then spotted on silica TLC and incubated in an iodine chamber for 10 minutes. Colorimetric analysis was then used to compare eluted fractions spots with Kryptofix 2.2.2® standards to assess the Kryptofix 2.2.2® concentration in each fraction.

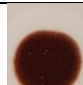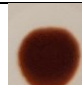Table 12: Iodine chamber results for Kryptofix 2.2.2® standard solutions
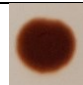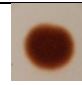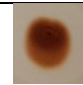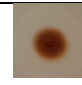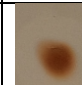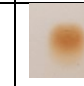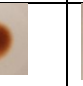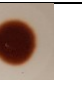
Sample	D0	D1	D2	D3	D4	D5	D6	D7
Amount of Kryptofix 2.2.2® in sample (mg)	11.3	5.65	2.83	1.41	0.71	0.35	0.18	0.09
mmoles of Kryptofix 2.2.2®	0.0300	0.0150	0.0075	0.0038	0.0019	0.0009	0.0005	0.0002
PBS Volume (mL)	0.3	0.3	0.3	0.3	0.3	0.3	0.3	0.3
Kryptofix 2.2.2® Concentration (mol/L)	0.1000	0.050	0.0250	0.013	0.0063	0.0031	0.0016	0.00078
TLC spot								

Table 13: NAP™-10 elution profile for Kryptofix 2.2.2® solution

Fraction	1	2	3	4	5	6	7
Volume (mL) of Fraction	0.5	0.5	0.5	0.25	0.25	0.5	0.5
Total Volume Eluted (mL)	0.5	1	1.5	1.75	2	2.5	3
TLC Spot							
Spot Resemblance to Standard #	None	None	None	D7	D5	D3	D1
Concentration of Kryptofix 2.2.2® in Reference Standard (mol/L)	0	0	0	0.00078	0.0031	0.013	0.050
mmoles of Kryptofix 2.2.2® in Reference Standard	0	0	0	0.00020	0.00078	0.00625	0.02501
Mass of Kryptofix 2.2.2® in Reference Standard (mg)	0	0	0	0.074	0.294	2.354	9.417

3.7. Transmission Electron Microscopy

A 1.0 mg/mL solution of PNP1 in water was incubated on a copper coated carbon grid for 30 seconds at room temperature and then stained with 2% phosphotungstic acid for 15 seconds. A Philips/FEI (Morgagni) Transmission Electron Microscope with CCD camera was used to take the PNP micrographs (accelerating voltage of 110 kV), with the assistance of the University of Alberta Department of Biological Sciences Microscopy Service Unit.

3.8. Confirming Covalent Bonding

The PNP not containing the SiFA unit, PNP 20 (43.39 ± 4.94 nm), was synthesized via micromolusion process with P7 subunits (figure 30). PNP20 (0.7 mg) was added to a 5.0 mL dry conical glass vial containing a stir bar. Oxalic acid (6.0 μmol, 0.54 mg) was then added to the fluorine-18 /ethanol solution and added to vial. The fluorine-18 /PNP solution was then heated to 65 °C and agitated for 30 minutes. Solution was then cooled to room temperature and assessed via radio-TLC. A NAP™-10 column was then preconditioned with saline solution and used to elute PNP20. Fractions of eluent (0.5 mL) were collected and analyzed for activity with an Atomlab™ 500 dosimeter.
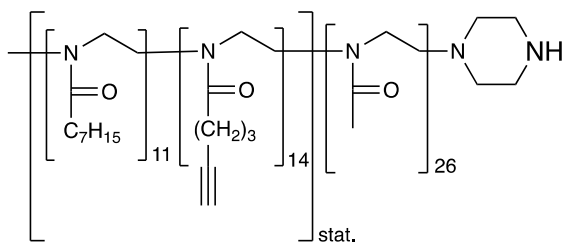
Figure 30: P7 subunit used in microemulsion synthesis for PNP20.

3.9. Radiolabeling of PNPs for *in vivo* Studies

3.9.1. Radiolabeling of PNP2 for *in vivo* Studies

PNP2 (0.6 mg) was dissolved in ethanol and combined with 744 MBq of fluorine-18 solution as prepared in Section 3.4. Reaction was agitated at 20°C for 20 minutes. Subsequently the reaction vial was opened and allowed to evaporate at 80°C for 5 minutes by the aid of a nitrogen sweep flow before being dissolved in a 100 μL 50%/50% saline/ ethanol solution. NAP™-10 columns were preconditioned with 20 mL of saline. Entire

PNP2 fluorine-18 labeling reaction solution was loaded onto the NAP™-10 column and eluted with saline solution. ^{18}F-PNP eluted from 1.0 to 1.9 mL with a radioactivity measurement of 169 MBq (RCY = 23%). An elution fraction was taken in the elution range of 1.3 mL to 1.6 mL to produce a concentrated solution of 69 MBq in 300 µL. This product was then tested for purity via Radio-TLC (Radiochemical purity = >95%) and used for *in vivo* animal studies.

3.9.2. Radiolabeling of PNP5 for *in vivo* Studies

PNP5 (0.3 mg) was dissolved in ethanol and combined with 1960 MBq of fluorine-18 solution (300 µL) as prepared in section 3.4. Reaction was agitated at 65°C for 30 minutes and allowed to cool to room temperature over 5 minutes. NAP™-10 columns were preconditioned with 20 mL of saline solution. Entire PNP5 fluorine-18 labeling reaction solution was loaded onto the NAP™-10 column and eluted with saline solution. ^{18}F-PNP eluted from 1.0 to 1.9 mL with a radioactivity measurement of 181 MBq (RCY = 9.2%). An elution fraction was taken in the elution range of 1.2 mL to 1.6 mL to produce a concentrated solution of 80.4 MBq in 400 µL. This product was then tested for purity via Radio-TLC (Radiochemical purity = >95%) and used for *in vivo* animal studies.

3.9.3. Radiolabeling of PNP6 for *in vivo* Studies

PNP6 (0.6 mg) was dissolved in ethanol and combined with 515 MBq of fluorine-18 solution (300 µL) as prepared in section 3.4. Reaction was agitated at 65°C for 30 minutes and allowed to cool to room temperature over 5 minutes. NAP™-10 columns were preconditioned with 20 mL of saline solution. Entire PNP6 fluorine-18 labeling reaction solution was loaded onto the NAP™-10 column and eluted with saline solution. ^{18}F-PNP eluted from 1.0 to 1.9 mL with a radioactivity measurement of 74 MBq (RCY = 14.3%). An elution fraction was taken in the elution range of 1.3 mL to 1.6 mL to produce a concentrated solution of 32 MBq in 300 µL. This product was then tested for purity via Radio-TLC (Radiochemical purity = >95%) and used for *in vivo* animal studies.

3.9.4. Radiolabeling of PNP7 for *in vivo* Studies

PNP7 (0.3 mg) was dissolved in ethanol and combined with 841 MBq of fluorine-18 solution (300 μL) as prepared in section 3.4. Reaction was agitated at 65°C for 30 minutes and allowed to cool to room temperature over 5 minutes. NAP™-10 columns were preconditioned with 20 mL of saline solution. Entire PNP2 fluorine-18 labeling reaction solution was loaded onto the NAP™-10 column and eluted with saline solution. ^{18}F-PNP eluted from 1.0 to 1.9 mL with a radioactivity measurement of 78 MBq (RCY = 9.3%). An elution fraction was taken in the elution range of 1.2 mL to 1.7 mL to produce a concentrated solution of 55 MBq in 500 μL. This product was then tested for purity via Radio-TLC (Radiochemical purity = >95%) and used for *in vivo* animal studies. RCY for PNP7 was 9.3%.

3.10. *In vivo* Animal Studies

All animal experiments were carried out in accordance with guidelines of the Canadian Council on Animal Care and were approved by the local Animal Ethics Committee of the Cross Cancer Institute, Edmonton. 8-12 weeks old normal female BALB/c mice were obtained from Charles-River (Saint-Constant, Quebec, Canada). Mice were housed in ventilated cages and provided food and water ad libitum. Murine EMT-6 cells (1×10^6 cells in 100 μl PBS) were injected into the upper left shoulder of 6-8 months old female BALB/c mice. Tumors were allowed to grow for 9-11 days reaching a size of ~300-500 mm$^{3.}$ The animals were anesthetized through inhalation of isoflurane in 100% oxygen (gas flow, 1 L/min), and body temperature was maintained at 37°C. Mice were immobilized in the prone position with in the center of the field of view of an INVEON® scanner (Siemens Preclinical Solutions, Knoxville, TN, USA). The amount of radioactivity present in the injection solution in a 0.5 mL syringe was determined with a dose calibrator (Atomlab 300, Biodex Medical Systems, Shirley, NY, USA), which was cross-calibrated with the scanner. ^{18}F-PNP2 was injected into a total of 3 mice. Three PET scans with a duration of 20 min were performed at 1h p.i. (p.i.; one of them as a dynamic scan over the entire 1h) after injection of 5.05-5.98 MBq (50-70 μL saline). An additional static scan was

done after 4 h p.i.. Mice were under anesthesia for the first hour p.i. and wake between the first and the second scan. ^{18}F-PNP5, ^{18}F-PNP6 and ^{18}F-PNP7 were used in a similar manner as described for ^{18}F-PNP2 with always one dynamic scan per radiolabeled NP over 1 h p.i. and an additional static scans at 1 and 4 h p.i.. The following radioactivity amounts were injected: ^{18}F-PNP5 3.44-4.55 MBq (110-180 µL saline; n=4 mice), ^{18}F-PNP6 3.87-4.47 MBq (120-160 µL; n=3 mice) and ^{18}F-PNP7 3.90-5.35 MBq (60-110 µL; n=4 mice), respectively. Dynamic list mode data were sorted into sinograms with 54 time frames (10 x 2 s, 8 x 5 s, 6 x 10 s, 6 x 20 s, 8 x 60 s, 10 x 120 s, 5 x 300 s). The frames as well as all static files were reconstructed using the maximum a posteriori (MAP) reconstruction modes. No correction for partial volume effects was performed. The image files were further processed using the ROVER v2.0.51 software (ABX GmbH, Radeberg, Germany). Masks defining 3D regions of interest (ROI) were set and the ROIs were defined by thresholding. ROIs covered all visible tumor mass of the subcutaneous tumors, and the thresholds were defined by 50% of the maximum radioactivity uptake level for each EMT-6 tumor in each animal. Mean standardized uptake values [SUV_{mean} =(activity/mL tissue)/(injected activity/body weight), mL/kg] were calculated for each ROI. Time-activity curves (TAC) were generated from the dynamic scans. All semi-quantified PET data are presented as mean ± SEM. Time-activity curves were constructed using GraphPad Prism 4.0 (GraphPad Software). Statistical differences were tested by unpaired Student's t-test and were considered significant for $p < 0.05$.

References

1. Allred, D. C.; Clark, G. M.; Tandon, A. K.; Molina, R.; Tormey, D. C.; Osborne, C. K.; Gilchrist, K. W.; Mansour, E. G.; Abeloff, M.; Eudey, L.; et al., HER-2/neu in node-negative breast cancer: prognostic significance of overexpression influenced by the presence of in situ carcinoma. *Journal of clinical oncology : official journal of the American Society of Clinical Oncology* **1992,** *10* (4), 599-605.
2. Bradley, W. G., History of Medical Imaging. *Proc. Amer. Philos. Soc.* **2008,** *152* (3), 349-361.
3. Dancey, A. L.; Mahon, B. S.; Rayatt, S. S., A review of diagnostic imaging in melanoma. *Journal of plastic, reconstructive & aesthetic surgery : JPRAS* **2008,** *61* (11), 1275-83.
4. Hollings, N.; Shaw, P., Diagnostic imaging of lung cancer. *Eur. Resp. J.* **2002,** *19* (4), 722-742.
5. Doi, K., Diagnostic imaging over the last 50 years: research and development in medical imaging science and technology. *Physics in medicine and biology* **2006,** *51* (13), R5-27.
6. Czernin, J.; Weber, W. A.; Herschman, H. R., Molecular imaging in the development of cancer therapeutics. *Annual review of medicine* **2006,** *57*, 99-118.
7. Raichle, M. E.; Mintun, M. A., Brain work and brain imaging. In *Annual Review of Neuroscience*, Annual Reviews: Palo Alto, 2006; Vol. 29, pp 449-476.
8. Hessenbruch, A., A brief history of x-rays. *Endeavour* **2002,** *26* (4), 137-41.
9. Beard, P., Biomedical photoacoustic imaging. *Interface Focus* **2011,** *1* (4), 602-631.
10. Sharma, V.; Luker, G. D.; Piwnica-Worms, D., Molecular imaging of gene expression and protein function in vivo with PET and SPECT. *Journal of magnetic resonance imaging : JMRI* **2002,** *16* (4), 336-51.
11. Scatliff, J. H.; Morris, P. J., From Roentgen to magnetic resonance imaging: the history of medical imaging. *North Carolina medical journal* **2014,** *75* (2), 111-3.
12. Vercher-Conejero, J. L.; Pelegri-Martinez, L.; Lopez-Aznar, D.; Cozar-Santiago, M. D., Positron Emission Tomography in Breast Cancer. *Diagnostics* **2015,** *5* (1), 61-83.
13. Willmann, J. K.; van Bruggen, N.; Dinkelborg, L. M.; Gambhir, S. S., Molecular imaging in drug development. *Nat. Rev. Drug Discov.* **2008,** *7* (7), 591-607.
14. Berger, A., How does it work? Magnetic resonance imaging. *Br. Med. J.* **2002,** *324* (7328), 35-35.
15. Lee, V., Cardiovascular MR Imaging: Physical Principles to Practical Protocols. *Radiology* **2008,** *246* (2), 365-366.
16. Sosnovik, D.; Weissleder, R., Magnetic resonance and fluorescence based molecular imaging technologies. *Progress in drug research. Fortschritte der Arzneimittelforschung. Progres des recherches pharmaceutiques* **2005,** *62*, 83-115.
17. Iagaru, A.; Masamed, R.; Keesara, S.; Conti, P. S., Breast MRI and 18F FDG PET/CT in the management of breast cancer. *Annals of nuclear medicine* **2007,** *21* (1), 33-8.
18. Gambhir, S. S., Molecular imaging of cancer with positron emission tomography. *Nature reviews. Cancer* **2002,** *2* (9), 683-93.

19.   Urch, D. S., Radiochemistry. In *Annual Reports on the Progress of Chemistry, Section A: Inorganic Chemistry, Vol 108*, Royal Soc Chemistry: Cambridge, 2012; Vol. 108, pp 507-523.

20.   Vaquero, J. J.; Kinahan, P., Positron Emission Tomography: Current Challenges and Opportunities for Technological Advances in Clinical and Preclinical Imaging Systems. *Annual review of biomedical engineering* **2015,** *17*, 385-414.

21.   Dogan, B. E.; Turnbull, L. W., Imaging of triple-negative breast cancer. *Annals of Oncology* **2012,** *23* (suppl_6), vi23-vi29.

22.   Del Vecchio, S.; Zanneti, A.; Fonti, R.; Pace, L.; Salvatore, M., Nuclear imaging in cancer theranostics. *Q. J. Nucl. Med. Mol. Imag.* **2007,** *51* (2), 152-163.

23.   Pereira, G. C.; Traughber, M.; Muzic, R. F., Jr., The role of imaging in radiation therapy planning: past, present, and future. *BioMed research international* **2014,** *2014*, 231090.

24.   Higashi, T.; Saga, T.; Nakamoto, Y.; Ishimori, T.; Fujimoto, K.; Doi, R.; Imamura, M.; Konishi, J., Diagnosis of pancreatic cancer using fluorine-18 fluorodeoxyglucose positron emission tomography (FDG PET) --usefulness and limitations in "clinical reality". *Annals of nuclear medicine* **2003,** *17* (4), 261-79.

25.   Suarez, M.; Perez-Castejon, M. J.; Jimenez, A.; Domper, M.; Ruiz, G.; Montz, R.; Carreras, J. L., Early diagnosis of recurrent breast cancer with FDG-PET in patients with progressive elevation of serum tumor markers. *The quarterly journal of nuclear medicine : official publication of the Italian Association of Nuclear Medicine (AIMN) [and] the International Association of Radiopharmacology (IAR)* **2002,** *46* (2), 113-21.

26.   Schwarzenbock, S.; Souvatzoglou, M.; Krause, B. J., Choline PET and PET/CT in Primary Diagnosis and Staging of Prostate Cancer. *Theranostics* **2012,** *2* (3), 318-30.

27.   Handbook of Radiopharmaceuticals: Radiochemistry and Applications. In *Handbook of Radiopharmaceuticals*, Michael J. Welch, C. S. R., Ed. John Wiley & Sons, Ltd: 2005.

28.   Massoud, T. F.; Gambhir, S. S., Molecular imaging in living subjects: seeing fundamental biological processes in a new light. *Genes & development* **2003,** *17* (5), 545-80.

29.   Matthews, P. M.; Rabiner, E. A.; Passchier, J.; Gunn, R. N., Positron emission tomography molecular imaging for drug development. *British Journal of Clinical Pharmacology* **2012,** *73* (2), 175-186.

30.   Bacharach, S. L., Positron Emission Tomography. In *Cardiac CT, PET and MR*, Wiley-Blackwell: 2010; pp 1-29.

31.   van Eijk, C. W., Radiation detector developments in medical applications: inorganic scintillators in positron emission tomography. *Radiation protection dosimetry* **2008,** *129* (1-3), 13-21.

32.   Moriya, T.; Fukumitsu, K.; Yamashita, T.; Watanabe, M., Fabrication of Finely Pitched LYSO Arrays Using Sub-Surface Laser Engraving Technique with Picosecond and Nanosecond Pulse Lasers. *2013 Ieee Nuclear Science Symposium and Medical Imaging Conference (Nss/Mic)* **2013**.

33.   Pierce, L. A.; Hunter, W. C.; Haynor, D. R.; MacDonald, L. R.; Kinahan, P. E.; Miyaoka, R. S., Multiplexing strategies for monolithic crystal PET detector modules. *Physics in medicine and biology* **2014,** *59* (18), 5347-60.

34.   Li, H. D.; Wang, C.; Baghaei, H.; Zhang, Y. X.; Ramirez, R.; Liu, S. T.; An, S. H.; Wong, W. H., A New Statistics-Based Online Baseline Restorer for a High Count-Rate Fully Digital System. *IEEE Trans. Nucl. Sci.* **2010,** *57* (2), 550-555.

35.   Reader, A. J.; Zaidi, H., Advances in PET Image Reconstruction. *PET clinics* **2007,** *2* (2), 173-90.

36.   Bernard-Gauthier, V.; Wangler, C.; Schirrmacher, E.; Kostikov, A.; Jurkschat, K.; Wangler, B.; Schirrmacher, R., (1)(8)F-labeled silicon-based fluoride acceptors: potential opportunities for novel positron emitting radiopharmaceuticals. *BioMed research international* **2014,** *2014*, 454503.

37.   Bernard-Gauthier, V.; Bailey, J. J.; Liu, Z.; Wangler, B.; Wangler, C.; Jurkschat, K.; Perrin, D. M.; Schirrmacher, R., From Unorthodox to Established: The Current Status of (18)F-Trifluoroborate- and (18)F-SiFA-Based Radiopharmaceuticals in PET Nuclear Imaging. *Bioconjugate chemistry* **2016,** *27* (2), 267-79.

38.   Kostikov, A. P.; Chin, J.; Orchowski, K.; Niedermoser, S.; Kovacevic, M. M.; Aliaga, A.; Jurkschat, K.; Wangler, B.; Wangler, C.; Wester, H. J.; Schirrmacher, R., Oxalic acid supported Si-18F-radiofluorination: one-step radiosynthesis of N-succinimidyl 3-(di-tert-butyl[18F]fluorosilyl)benzoate ([18F]SiFB) for protein labeling. *Bioconjugate chemistry* **2012,** *23* (1), 106-14.

39.   Cole, E. L.; Stewart, M. N.; Littich, R.; Hoareau, R.; Scott, P. J., Radiosyntheses using fluorine-18: the art and science of late stage fluorination. *Current topics in medicinal chemistry* **2014,** *14* (7), 875-900.

40.   Price, E. W.; Orvig, C., Matching chelators to radiometals for radiopharmaceuticals. *Chemical Society reviews* **2014,** *43* (1), 260-90.

41.   Sugiura, G.; Kuhn, H.; Sauter, M.; Haberkorn, U.; Mier, W., Radiolabeling strategies for tumor-targeting proteinaceous drugs. *Molecules (Basel, Switzerland)* **2014,** *19* (2), 2135-65.

42.   AGENCY, I. A. E., *Cyclotron Produced Radionuclides: Physical Characteristics and Production Methods*. INTERNATIONAL ATOMIC ENERGY AGENCY: Vienna, 2009.

43.   Ruotsalainen, U.; Raitakari, M.; Nuutila, P.; Oikonen, V.; Sipila, H.; Teras, M.; Knuuti, M. J.; Bloomfield, P. M.; Iida, H., Quantitative blood flow measurement of skeletal muscle using oxygen-15-water and PET. *Journal of nuclear medicine : official publication, Society of Nuclear Medicine* **1997,** *38* (2), 314-9.

44.   Pentlow, K. S.; Graham, M. C.; Lambrecht, R. M.; Daghighian, F.; Bacharach, S. L.; Bendriem, B.; Finn, R. D.; Jordan, K.; Kalaigian, H.; Karp, J. S.; Robeson, W. R.; Larson, S. M., Quantitative imaging of iodine-124 with PET. *Journal of nuclear medicine : official publication, Society of Nuclear Medicine* **1996,** *37* (9), 1557-62.

45.   Pike, V. W., PET radiotracers: crossing the blood-brain barrier and surviving metabolism. *Trends in pharmacological sciences* **2009,** *30* (8), 431-40.

46.   Li, L.; Zhou, X.; Ching, W. K.; Wang, P., Predicting enzyme targets for cancer drugs by profiling human metabolic reactions in NCI-60 cell lines. *BMC bioinformatics* **2010,** *11*, 501.

47.   Park, B. K.; Kitteringham, N. R.; O'Neill, P. M., Metabolism of fluorine-containing drugs. *Annual review of pharmacology and toxicology* **2001,** *41*, 443-70.

48.   Stepan, A. F.; Mascitti, V.; Beaumont, K.; Kalgutkar, A. S., Metabolism-guided drug design. *MedChemComm* **2013,** *4* (4), 631-652.

49. Hanahan, D.; Weinberg, R. A., The hallmarks of cancer. *Cell* **2000,** *100* (1), 57-70.
50. Hanahan, D.; Weinberg, R. A., Hallmarks of Cancer: The Next Generation. *Cell* **2011,** *144* (5), 646-674.
51. Sjoblom, T.; Jones, S.; Wood, L. D.; Parsons, D. W.; Lin, J.; Barber, T. D.; Mandelker, D.; Leary, R. J.; Ptak, J.; Silliman, N.; Szabo, S.; Buckhaults, P.; Farrell, C.; Meeh, P.; Markowitz, S. D.; Willis, J.; Dawson, D.; Willson, J. K. V.; Gazdar, A. F.; Hartigan, J.; Wu, L.; Liu, C. S.; Parmigiani, G.; Park, B. H.; Bachman, K. E.; Papadopoulos, N.; Vogelstein, B.; Kinzler, K. W.; Velculescu, V. E., The consensus coding sequences of human breast and colorectal cancers. *Science (New York, N.Y.)* **2006,** *314* (5797), 268-274.
52. Greenman, C.; Stephens, P.; Smith, R.; Dalgliesh, G. L.; Hunter, C.; Bignell, G.; Davies, H.; Teague, J.; Butler, A.; Edkins, S.; O'Meara, S.; Vastrik, I.; Schmidt, E. E.; Avis, T.; Barthorpe, S.; Bhamra, G.; Buck, G.; Choudhury, B.; Clements, J.; Cole, J.; Dicks, E.; Forbes, S.; Gray, K.; Halliday, K.; Harrison, R.; Hills, K.; Hinton, J.; Jenkinson, A.; Jones, D.; Menzies, A.; Mironenko, T.; Perry, J.; Raine, K.; Richardson, D.; Shepherd, R.; Small, A.; Tofts, C.; Varian, J.; Webb, T.; West, S.; Widaa, S.; Yates, A.; Cahill, D. P.; Louis, D. N.; Goldstraw, P.; Nicholson, A. G.; Brasseur, F.; Looijenga, L.; Weber, B. L.; Chiew, Y. E.; Defazio, A.; Greaves, M. F.; Green, A. R.; Campbell, P.; Birney, E.; Easton, D. F.; Chenevix-Trench, G.; Tan, M. H.; Khoo, S. K.; Teh, B. T.; Yuen, S. T.; Leung, S. Y.; Wooster, R.; Futreal, P. A.; Stratton, M. R., Patterns of somatic mutation in human cancer genomes. *Nature* **2007,** *446* (7132), 153-158.
53. Sledge, G. W.; Miller, K. D., Exploiting the hallmarks of cancer: the future conquest of breast cancer. *Eur. J. Cancer* **2003,** *39* (12), 1668-1675.
54. Norman, S. A.; Localio, A. R.; Zhou, L.; Weber, A. L.; Coates, R. J.; Malone, K. E.; Bernstein, L.; Marchbanks, P. A.; Liff, J. M.; Lee, N. C.; Nadel, M. R., Benefit of screening mammography in reducing the rate of late-stage breast cancer diagnoses (United States). *Cancer causes & control : CCC* **2006,** *17* (7), 921-9.
55. Cancer Reseach UK. http://www.cancerresearchuk.org/about-cancer/cancer-symptoms/why-is-early-diagnosis-important (accessed March 14).
56. David L. Nelson, M. M. C., *lehninher principals of biochemistry* 6th ed.; Macmillian Learning: 2013.
57. Vander Heiden, M. G.; Cantley, L. C.; Thompson, C. B., Understanding the Warburg effect: the metabolic requirements of cell proliferation. *Science (New York, N.Y.)* **2009,** *324* (5930), 1029-33.
58. Buck, A. C.; Schirrmeister, H. H.; Guhlmann, C. A.; Diederichs, C. G.; Shen, C.; Buchmann, I.; Kotzerke, J.; Birk, D.; Mattfeldt, T.; Reske, S. N., Ki-67 immunostaining in pancreatic cancer and chronic active pancreatitis: does in vivo FDG uptake correlate with proliferative activity? *Journal of nuclear medicine : official publication, Society of Nuclear Medicine* **2001,** *42* (5), 721-5.
59. Haberkorn, U.; Ziegler, S. I.; Oberdorfer, F.; Trojan, H.; Haag, D.; Peschke, P.; Berger, M. R.; Altmann, A.; van Kaick, G., FDG uptake, tumor proliferation and expression of glycolysis associated genes in animal tumor models. *Nuclear medicine and biology* **1994,** *21* (6), 827-34.
60. Haberkorn, U.; Markert, A.; Mier, W.; Askoxylakis, V.; Altmann, A., Molecular imaging of tumor metabolism and apoptosis. *Oncogene* **2011,** *30* (40), 4141-51.

61. Warburg, O., On the metabolism of cancer cells. *Naturwissenschaften* **1924,** *12*, 1131-1137.

62. Pacak, J.; Tocik, Z.; Cerny, M., Synthesis of 2-Deoxy-2-Fluoro-D-Glucose. *Journal of the Chemical Society D-Chemical Communications* **1969,** (2), 77-&.

63. Ido, T.; Wan, C. N.; Casella, V.; Fowler, J. S.; Wolf, A. P.; Reivich, M.; Kuhl, D. E., Labeled 2-deoxy-D-glucose analogs. 18F-labeled 2-deoxy-2-fluoro-D-glucose, 2-deoxy-2-fluoro-D-mannose and 14C-2-deoxy-2-fluoro-D-glucose. *Journal of Labelled Compounds and Radiopharmaceuticals* **1978,** *14* (2), 175-183.

64. Reivich, M.; Kuhl, D.; Wolf, A.; Greenberg, J.; Phelps, M.; Ido, T.; Casella, V.; Fowler, J.; Hoffman, E.; Alavi, A.; Som, P.; Sokoloff, L., FLUORODEOXYGLUCOSE-F-18 METHOD FOR THE MEASUREMENT OF LOCAL CEREBRAL GLUCOSE-UTILIZATION IN MAN. *Circulation Research* **1979,** *44* (1), 127-137.

65. Adejolu, M.; Huo, L.; Rohren, E.; Santiago, L.; Yang, W. T., False-positive lesions mimicking breast cancer on FDG PET and PET/CT. *AJR. American journal of roentgenology* **2012,** *198* (3), W304-14.

66. Shields, A. F.; Grierson, J. R.; Dohmen, B. M.; Machulla, H. J.; Stayanoff, J. C.; Lawhorn-Crews, J. M.; Obradovich, J. E.; Muzik, O.; Mangner, T. J., Imaging proliferation in vivo with [F-18]FLT and positron emission tomography. *Nature medicine* **1998,** *4* (11), 1334-6.

67. Christensen, H. N., Role of amino acid transport and countertransport in nutrition and metabolism. *Physiological reviews* **1990,** *70* (1), 43-77.

68. Ganapathy, V.; Thangaraju, M.; Prasad, P. D., Nutrient transporters in cancer: relevance to Warburg hypothesis and beyond. *Pharmacology & therapeutics* **2009,** *121* (1), 29-40.

69. Langen, K. J.; Jarosch, M.; Muhlensiepen, H.; Hamacher, K.; Broer, S.; Jansen, P.; Zilles, K.; Coenen, H. H., Comparison of fluorotyrosines and methionine uptake in F98 rat gliomas. *Nuclear medicine and biology* **2003,** *30* (5), 501-508.

70. Tripathi, M.; Sharma, R.; Varshney, R.; Jaimini, A.; Jain, J.; Souza, M. M.; Bal, J.; Pandey, S.; Kumar, N.; Mishra, A. K.; Mondal, A., Comparison of F-18 FDG and C-11 methionine PET/CT for the evaluation of recurrent primary brain tumors. *Clinical nuclear medicine* **2012,** *37* (2), 158-63.

71. Glunde, K.; Bhujwalla, Z. M.; Ronen, S. M., Choline metabolism in malignant transformation. *Nat. Rev. Cancer* **2011,** *11* (12), 835-848.

72. Gibellini, F.; Smith, T. K., The Kennedy pathway--De novo synthesis of phosphatidylethanolamine and phosphatidylcholine. *IUBMB life* **2010,** *62* (6), 414-28.

73. Hara, T.; Kosaka, N.; Shinoura, N.; Kondo, T., PET imaging of brain tumor with [methyl-11C]choline. *Journal of nuclear medicine : official publication, Society of Nuclear Medicine* **1997,** *38* (6), 842-7.

74. Bollineni, V. R.; Kramer, G. M.; Jansma, E. P.; Liu, Y.; Oyen, W. J., A systematic review on [(18)F]FLT-PET uptake as a measure of treatment response in cancer patients. *European journal of cancer (Oxford, England : 1990)* **2016,** *55*, 81-97.

75. Comar, D.; Cartron, J. C.; Maziere, M.; Marazano, C., LABELING AND METABOLISM OF METHIONINE-METHYL-C-11. *European Journal of Nuclear Medicine* **1976,** *1* (1), 11-14.

76. Vaupel, P.; Mayer, A.; Hockel, M., Tumor hypoxia and malignant progression. *Methods Enzymol.* **2004,** *381*, 335-354.

77. Vaupel, P.; Mayer, A., Hypoxia in cancer: significance and impact on clinical outcome. *Cancer metastasis reviews* **2007,** *26* (2), 225-39.

78. Eschmann, S. M.; Paulsen, F.; Reimold, M.; Dittmann, H.; Welz, S.; Reischl, G.; Machulla, H. J.; Bares, R., Prognostic impact of hypoxia imaging with 18F-misonidazole PET in non-small cell lung cancer and head and neck cancer before radiotherapy. *Journal of nuclear medicine : official publication, Society of Nuclear Medicine* **2005,** *46* (2), 253-60.

79. Piert, M.; Machulla, H. J.; Picchio, M.; Reischl, G.; Ziegler, S.; Kumar, P.; Wester, H. J.; Beck, R.; McEwan, A. J.; Wiebe, L. I.; Schwaiger, M., Hypoxia-specific tumor imaging with 18F-fluoroazomycin arabinoside. *Journal of nuclear medicine : official publication, Society of Nuclear Medicine* **2005,** *46* (1), 106-13.

80. Tafe, L. J., Molecular mechanisms of therapy resistance in solid tumors: chasing "moving" targets. *Virchows Archiv : an international journal of pathology* **2017**.

81. Bernard-Gauthier, V.; Bailey, J. J.; Berke, S.; Schirrmacher, R., Recent Advances in the Development and Application of Radiolabeled Kinase Inhibitors for PET Imaging. *Molecules (Basel, Switzerland)* **2015,** *20* (12), 22000-27.

82. Maeda, H.; Bharate, G. Y.; Daruwalla, J., Polymeric drugs for efficient tumor-targeted drug delivery based on EPR-effect. *European journal of pharmaceutics and biopharmaceutics : official journal of Arbeitsgemeinschaft fur Pharmazeutische Verfahrenstechnik e.V* **2009,** *71* (3), 409-19.

83. Folkman, J.; Merler, E.; Abernathy, C.; Williams, G., Isolation of a tumor factor responsible for angiogenesis. *The Journal of experimental medicine* **1971,** *133* (2), 275-88.

84. Folkman, J., Tumor Angiogenesis Factor. *Cancer research* **1974,** *34* (8), 2109-2113.

85. Hanahan, D.; Folkman, J., Patterns and emerging mechanisms of the angiogenic switch during tumorigenesis. *Cell* **1996,** *86* (3), 353-64.

86. Black, W. C.; Welch, H. G., Advances in diagnostic imaging and overestimations of disease prevalence and the benefits of therapy. *The New England journal of medicine* **1993,** *328* (17), 1237-43.

87. Bergers, G.; Benjamin, L. E., Tumorigenesis and the angiogenic switch. *Nat. Rev. Cancer* **2003,** *3* (6), 401-410.

88. Patan, S.; Munn, L. L.; Jain, R. K., Intussusceptive microvascular growth in a human colon adenocarcinoma xenograft: a novel mechanism of tumor angiogenesis. *Microvascular research* **1996,** *51* (2), 260-72.

89. Klagsbrun, M., Regulators of Angiogenesis. *Annu. Rev. Physiol.* **1991,** *53*, 217-239.

90. Kalluri, R., Basement membranes: Structure, assembly and role in tumour angiogenesis. *Nat. Rev. Cancer* **2003,** *3* (6), 422-433.

91. Carmeliet, P., Mechanisms of angiogenesis and arteriogenesis. *Nature medicine* **2000,** *6* (4), 389-395.

92. Papetti, M.; Herman, I. M., Mechanisms of normal and tumor-derived angiogenesis. *American journal of physiology. Cell physiology* **2002,** *282* (5), C947-70.

93. Gullino, P. M., Angiogenesis and Oncogenesis. *J. Natl. Cancer Inst.* **1978,** *61* (3), 639-643.

94. Senger, D. R.; Perruzzi, C. A.; Feder, J.; Dvorak, H. F., A highly conserved vascular permeability factor secreted by a variety of human and rodent tumor cell lines. *Cancer research* **1986,** *46* (11), 5629-32.

95.   Dvorak, H. F., Tumors: wounds that do not heal. Similarities between tumor stroma generation and wound healing. *The New England journal of medicine* **1986,** *315* (26), 1650-9.

96.   Benjamin, L. E.; Golijanin, D.; Itin, A.; Pode, D.; Keshet, E., Selective ablation of immature blood vessels in established human tumors follows vascular endothelial growth factor withdrawal. *The Journal of clinical investigation* **1999,** *103* (2), 159-65.

97.   Morikawa, S.; Baluk, P.; Kaidoh, T.; Haskell, A.; Jain, R. K.; McDonald, D. M., Abnormalities in pericytes on blood vessels and endothelial sprouts in tumors. *The American journal of pathology* **2002,** *160* (3), 985-1000.

98.   Skinner, S. A.; Tutton, P. J.; O'Brien, P. E., Microvascular architecture of experimental colon tumors in the rat. *Cancer research* **1990,** *50* (8), 2411-7.

99.   Rao, J., Shedding light on tumors using nanoparticles. *ACS nano* **2008,** *2* (10), 1984-6.

100.   Brigger, I.; Dubernet, C.; Couvreur, P., Nanoparticles in cancer therapy and diagnosis. *Advanced drug delivery reviews* **2002,** *54* (5), 631-651.

101.   Latham, A. H.; Freitas, R. S.; Schiffer, P.; Williams, M. E., Capillary magnetic field flow fractionation and analysis of magnetic nanoparticles. *Analytical chemistry* **2005,** *77* (15), 5055-62.

102.   Maeda, H.; Wu, J.; Sawa, T.; Matsumura, Y.; Hori, K., Tumor vascular permeability and the EPR effect in macromolecular therapeutics: a review. *Journal of controlled release : official journal of the Controlled Release Society* **2000,** *65* (1-2), 271-84.

103.   Zhao, Y.; Sultan, D.; Detering, L.; Cho, S.; Sun, G.; Pierce, R.; Wooley, K. L.; Liu, Y., Copper-64-alloyed gold nanoparticles for cancer imaging: improved radiolabel stability and diagnostic accuracy. *Angewandte Chemie (International ed. in English)* **2014,** *53* (1), 156-9.

104.   Maeda, H., SMANCS and polymer-conjugated macromolecular drugs: advantages in cancer chemotherapy. *Advanced drug delivery reviews* **2001,** *46* (1-3), 169-85.

105.   Sykes, E. A.; Chen, J.; Zheng, G.; Chan, W. C., Investigating the impact of nanoparticle size on active and passive tumor targeting efficiency. *ACS nano* **2014,** *8* (6), 5696-706.

106.   Wittrup, K. D.; Thurber, G. M.; Schmidt, M. M.; Rhoden, J. J., Practical theoretic guidance for the design of tumor-targeting agents. *Methods in enzymology* **2012,** *503*, 255-68.

107.   Alexis, F.; Pridgen, E.; Molnar, L. K.; Farokhzad, O. C., Factors affecting the clearance and biodistribution of polymeric nanoparticles. *Molecular pharmaceutics* **2008,** *5* (4), 505-15.

108.   Wang, B.; He, X.; Zhang, Z.; Zhao, Y.; Feng, W., Metabolism of nanomaterials in vivo: blood circulation and organ clearance. *Accounts of chemical research* **2013,** *46* (3), 761-9.

109.   Choi, H. S.; Liu, W.; Misra, P.; Tanaka, E.; Zimmer, J. P.; Itty Ipe, B.; Bawendi, M. G.; Frangioni, J. V., Renal clearance of quantum dots. *Nature biotechnology* **2007,** *25* (10), 1165-70.

110.   Jhaveri, A. M.; Torchilin, V. P., Multifunctional polymeric micelles for delivery of drugs and siRNA. *Frontiers in pharmacology* **2014,** *5*, 77.

111.   Longmire, M.; Choyke, P. L.; Kobayashi, H., Clearance properties of nano-sized particles and molecules as imaging agents: considerations and caveats. *Nanomedicine (London, England)* **2008,** *3* (5), 703-17.

112.   Elsabahy, M.; Wooley, K. L., Design of polymeric nanoparticles for biomedical delivery applications. *Chemical Society reviews* **2012,** *41* (7), 2545-61.

113.   Yu, M.; Zheng, J., Clearance Pathways and Tumor Targeting of Imaging Nanoparticles. *ACS nano* **2015,** *9* (7), 6655-74.

114.   Moghimi, S. M.; Hunter, A. C.; Murray, J. C., Long-circulating and target-specific nanoparticles: theory to practice. *Pharmacological reviews* **2001,** *53* (2), 283-318.

115.   Hirn, S.; Semmler-Behnke, M.; Schleh, C.; Wenk, A.; Lipka, J.; Schaffler, M.; Takenaka, S.; Moller, W.; Schmid, G.; Simon, U.; Kreyling, W. G., Particle size-dependent and surface charge-dependent biodistribution of gold nanoparticles after intravenous administration. *European journal of pharmaceutics and biopharmaceutics : official journal of Arbeitsgemeinschaft fur Pharmazeutische Verfahrenstechnik e.V* **2011,** *77* (3), 407-16.

116.   Sun, T.; Zhang, Y. S.; Pang, B.; Hyun, D. C.; Yang, M.; Xia, Y., Engineered nanoparticles for drug delivery in cancer therapy. *Angewandte Chemie (International ed. in English)* **2014,** *53* (46), 12320-64.

117.   Heidel, J. D.; Davis, M. E., Clinical developments in nanotechnology for cancer therapy. *Pharmaceutical research* **2011,** *28* (2), 187-99.

118.   Dams, E. T.; Laverman, P.; Oyen, W. J.; Storm, G.; Scherphof, G. L.; van Der Meer, J. W.; Corstens, F. H.; Boerman, O. C., Accelerated blood clearance and altered biodistribution of repeated injections of sterically stabilized liposomes. *The Journal of pharmacology and experimental therapeutics* **2000,** *292* (3), 1071-9.

119.   Ishida, T.; Ichihara, M.; Wang, X.; Yamamoto, K.; Kimura, J.; Majima, E.; Kiwada, H., Injection of PEGylated liposomes in rats elicits PEG-specific IgM, which is responsible for rapid elimination of a second dose of PEGylated liposomes. *Journal of controlled release : official journal of the Controlled Release Society* **2006,** *112* (1), 15-25.

120.   Turkevich, J.; Stevenson, P. C.; Hillier, J., A Study of the Nucleation and Growth Processes in the Synthesis of Colloidal Gold. *Discussions of the Faraday Society* **1951,** (11), 55-&.

121.   Zhu, J.; Chin, J.; Wangler, C.; Wangler, B.; Lennox, R. B.; Schirrmacher, R., Rapid (18)F-labeling and loading of PEGylated gold nanoparticles for in vivo applications. *Bioconjugate chemistry* **2014,** *25* (6), 1143-50.

122.   Ng, Q. K.; Olariu, C. I.; Yaffee, M.; Taelman, V. F.; Marincek, N.; Krause, T.; Meier, L.; Walter, M. A., Indium-111 labeled gold nanoparticles for in-vivo molecular targeting. *Biomaterials* **2014,** *35* (25), 7050-7.

123.   Tian, M.; Lu, W.; Zhang, R.; Xiong, C.; Ensor, J.; Nazario, J.; Jackson, J.; Shaw, C.; Dixon, K. A.; Miller, J.; Wright, K.; Li, C.; Gupta, S., Tumor uptake of hollow gold nanospheres after intravenous and intra-arterial injection: PET/CT study in a rabbit VX2 liver cancer model. *Molecular imaging and biology : MIB : the official publication of the Academy of Molecular Imaging* **2013,** *15* (5), 614-24.

124.   Xu, C.; Shi, S.; Feng, L.; Chen, F.; Graves, S. A.; Ehlerding, E. B.; Goel, S.; Sun, H.; England, C. G.; Nickles, R. J.; Liu, Z.; Wang, T.; Cai, W., Long circulating reduced graphene oxide-iron oxide nanoparticles for efficient tumor targeting and multimodality imaging. *Nanoscale* **2016,** *8* (25), 12683-92.

125.   Sharma, R.; Xu, Y.; Kim, S. W.; Schueller, M. J.; Alexoff, D.; Smith, S. D.; Wang, W.; Schlyer, D., Carbon-11 radiolabeling of iron-oxide nanoparticles for dual-modality PET/MR imaging. *Nanoscale* **2013,** *5* (16), 7476-83.
126.   Xie, J.; Chen, K.; Huang, J.; Lee, S.; Wang, J.; Gao, J.; Li, X.; Chen, X., PET/NIRF/MRI triple functional iron oxide nanoparticles. *Biomaterials* **2010,** *31* (11), 3016-22.
127.   Kim, S. M.; Chae, M. K.; Yim, M. S.; Jeong, I. H.; Cho, J.; Lee, C.; Ryu, E. K., Hybrid PET/MR imaging of tumors using an oleanolic acid-conjugated nanoparticle. *Biomaterials* **2013,** *34* (33), 8114-21.
128.   Benezra, M.; Penate-Medina, O.; Zanzonico, P. B.; Schaer, D.; Ow, H.; Burns, A.; DeStanchina, E.; Longo, V.; Herz, E.; Iyer, S.; Wolchok, J.; Larson, S. M.; Wiesner, U.; Bradbury, M. S., Multimodal silica nanoparticles are effective cancer-targeted probes in a model of human melanoma. *The Journal of clinical investigation* **2011,** *121* (7), 2768-80.
129.   Dasog, M.; Kehrle, J.; Rieger, B.; Veinot, J. G., Silicon Nanocrystals and Silicon-Polymer Hybrids: Synthesis, Surface Engineering, and Applications. *Angewandte Chemie (International ed. in English)* **2016,** *55* (7), 2322-39.
130.   Trewyn, B. G.; Slowing, II; Giri, S.; Chen, H. T.; Lin, V. S., Synthesis and functionalization of a mesoporous silica nanoparticle based on the sol-gel process and applications in controlled release. *Accounts of chemical research* **2007,** *40* (9), 846-53.
131.   Chen, F.; Nayak, T. R.; Goel, S.; Valdovinos, H. F.; Hong, H.; Theuer, C. P.; Barnhart, T. E.; Cai, W., In vivo tumor vasculature targeted PET/NIRF imaging with TRC105(Fab)-conjugated, dual-labeled mesoporous silica nanoparticles. *Molecular pharmaceutics* **2014,** *11* (11), 4007-14.
132.   Starmans, L. W.; Hummelink, M. A.; Rossin, R.; Kneepkens, E. C.; Lamerichs, R.; Donato, K.; Nicolay, K.; Grull, H., 89 Zr- and Fe-Labeled Polymeric Micelles for Dual Modality PET and T1 -Weighted MR Imaging. *Advanced healthcare materials* **2015**.
133.   Jensen, A. I.; Binderup, T.; Kumar, E. P.; Kjaer, A.; Rasmussen, P. H.; Andresen, T. L., Positron emission tomography based analysis of long-circulating cross-linked triblock polymeric micelles in a U87MG mouse xenograft model and comparison of DOTA and CB-TE2A as chelators of copper-64. *Biomacromolecules* **2014,** *15* (5), 1625-33.
134.   Perez-Medina, C.; Abdel-Atti, D.; Tang, J.; Zhao, Y. M.; Fayad, Z. A.; Lewis, J. S.; Mulder, W. J. M.; Reiner, T., Nanoreporter PET predicts the efficacy of anti-cancer nanotherapy. *Nat. Commun.* **2016,** *7*.
135.   Hansen, A. E.; Petersen, A. L.; Henriksen, J. R.; Boerresen, B.; Rasmussen, P.; Elema, D. R.; af Rosenschold, P. M.; Kristensen, A. T.; Kjaer, A.; Andresen, T. L., Positron Emission Tomography Based Elucidation of the Enhanced Permeability and Retention Effect in Dogs with Cancer Using Copper-64 Liposomes. *ACS nano* **2015,** *9* (7), 6985-95.
136.   Harrington, K. J.; Mohammadtaghi, S.; Uster, P. S.; Glass, D.; Peters, A. M.; Vile, R. G.; Stewart, J. S., Effective targeting of solid tumors in patients with locally advanced cancers by radiolabeled pegylated liposomes. *Clinical cancer research : an official journal of the American Association for Cancer Research* **2001,** *7* (2), 243-54.
137.   Schluep, T.; Hwang, J.; Hildebrandt, I. J.; Czernin, J.; Choi, C. H.; Alabi, C. A.; Mack, B. C.; Davis, M. E., Pharmacokinetics and tumor dynamics of the nanoparticle IT-101 from PET imaging and tumor histological measurements. *Proceedings of the National Academy of Sciences of the United States of America* **2009,** *106* (27), 11394-9.

138.	Phillips, E.; Penate-Medina, O.; Zanzonico, P. B.; Carvajal, R. D.; Mohan, P.; Ye, Y.; Humm, J.; Gonen, M.; Kalaigian, H.; Schoder, H.; Strauss, H. W.; Larson, S. M.; Wiesner, U.; Bradbury, M. S., Clinical translation of an ultrasmall inorganic optical-PET imaging nanoparticle probe. *Science translational medicine* **2014,** *6* (260), 260ra149.

139.	Di Mauro, P. P.; Gomez-Vallejo, V.; Baz Maldonado, Z.; Llop Roig, J.; Borros, S., Novel 18F labeling strategy for polyester-based NPs for in vivo PET-CT imaging. *Bioconjugate chemistry* **2015,** *26* (3), 582-92.

140.	Guerrero, S.; Herance, J. R.; Rojas, S.; Mena, J. F.; Gispert, J. D.; Acosta, G. A.; Albericio, F.; Kogan, M. J., Synthesis and in vivo evaluation of the biodistribution of a 18F-labeled conjugate gold-nanoparticle-peptide with potential biomedical application. *Bioconjugate chemistry* **2012,** *23* (3), 399-408.

141.	Yamamoto, F.; Yamahara, R.; Makino, A.; Kurihara, K.; Tsukada, H.; Hara, E.; Hara, I.; Kizaka-Kondoh, S.; Ohkubo, Y.; Ozeki, E.; Kimura, S., Radiosynthesis and initial evaluation of (18)F labeled nanocarrier composed of poly(L-lactic acid)-block-poly(sarcosine) amphiphilic polydepsipeptide. *Nuclear medicine and biology* **2013,** *40* (3), 387-94.

142.	Sirianni, R. W.; Zheng, M. Q.; Patel, T. R.; Shafbauer, T.; Zhou, J.; Saltzman, W. M.; Carson, R. E.; Huang, Y., Radiolabeling of poly(lactic-co-glycolic acid) (PLGA) nanoparticles with biotinylated F-18 prosthetic groups and imaging of their delivery to the brain with positron emission tomography. *Bioconjugate chemistry* **2014,** *25* (12), 2157-65.

143.	Rojas, S.; Gispert, J. D.; Martin, R.; Abad, S.; Menchon, C.; Pareto, D.; Victor, V. M.; Alvaro, M.; Garcia, H.; Herance, J. R., Biodistribution of amino-functionalized diamond nanoparticles. In vivo studies based on 18F radionuclide emission. *ACS nano* **2011,** *5* (7), 5552-9.

144.	Herth, M. M.; Barz, M.; Moderegger, D.; Allmeroth, M.; Jahn, M.; Thews, O.; Zentel, R.; Rosch, F., Radioactive labeling of defined HPMA-based polymeric structures using [18F]FETos for in vivo imaging by positron emission tomography. *Biomacromolecules* **2009,** *10* (7), 1697-703.

145.	Sun, Y.; Yu, M.; Liang, S.; Zhang, Y.; Li, C.; Mou, T.; Yang, W.; Zhang, X.; Li, B.; Huang, C.; Li, F., Fluorine-18 labeled rare-earth nanoparticles for positron emission tomography (PET) imaging of sentinel lymph node. *Biomaterials* **2011,** *32* (11), 2999-3007.

146.	Sun, Z.; Cheng, K.; Wu, F.; Liu, H.; Ma, X.; Su, X.; Liu, Y.; Xia, L.; Cheng, Z., Robust surface coating for a fast, facile fluorine-18 labeling of iron oxide nanoparticles for PET/MR dual-modality imaging. *Nanoscale* **2016,** *8* (47), 19644-19653.

147.	Devaraj, N. K.; Keliher, E. J.; Thurber, G. M.; Nahrendorf, M.; Weissleder, R., 18F labeled nanoparticles for in vivo PET-CT imaging. *Bioconjugate chemistry* **2009,** *20* (2), 397-401.

148.	Vaidyanathan, G.; Zalutsky, M. R., Synthesis of N-succinimidyl 4-[18F]fluorobenzoate, an agent for labeling proteins and peptides with 18F. *Nature protocols* **2006,** *1* (4), 1655-61.

149.	Schirrmacher, R.; Bradtmoller, G.; Schirrmacher, E.; Thews, O.; Tillmanns, J.; Siessmeier, T.; Buchholz, H. G.; Bartenstein, P.; Waengler, B.; Niemeyer, C. M.; Jurkschat, K., F-18-labeling of peptides by means of an organosilicon-based fluoride acceptor. *Angewandte Chemie-International Edition* **2006,** *45* (36), 6047-6050.

150.   Kampmann, A. L.; Luksin, M.; Pretzer, I.; Weberskirch, R., Formation of Well-Defined Polymer Particles in the Sub-100 nm Size Range by Using Amphiphilic Block Copolymer Surfactants and a Microemulsion Approach. *Macromolecular Chemistry and Physics* **2016,** *217* (15), 1704-1711.

151.   Powell, J. A.; Schwieters, R. M.; Bayliff, K. W.; Herman, E. N.; Hotvedt, N. J.; Changstrom, J. R.; Chakrabarti, A.; Sorensen, C. M., Temperature dependent solubility of gold nanoparticle suspension/solutions. *Rsc Advances* **2016,** *6* (74), 70638-70643.

152.   Stewart, M. N.; Hockley, B. G.; Scott, P. J., Green approaches to late-stage fluorination: radiosyntheses of (18)F-labelled radiopharmaceuticals in ethanol and water. *Chemical communications (Cambridge, England)* **2015,** *51* (79), 14805-8.

153.   Glaser, M.; Iveson, P.; Hoppmann, S.; Indrevoll, B.; Wilson, A.; Arukwe, J.; Danikas, A.; Bhalla, R.; Hiscock, D., Three methods for 18F labeling of the HER2-binding affibody molecule Z(HER2:2891) including preclinical assessment. *Journal of nuclear medicine : official publication, Society of Nuclear Medicine* **2013,** *54* (11), 1981-8.

154.   Chaly, T.; Dahl, J. R., Thin layer chromatographic detection of kryptofix 2.2.2 in the routine synthesis of [18F]2-fluoro-2-deoxy-D-glucose. *International journal of radiation applications and instrumentation. Part B, Nuclear medicine and biology* **1989,** *16* (4), 385-7.

155.   Cabral, H.; Matsumoto, Y.; Mizuno, K.; Chen, Q.; Murakami, M.; Kimura, M.; Terada, Y.; Kano, M. R.; Miyazono, K.; Uesaka, M.; Nishiyama, N.; Kataoka, K., Accumulation of sub-100 nm polymeric micelles in poorly permeable tumours depends on size. *Nature Nanotechnology* **2011,** *6* (12), 815-823.

156.   Fang, C.; Shi, B.; Pei, Y. Y.; Hong, M. H.; Wu, J.; Chen, H. Z., In vivo tumor targeting of tumor necrosis factor-alpha-loaded stealth nanoparticles: effect of MePEG molecular weight and particle size. *European journal of pharmaceutical sciences : official journal of the European Federation for Pharmaceutical Sciences* **2006,** *27* (1), 27-36.

157.   Lee, J.; Lee, T. S.; Ryu, J.; Hong, S.; Kang, M.; Im, K.; Kang, J. H.; Lim, S. M.; Park, S.; Song, R., RGD peptide-conjugated multimodal NaGdF4:Yb3+/Er3+ nanophosphors for upconversion luminescence, MR, and PET imaging of tumor angiogenesis. *Journal of nuclear medicine : official publication, Society of Nuclear Medicine* **2013,** *54* (1), 96-103.

158.   Yang, K.; Gong, H.; Shi, X.; Wan, J.; Zhang, Y.; Liu, Z., In vivo biodistribution and toxicology of functionalized nano-graphene oxide in mice after oral and intraperitoneal administration. *Biomaterials* **2013,** *34* (11), 2787-95.

159.   Chakravarty, R.; Goel, S.; Dash, A.; Cai, W., Radiolabeled inorganic nanoparticles for positron emission tomography imaging of cancer: an overview. *The quarterly journal of nuclear medicine and molecular imaging : official publication of the Italian Association of Nuclear Medicine (AIMN) [and] the International Association of Radiopharmacology (IAR), [and] Section of the So* **2017,** *61* (2), 181-204.

160.   Tang, L.; Yang, X. J.; Yin, Q.; Cai, K. M.; Wang, H.; Chaudhury, I.; Yao, C.; Zhou, Q.; Kwon, M.; Hartman, J. A.; Dobrucki, I. T.; Dobrucki, L. W.; Borst, L. B.; Lezmig, S.; Helferich, W. G.; Ferguson, A. L.; Fan, T. M.; Cheng, J. J., Investigating the optimal size of anticancer nanomedicine. *Proceedings of the National Academy of Sciences of the United States of America* **2014,** *111* (43), 15344-15349.

161.   Iovkova, L.; Wangler, B.; Schirrmacher, E.; Schirrmacher, R.; Quandt, G.; Boening, G.; Schurmann, M.; Jurkschat, K., para-Functionalized aryl-di-tert-

butylfluorosilanes as potential labeling synthons for (18)F radiopharmaceuticals. *Chemistry (Weinheim an der Bergstrasse, Germany)* **2009,** *15* (9), 2140-7.

162. Witte, H.; Seeliger, W., - Cyclische Imidsäureester aus Nitrilen und Aminoalkoholen. **1974,** - *1974* (- 6), - 1009.

163. ten Brummelhuis, N.; Schlaad, H., Stimuli-responsive star polymers through thiol-yne core functionalization/crosslinking of block copolymer micelles. *Polym. Chem.* **2011,** *2* (5), 1180-1184.